UNIVERSIDADE FEDERAL DE UBERLÂNDIA
FACULDADE DE ENGENHARIA QUÍMICA
PROGRAMA DE PÓS-GRADUAÇÃO EM ENGENHARIA QUÍMICA

Investigating the structure-activity relationship of materials applied in CO_2 capture and its conversion to CO

Investigação da relação estrutura-atividade de materiais aplicados na captura de CO_2 e em sua conversão a CO

Dyovani Bruno Lima dos Santos

Uberlândia - MG
March - 2022

UNIVERSIDADE FEDERAL DE UBERLÂNDIA

FACULDADE DE ENGENHARIA QUÍMICA

PROGRAMA DE PÓS-GRADUAÇÃO EM ENGENHARIA QUÍMICA

Investigating the structure-activity relationship of materials applied in CO_2 capture and its conversion to CO

Investigação da relação estrutura-atividade de materiais aplicados na captura de CO_2 e em sua conversão a CO

Dyovani Bruno Lima dos Santos

Orientadora: Profª. Drª. Carla Eponina Hori

Co-orientador: Dr. Fábio Bellot Noronha

Tese submetida ao Programa de Pós-Graduação em Engenharia Química da Universidade Federal de Uberlândia como parte dos requisitos necessários à obtenção do título de Doutor em Engenharia Química, área de concentracao em Pesquisa e Desenvolvimento de Processos Químicos.

Uberlândia - MG

March - 2022

Ficha Catalográfica Online do Sistema de Bibliotecas da UFU
com dados informados pelo(a) próprio(a) autor(a).

S237 Santos, Dyovani Bruno Lima dos, 1992-
2022 Investigating the structure-activity relationship of materials applied in CO2 capture and its conversion to CO [recurso eletrônico] / Dyovani Bruno Lima dos Santos. - 2022.

Orientadora: Carla Eponina Hori.
Coorientador: Fábio Bellot Noronha.
Tese (Doutorado) - Universidade Federal de Uberlândia, Pós-graduação em Engenharia Química.
Modo de acesso: Internet.
Disponível em: http://doi.org/10.14393/ufu.te.2022.196
Inclui bibliografia.

1. Engenharia química. I. Hori, Carla Eponina,1965-, (Orient.). II. Noronha, Fábio Bellot,1963-, (Coorient.). III. Universidade Federal de Uberlândia. Pós-graduação em Engenharia Química. IV. Título.

CDU: 66.0

Bibliotecários responsáveis pela estrutura de acordo com o AACR2:
Gizele Cristine Nunes do Couto - CRB6/2091
Nelson Marcos Ferreira - CRB6/3074

UNIVERSIDADE FEDERAL DE UBERLÂNDIA
Coordenação do Programa de Pós-Graduação em Engenharia Química
Av. João Naves de Ávila, 2121, Bloco 1K, Sala 206 - Bairro Santa Mônica, Uberlândia-MG, CEP 38400-902
Telefone: (34)3239-4249 - www.ppgeq.feq.ufu.br - secppgeq@feq.ufu.br

ATA DE DEFESA - PÓS-GRADUAÇÃO

Programa de Pós-Graduação em:	Engenharia Química				
Defesa de:	Tese de Doutorado, 05/2022, PPGEQ				
Data:	31 de março de 2022	Hora de início:	9:00	Hora de encerramento:	13:15
Matrícula do Discente:	11723EQU002				
Nome do Discente:	Dyovani Bruno Lima dos Santos				
Título do Trabalho:	Estudo da relação estrutura-atividade de materiais aplicados à captura de dióxido de carbono e sua conversão à monóxido de carbono				
Área de concentração:	Desenvolvimento de Processos Químicos				
Linha de pesquisa:	Termodinâmica, Cinética Química e Reatores				
Projeto de Pesquisa de vinculação:	Produção de hidrogênio a partir de reforma de hidrocarbonetos				

Reuniu-se por meio de webconferência, a Banca Examinadora, designada pelo Colegiado do Programa de Pós-graduação em Engenharia Química, assim composta: Professores Doutores: José Maria Corrêa Bueno - DEQ/UFSCar; Liane Márcia Rossi - IQ/USP; Lucienne Lobato Romanielo - PPGEQ/UFU; Érika Ohta Watanabe - PPGEQ/UFU; Fábio Bellot Noronha - INT/RJ, coorientador e Carla Eponina Hori - PPGEQ/UFU, orientadora do candidato.

Iniciando os trabalhos a presidente da mesa, Profa. Dra. Carla Eponina Hori, apresentou a Comissão Examinadora e o candidato, agradeceu a presença do público, e concedeu ao Discente a palavra para a exposição do seu trabalho. A duração da apresentação do Discente e o tempo de arguição e resposta foram conforme as normas do Programa.

A seguir o senhor(a) presidente concedeu a palavra, pela ordem sucessivamente, aos(às) examinadores(as), que passaram a arguir o(a) candidato(a). Ultimada a arguição, que se desenvolveu dentro dos termos regimentais, a Banca, em sessão secreta, atribuiu o resultado final, considerando o(a) candidato(a):

aprovado.

Esta defesa faz parte dos requisitos necessários à obtenção do título de Doutor.

O competente diploma será expedido após cumprimento dos demais requisitos, conforme as normas do Programa, a legislação pertinente e a regulamentação interna da UFU.

Nada mais havendo a tratar foram encerrados os trabalhos. Foi lavrada a presente ata que após lida e achada conforme foi assinada pela Banca Examinadora.

Documento assinado eletronicamente por **Carla Eponina Hori**, **Professor(a) do Magistério Superior**, em 31/03/2022, às 13:17, conforme horário oficial de Brasília, com fundamento no art. 6º, § 1º, do Decreto nº 8.539, de 8 de outubro de 2015.

Documento assinado eletronicamente por **Erika Ohta Watanabe**, **Professor(a) do Magistério Superior**, em 31/03/2022, às 13:17, conforme horário oficial de Brasília, com fundamento no art. 6º,

§ 1º, do Decreto nº 8.539, de 8 de outubro de 2015.

Documento assinado eletronicamente por **Liane Marcia Rossi**, **Usuário Externo**, em 31/03/2022, às 13:17, conforme horário oficial de Brasília, com fundamento no art. 6º, § 1º, do Decreto nº 8.539, de 8 de outubro de 2015.

Documento assinado eletronicamente por **Lucienne Lobato Romanielo**, **Professor(a) do Magistério Superior**, em 31/03/2022, às 13:18, conforme horário oficial de Brasília, com fundamento no art. 6º, § 1º, do Decreto nº 8.539, de 8 de outubro de 2015.

Documento assinado eletronicamente por **JOSÉ MARIA CORREA BUENO**, **Usuário Externo**, em 14/04/2022, às 11:41, conforme horário oficial de Brasília, com fundamento no art. 6º, § 1º, do Decreto nº 8.539, de 8 de outubro de 2015.

Documento assinado eletronicamente por **Fabio Bellot Noronha**, **Usuário Externo**, em 17/05/2022, às 15:25, conforme horário oficial de Brasília, com fundamento no art. 6º, § 1º, do Decreto nº 8.539, de 8 de outubro de 2015.

A autenticidade deste documento pode ser conferida no site https://www.sei.ufu.br/sei/controlador_externo.php?acao=documento_conferir&id_orgao_acesso_externo=0, informando o código verificador **3466215** e o código CRC **42729FA6**.

Referência: Processo nº 23117.018039/2022-95 SEI nº 3466215

AGRADECIMENTOS

Primeiramente, eu gostaria de agradecer a Deus por toda proteção e bençãos derramadas sobre mim durante esses anos.

Agradeço a toda minha família, meus avós Abadia e Altaídes, meus tios Edson, Jesus e Celso, minha tia Maria Abadia e meu padrinho Eurípedes. Em especial, agradeço minha amada mãe Márcia que sempre me deu muito amor e carinho em toda minha vida. Obrigado por toda paciência e suporte que todos vocês me deram durante essa jornada.

Meu muito obrigado também ao meu namorado, Aristides o qual sempre esteve ao meu lado me dando todo amor, apoio e suporte necessário nos momentos bons e também nos difíceis. Obrigado pela paciência e por me ouvir nos momentos de desabafo.

Gostaria de agradecer aos colegas do laboratório, Carolina Marinho, Lucas Mendes, Thales, Rafael, Ana Caroline, Sarah, Caroline Lemos, Rondi e Ana Soldan que durante esse tempo pude ter o privilégio de conviver e aprender muito. Em especial, meu muito obrigado as minhas amigas Karen Resende e Leticia Rade. Obrigado por todo o suporte, conversas, boas risadas, conselhos e todo o carinho nesses anos. Gostaria de agradecer também ao grande amigo e colega de laboratório Lucas Moura que esteve presente durante meu mestrado e doutorado. Nesse tempo, você foi fundamental e um dos pilares para a construção desse trabalho. Meu muito obrigado pelas conversas, lanches e almoços, viagens a congresso, e por ser um exemplo que levarei para vida.

Ao todo o corpo técnico da Faculdade de Engenharia Química — UFU por todo o suporte dado para a construção desse trabalho. Meu obrigado também aos técnicos do LNLS e do ESRF que ajudaram na realização dos experimentos no síncrotron.

Agradeço imensamente a minha orientadora Profa. Dra. Carla Hori. Obrigado por todo o conhecimento técnico e pessoal transmitido ao longo desses anos, por todas as horas de dedicação a mim, por todo suporte, conselhos, carinho, pela paciência e pelos puxões de orelha. Obrigado por todo esforço em minha formação e para que minha viagem ao exterior acontecesse. Cresci muito profissional e pessoalmente. Agradeço também ao Dr. Fábio Noronha por toda contribuição e suporte cientifico na construção desse trabalho. Meu muito obrigado a vocês.

Aos amigos e colegas do laboratório LESE – ETH Zurich, obrigado por todo suporte, paciência, ajuda e carinho durante minha estadia. Em especial, aos amigos que fiz durante esse 1 ano, Nora Zimmerli, Evgenia Kountoupi, Angelo Bellia e David Niedbalka, obrigado por todos os bons momentos de conversa e confraternização. Vocês me proporcionaram uma

experiência magnifica que levarei para o resto da vida. Também tenho muito a agradecer ao Prof. Dr. Christoph Muller e a Drª. Paula Abdala pela oportunidade de estagiar no grupo e por todo conhecimento cientifico e pessoal compartilhado. Meu muito obrigado!

Agradeço à CAPES, FAPEMIG, CNPq, LNLS e FEQUI-UFU pelo apoio financeiro concedido.

E por último, agradeço a todos que contribuíram direta e indiretamente para a realização desse trabalho.

ABSTRACT

Carbon capture, utilization, and storage (CCUS) have been shown as a promising strategy to decrease anthropogenic CO_2 emissions and, consequently, mitigate climate change. It refers to a suite of technologies that are associated with capturing CO_2 from industrial processes or directly from the air and using the CO_2 captured as a feedstock to produce valuable chemicals and fuels. Nevertheless, the development of materials applied in these technologies is crucial to make them suitable and to increase the number of CCUS facilities operating worldwide. This doctoral dissertation focuses on the development of sorbent for the CO_2 capture during the steam reforming of methane which is an established route to produce hydrogen and the use of CO_2 in the reverse water gas shift reaction (rWGS) applying the intermetallic/alloy compounds as catalysts.

Regarding CO_2 capture, calcium oxide as a sorbent has become an alternative to amine scrubbing due to advantages such as reduced CO_2 capture costs and high theoretical CO_2 capture capacities (0.78 g CO_2/gCaO). However, the sintering of CaO particles on cyclic operation is the major problem, limiting its practical implementation. In this scenario, the addition of alkali molten salts has been reported as a strategy to overcome the deactivation of calcium oxide in CO_2 capture systems. In the first study, we investigated the influence of sodium doping on the CaO sorbent in the sorption-enhanced steam methane reforming process (SE-SMR). The goal was to increase the stability of the sorbent and, consequently, the efficiency of the process. For that, a Na-containing CaO sorbent was prepared using the precipitation technique and a pure calcium oxide was obtained by calcination of $CaCO_3$. The sorbents were physically mixed with 10% Ni/Al_2O_3 catalyst and tested in 10 cycles of SE-SMR at 600 °C and CH_4:H_2O equal to 1:4. In general, both materials showed 100% of CH_4 conversion and H_2 molar fraction of 93.5 vol.%. However, regarding the stability during the SE-SMR cycles, it was evidenced that the addition of sodium decreased the duration of pre-breakthrough compared with the non-doped material. The XRD, SEM, and TGA results allowed us to observe an inverse relationship between particle diameter and CO_2 capture performance. Na_2CO_3-CaO presented a higher average crystallite size compared to the pure CaO, which led to a higher probability of the $CaCO_3$ layers to inactivate the calcium oxide and, consequently, cause a strong sintering effect. Besides the presence of sodium, the precipitation method and the synthesis conditions could have favored the low initial CO_2 uptake and poor stability of the Na_2CO_3-CaO sorbent.

Turning to the use of CO_2 as a feedstock, the conversion of CO_2 to CO via reverse water gas shift reaction represents an important route, since the CO produced can be an intermediate to produce fuels and valuable chemicals (e.g. methanol synthesis). However, the undesired reactions, such as the methanation reaction, compete with the rWGS reaction, decreasing the CO formation. Thereby, the development of a catalyst that enhances the CO selectivity and minimizes CH_4 formation is essential and, for this, the use of bimetallic catalyst is a viable strategy. The addition of a second metal can result in a compound that has a peculiar electronic and crystal structure, leading to chemical potentials that can optimize the catalytic performance. In the second study, we investigate the structure-activity relationship of the bimetallic Ni-In catalyst in the rWGS reaction at 450 °C, 1 bar, and under different feed compositions. Ni/SiO_2, $Ni_{0.85}In_{0.15}/SiO_2$, and $Ni_{0.50}In_{0.50}/SiO_2$ were synthesized by the hydrothermal method that resulted in similar particle size (~5 nm) for all catalysts and homogenous dispersion of both metals on the support. The addition of indium promoted CO selectivity (greater than 99%) even at a higher H_2:CO_2 molar ratio. *In situ* XRD-XAS and CO-DRIFTS results revealed that the presence of indium resulted in a catalyst with a different coordination environment and chemical bond when compared to Ni/SiO_2. Moreover, the indium act as a spacer that prevents the formation of Ni-Ni ensembles leading to a weaker CO adsorption on $Ni\text{-}In/SiO_2$ than on Ni/SiO_2 catalyst, which may justify the high CO selectivity demonstrated by the bimetallic catalysts.

Keywords: CCUS; calcium oxide; steam reforming of methane; rWGS reaction; intermetallic compounds; nickel; indium.

RESUMO

A captura, utilização e armazenamento de carbono (CCUS) tem se mostrado como uma estratégia promissora para diminuir as emissões antropogênicas de CO_2 e, consequentemente, mitigar as mudanças climáticas. Essa refere-se a um conjunto de tecnologias as quais estão associadas à captura de CO_2 dos processos industriais ou diretamente do ar e ao uso do CO_2 capturado como matéria-prima para produzir produtos químicos e combustíveis de maior valor agregado. Entretanto, o desenvolvimento de materiais aplicados nestas tecnologias é crucial para torná-las adequadas e para aumentar o número de instalações CCUS operando em todo o mundo. Esta tese de doutorado tem como foco o desenvolvimento de sorventes para a captura de CO_2 durante a reforma a vapor do metano que é uma rota estabelecida para produzir hidrogênio e o uso do CO_2 na reação inversa de deslocamento gás-água (rWGS) aplicando os compostos intermetálicos/ligados como catalisadores.

Em relação à captura de CO_2, o óxido de cálcio como sorvente se tornou uma alternativa ao tratamento de gás com amina devido a vantagens como custos reduzidos de captura de CO_2 e alta capacidade teórica de captura de CO_2 (0,78 g CO_2/gCaO). Entretanto, a sinterização das partículas de CaO durante a operação cíclica é o maior problema limitando sua implementação prática. Neste cenário, a adição de sais alcalinos tem sido relatada como uma estratégia para superar a desativação do óxido de cálcio em sistemas de captura de CO_2. No primeiro estudo, investigamos a influência do dopagem de sódio no sorvente de CaO no processo de reforma do metano a vapor melhorada (SE-SMR). O objetivo foi aumentar a estabilidade do sorvente e, consequentemente, a eficiência do processo. Para isso, preparou-se um sorvente contendo sodium usando a técnica de precipitação e o óxido de cálcio puro foi obtido por calcinação de $CaCO_3$. Os sorventes foram fisicamente misturados com 10% do catalisador Ni/Al_2O_3 e testados em 10 ciclos da SE-SMR a 600 °C e CH_4:H_2O igual a 4. Em geral, ambos os materiais mostraram 100% de conversão do CH_4 e fração molar de H_2 igual a 93,5 vol.%. Entretanto, com relação à estabilidade durante os ciclos SE-SMR, ficou evidenciado que a adição de sódio diminuiu a duração da pré-breakthrough em comparação com o material não dopado. Os resultados do XRD, SEM e TGA nos permitiram observar uma relação inversa de diâmetro de partícula e desempenho de captura de CO_2. O sorvente Na_2CO_3-CaO apresentou um tamanho médio de cristalito mais alto em comparação com o CaO puro, o que levou a uma maior probabilidade das camadas de $CaCO_3$ inativarem o óxido de cálcio e, consequentemente, causarem um forte efeito de sinterização. Além da presença de sódio, o método de precipitação

e as condições de síntese podem ter causado a baixa absorção inicial de CO_2 e a baixa estabilidade do adsorvente de Na_2CO_3-CaO.

Voltando ao uso do CO_2 como matéria-prima, a conversão de CO_2 em CO através da reação inversa de deslocamento gás-água representa uma rota importante, visto que o CO produzido pode ser um intermediário para produzir combustíveis e produtos químicos valiosos (por exemplo, síntese de metanol). Entretanto, as reações indesejadas como a reação de metanação competem com a reação de rWGS, diminuindo a formação de CO. Portanto, o desenvolvimento de catalisadores que aumentem a seletividade do CO e minimizem a formação de CH_4 é essencial e, para isso, o uso de catalisador bimetálico é uma estratégia viável. A adição de um segundo metal pode resultar em um composto com uma peculiar estrutura eletrônica e cristalina, levando a potenciais químicos que podem otimizar o desempenho catalítico. No segundo estudo, investigamos a relação estrutura-actividade do catalisador bimetálico Ni-In na reação de rWGS a 450 °C, 1 bar, e sob diferentes composições de alimentação. Ni/SiO_2, $Ni_{0,85}In_{0,15}/SiO_2$ e $Ni_{0,50}In_{0,50}/SiO_2$ foram sintetizados pelo método hidrotérmico que resultou em um tamanho de partícula similar (~5 nm) para todos os catalisadores e uma dispersão homogênea de ambos os metais no suporte. A adição de índio promoveu a seletividade de CO (maior que 99%) mesmo com uma relação molar H_2:CO_2 mais alta. Os resultados *in situ* XRD-XAS e CO-DRIFTS revelaram que a presença de índio resultou em um catalisador com um ambiente de coordenação e ligação química diferente quando comparado com Ni/SiO_2. Além disso, o índio atua como espaçador o que impede a formação de conjuntos de Ni-Ni levando a uma adsorção mais fraca de CO no $Ni\text{-}In/SiO_2$ do que no catalisador Ni/SiO_2 que pode justificar a alta seletividade de CO mostrada pelos catalisadores bimetálicos.

Palavras-chave: CCUS; óxido de cálcio; reforma a vapor do metano; reação deslocamento gás-água; compostos intermetálicos; níquel; indío.

LIST OF FIGURES

LIST OF TABLES

ACRONYMS

AR5 – Fifth Annual Assessment Report

BET – Brunauer-Emmett-Teller (surface area)

CCUS – Carbon Capture, Utilization, and Storage technology

DFR – Dual Fixed-bed Reactor

DFT – Density Functional Theory

DRIFTS – Diffuse Reflectance Infrared Fourier Transform Spectroscopy

EDS – Energy Dispersive Spectroscopy

EXAFS – Extended X-ray Absorption Fine Structure

FB – Fluidized Bed reactor

FIB-TEM – Focused Ion Beam - Transmission Electron Microscopy

FSP – Flame Spray Pyrolysis

FTIR – Fourier-Transform Infrared Spectroscopy

GHG – Greenhouse gases

GHSV – Gas Hour Space Velocity

HTlc – Hydrotalcite

ICP-OES – Inductively Coupled Plasma Optical Emission Spectrometry

ICSD – Inorganic Crystal Structure Database

IEA – International Energy Agency

IPCC – Intergovernmental Panel on Climate Change

LHV – Lower Heating Value

LNG – Liquified Natural Gas

LNLS – Laboratório Nacional de Luz Síncronton

MCT - Mercury-Cadmium-Telluride detector

MEA – Monoethanolamine

MOF – Metal-organic frameworks

MS - Mass Spectrometry

NIST – National Institute of Standards and Technology

PS - Phyllosilicate

PSA – Pressure Swing Adsorption

rWGS – Reverse Water Gas Shift

SDS – Sustainable Development Scenario

SEM – Scanning Spectroscopy Microscopy

SE-SRM – Sorption Enhanced Steam Reforming of Methane

SE-SRP – Sorption Enhanced Steam Reforming Process

SNBL – Swiss-Norwegian Beamlines

SRM – Steam Reforming of Methane

SSITKA – Steady-State Isotopic Transient Kinetic Analysis

STEM – Scanning Transmission Electron Microscopy

TCD – Thermo Conductivity Detector

TEM – Transmission Electron Microscopy

TGA – Thermogravimetric analyzer

TPD – Temperature-programmed desorption

TPR – Temperature-programmed reduction

USP – Ultrasonic Spray Pyrolysis

WGS – Water Gas Shift

XANES – X-ray Absorption Near Edge Structure

XPS – X-ray Photoelectron Spectroscopy

XRD – X-ray Diffraction

SUMMARY

Chapter 1 - INTRODUCTION

The worldwide energy demand has been increasing, driven by the growth of the global economy.[1] The increase in the anthropogenic greenhouse gases (GHG) can be associated with these new scenarios presented in the energy sector. One of the negative consequences of the accelerated growth and the high energy demand is the increase in the CO_2 emissions from fossil fuels combustion, resulting in several climate changes with serious environmental damage such as sea-level rise, heavy precipitation, and impacts on biodiversity and ecosystems.[2] These effects could be irreversible if global warming caused by GHG emissions continues to increase. According to the Intergovernmental Panel on Climate Change (IPCC), the global net anthropogenic CO_2 emissions must be zero around 2050 to limit global temperature increase to 1.5 °C.[2, 3]

To achieve the targets proposed to regulate climate neutrality, the Carbon Capture, Utilization, and Storage (CCUS) technologies have been a promising pathway including technical, economic, and public approval considerations to reduce de CO_2 emissions.[4] This type of technology involves (i) the capture of CO_2 produced by large industrial plants (such as power plants), (ii) the storage of the CO_2 into a rock formation by its deep reinjection, and/or (iii) the use of CO_2 as a raw material for the production of fuels, chemicals, building materials, among others.[4]

Significant efforts have been made to increase the role and contribution of CCUS as a tool to provide a reduction of CO_2 emissions to the atmosphere. Its technical and economic viability involves the development of new materials that can effectively capture the CO_2 as well as catalysts that are suitable to activate CO_2 molecules and, at the same time, provide high selectivity towards the desired products.

CO_2 capture could be performed by various materials such as CaO, MgO, hydrotalcite, zeolites depending on the temperature operation in the CCUS process.[5] Particularly, calcium oxide is the most used material for CO_2 capture due to features such as high CO_2 adsorption capacity, high-temperature operation, low cost, excellent CO_2 adsorption/desorption rate, and wide availability in nature as dolomite.[5, 6] However, particle sintering is the main problem presented by the Ca-based sorbents causing the decay of CaO activity over the carbonation and regeneration process.[7]

One promising application of Ca-based sorbent for CO_2 capture is on the hydrogen production using steam reforming of hydrocarbons. This new field of research is called sorption

enhanced steam reforming process (SE-SRP). Based on Le Chatelier's principle, the concept of SE-SRP is to shift the equilibrium reaction beyond the conventional thermodynamic limit to obtain high-purity hydrogen production combined with simultaneous CO_2 capture.[8-10] This process presents substantial benefits, for example, higher reactant conversion and yields of H_2 (> 95 vol.%), improved process efficiency, lower reaction temperature than the conventional reforming reactions, and lower investment cost.[6, 9, 10] This new technology could be applied for steam reforming of methane (SRM) that is the current main route to produce hydrogen from fossil fuels (natural gas) and, consequently, an interesting way to decrease CO_2 emissions and potentialize hydrogen as a clean fuel.

Numerous alternative approaches have been developed to overcome the sintering problems presented by calcium oxide, including insertion of inert into calcium oxide structure, the addition of treatments (e.g. hydration), development of new synthesis method, doping with alkaline metals, among others. Also, some advanced researches have been made regarding the optimization of SE-SRP to become a mature technology and to investigate the scale and commercial viability.[4]

Another important aspect is that the CO_2 captured in the SE-SRP can be stored in the rock formations or used as input or feedstock in various processes. Specifically, the catalytic reduction of CO_2 into value-added products such as methanol, formic acid, olefins, and dimethyl ether (DME) is an example of possible use.[11] In general, the reduction of CO_2, also called the reverse water gas shift reaction, produces CO that can act as an intermediate to produce alcohols like methanol.[12] The higher reactivity of the CO molecules makes them much more energetically favorable and easier to convert into other products.[13, 14] For that, the thermochemical conversion of CO_2 to CO is commonly performed by catalysts based on precious metals (Pt, Pd, Au, and Ru) or the free-precious metals (Cu, Ni, Co, and Fe) in which the latter has shown good CO_2 conversions and CO selectivity.[11, 14]

Despite the fair activity and low-cost material, some drawbacks appear in non-precious metals catalysts, such as the sintering in the Cu-based catalysts and high methanation rates in the Ni-based catalysts.[15] In both cases, the consequence is the decrease in activity and in CO formation rates in the rWGS reaction. One alternative to overcome these drawbacks is to alloy two metals to form disordered or ordered alloy, which is known as an intermetallic compound.[16] This new material may have unique features due to changes in the surface atomic arrangement and modification of the electronic structure. Thereby, the addition of a second metal can modify and/or create new active sites that alter the activation, strength, and configuration of the

reactants and intermediates adsorption providing special properties for these intermetallic compounds.[17]

Therefore, the determination of the crystal structure and the electron promotion of such materials are fundamental to clarify the structure-activity relationship of the bimetallic catalysts in the rWGS reaction. Furthermore, understanding the mechanism of CO formation is crucial for the optimal design of catalyst aiming for high activity with enhanced CO selectivity as well as low CH_4 formation.

Overall, two important and current fields of the CCUS research were investigated in this thesis. Firstly, hydrogen production with simultaneous CO_2 capture since hydrogen is considered a potential fuel to decarbonize industrial processes, transport, domestic heating, and economies. Secondly, the use of CO_2 as a raw material to produce value-added products that can be a vital way to reduce CO_2 emissions and, at the same time, provide an efficient way to manufacture a wide range of chemical products.

1.1 Outline of this thesis

This doctoral thesis contains 6 chapters.

Chapter 2 presents a review of the capture and utilization of CO_2. Specifically, the review comprises the application of CaO as a sorbent for CO_2 capture in sorption enhanced steam reforming process for hydrogen production and the use of CO_2 as feedstock in the reverse water gas shift reaction and the application of intermetallic compounds as catalysts.

Chapter 3 present the main and specifics objectives of this work.

Chapter 4 focuses on investigating the influence of the alkali metal as a promoter in CaO sorbent using the precipitation method. The Ni/Al_2O_3 catalyst and Na_2CO_3/CaO sorbent were physically mixed and applied in sorption enhanced steam reforming of methane. The behavior observed was explained by the structural characterization results such as N_2 physisorption, thermogravimetric analyses, *in situ* XRD, *in situ* XANES, and scattering spectroscopy microscopy (SEM) coupled with EDS. This chapter was published in the scientific journal: Santos, D. B. L.; Oliveira, A. C. P.; Hori, C. E., Performance of Na_2CO_3-CaO sorbent in

sorption-enhanced steam methane reforming. *Journal of CO_2 Utilization* **2021**, 51, 101634. https://doi.org/10.1016/j.jcou.2021.101634.

Chapter 5 involves the study of bimetallic Ni-In catalysts for the rWGS reaction at 450 °C and 1 bar. The materials were characterized by ICP, TEM, *in situ* XRD-XAS, and CO-DRIFTS in order to understand the influence of the indium addition in the CO selectivity as well as the structure-activity relationship of the intermetallic Ni-In catalyst.

Chapter 6 summarizes the main conclusions obtained by the thesis and recommendations of approaches for future work.

1.2 References

1. IEA *Global energy & CO_2 status*; 2019.
2. IPCC *Climate Change 2014: Synthesis Report. Contribution of Working Groups I, II and III to the Fifth Assessment Report of the Intergovernmental Panel on Climate Change*; Geneva, Switzerland, 2014; p 151.
3. IEA *Energy Technology Perspectives* 2016.
4. Instituite, G. C. *GCC-Global status of CCS*; 2019.
5. Choi, S.; Drese, J. H.; Jones, C. W., Adsorbent materials for carbon dioxide capture from large anthropogenic point sources. *ChemSusChem* **2009,** *2* (9), 796-854. https://doi.org/10.1002/cssc.200900036
6. Shokrollahi Yancheshmeh, M.; Radfarnia, H. R.; Iliuta, M. C., High temperature CO_2 sorbents and their application for hydrogen production by sorption enhanced steam reforming process. *Chemical Engineering Journal* **2016,** *283*, 420-444. https://doi.org/10.1016/j.cej.2015.06.060
7. Broda, M. Synthetic calcium-based sorbents for pre-and post-combustion CO_2 capture. ETH Zürich, 2019.
8. Barelli, L.; Bidini, G.; Gallorini, F.; Servili, S., Hydrogen production through sorption-enhanced steam methane reforming and membrane technology: a review. *Energy* **2008,** *33* (4), 554-570. https://doi.org/10.1016/j.energy.2007.10.018
9. Carvill, B. T.; Hufton, J. R.; Anand, M.; Sircar, S., Sorption-enhanced reaction process. *AIChE Journal* **1996,** *42* (10), 2765-2772. https://doi.org/10.1002/aic.690421008
10. Harrison, D. P., Sorption-enhanced hydrogen production: a review. *Industrial & Engineering Chemistry Research* **2008,** *47* (17), 6486-6501. https://doi.org/10.1021/ie800298z
11. González-Castaño, M.; Dorneanu, B.; Arellano-García, H., The reverse water gas shift reaction: a process systems engineering perspective. *Reaction Chemistry & Engineering* **2021,** *6* (6), 954-976. https://doi.org/10.1039/d0re00478b
12. Porosoff, M. D.; Yan, B.; Chen, J. G., Catalytic reduction of CO_2 by H_2 for synthesis of CO, methanol and hydrocarbons: challenges and opportunities. *Energy & Environmental Science* **2016,** *9* (1), 62-73. https://doi.org/10.1039/c5ee02657a
13. Su, X.; Yang, X.; Zhao, B.; Huang, Y., Designing of highly selective and high-temperature endurable RWGS heterogeneous catalysts: recent advances and the future directions. *Journal of Energy Chemistry* **2017,** *26* (5), 854-867. https://doi.org/10.1016/j.jechem.2017.07.006
14. Daza, Y. A.; Kuhn, J. N., CO_2 conversion by reverse water gas shift catalysis: comparison of catalysts, mechanisms and their consequences for CO_2 conversion to liquid fuels. *RSC Advances* **2016,** *6* (55), 49675-49691. https://doi.org/10.1039/c6ra05414e

15. Chen, P.; Zhao, G.; Shi, X. R.; Zhu, J.; Ding, J.; Lu, Y., Nano-intermetallic $InNi_3C_{0.5}$ compound discovered as a superior catalyst for CO_2 reutilization. *iScience* **2019,** *17*, 315-324. https://doi.org/10.1016/j.isci.2019.07.006
16. Armbruster, M., Intermetallic compounds in catalysis - a versatile class of materials meets interesting challenges. *Sci Technol Adv Mater* **2020,** *21* (1), 303-322. https://doi.org/10.1080/14686996.2020.1758544
17. Furukawa, S.; Komatsu, T.; Shimizu, K.-i., Catalyst design concept based on a variety of alloy materials: a personal account and relevant studies. *Journal of Materials Chemistry A* **2020,** *8* (31), 15620-15645. https://doi.org/10.1039/d0ta03733h

Chapter 2 - LITERATURE REVIEW

2.1 Background

Nowadays, fossil fuels dominate primary energy source in the world representing 79.1% of the total energy consumption (Figure 2.1).[1] In addition, in 2018 the global energy consumption increased at nearly twice the average rate growth since 2010, driven by a robust global economy and higher heating and cooling needs in some parts of the world.[2] The mainly responsible countries for the increase in energy demand are China, United States, and India, which together account for almost 70% of the total. However, the pandemic of COVID-19 impacted the global energy demand due to the necessary restrictions on movement. The global energy demand in 2020 fell by 4% which was the largest decline since World War II and the largest ever absolute decline. In a different trend, the demand in 2021 was set to increase by 4.6% followed by stimulus packages and vaccine rollouts.[3]

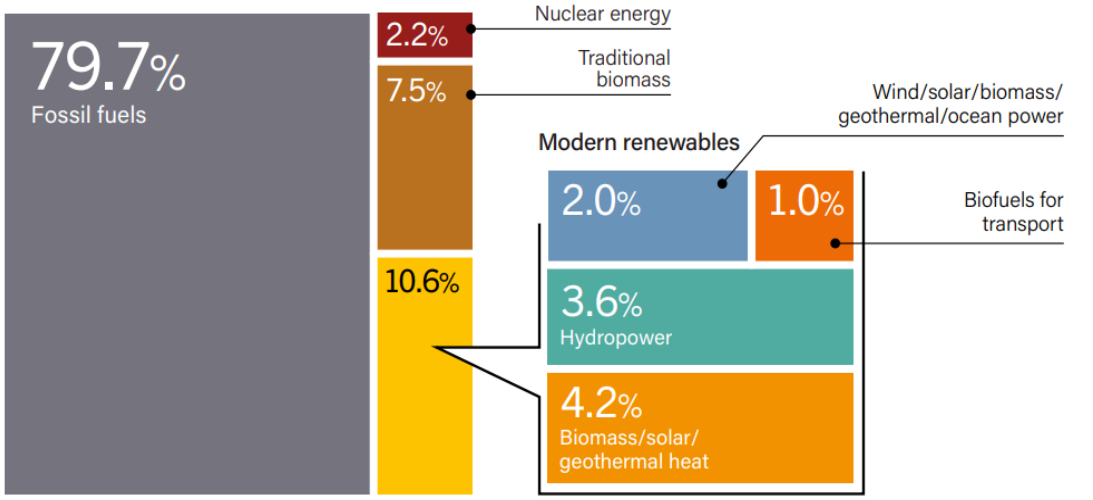

Figure 2.1: Estimated renewable share of total final energy consumption in 2017.[1] (Source: Based on OECD/IEA and IEA SHC.)

As a result of higher energy consumption, global energy related-CO_2 emissions rose to a historic high of 33.5 Gt CO_2 in 2018 (Figure 2.2).[2] Despite the decline of 5.8% of the global CO_2 emissions 2020, the emissions remained at 31.5 Gt which represents the highest ever average annual concentration in the atmosphere of 412.5 ppm.[3] In 2021, the increase demand for coal, oil, and gas associated with the intensive economic recovery and rebound of the activity economy caused an increase of 4.8% in the global-related CO_2 emissions[3]. Moreover,

the CO_2 emissions from fossil fuel combustion and industrial processes are responsible for 78% of the total greenhouse gas (GHG) emission increase between 1970 and 2010[4].

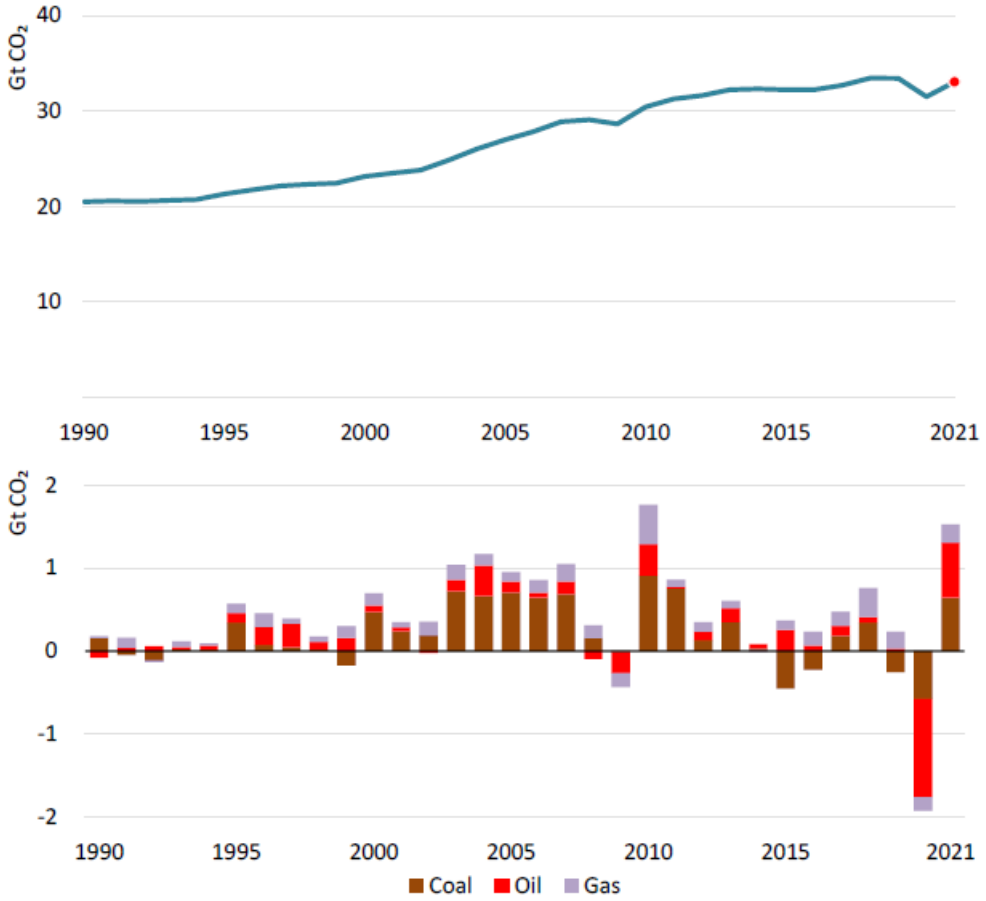

Figure 2.2: Global energy-related carbon dioxide emissions by source, 1990-2021.[3] (Source: IEA (2021), Global Energy Review, All rights reserved.)

The International Energy Agency (IEA) evaluated the impact of fossil fuel use on global temperature increases. Reported results indicated that the CO_2 emitted from coal combustion was responsible for over 0.3 °C of the 1 °C increase in global average annual surface temperature above pre-industrial levels. Associated with that, many efforts and enhancements have been done to increase energy efficiency and become feasibility the use of low-carbon technologies. Furthermore, after the Paris Agreement, the nations have been searching for development and rapid adoption of advanced technologies to reduce GHG emissions. The net emissions in the world will need to be equal to zero in 2050 so that the global temperature does not rise 1.5 °C above pre-industrial levels.[5] The carbon capture, utilization, and storage (CCUS) has been an interesting and promising tool to reduce GHG emissions and help in the decarbonization of industry. It refers to a suite of technologies that involves the capture of CO_2 from industrial facilities, power generation, or directly from the air. The captured CO_2 could be

used on-site as a feedstock for the production of synthetic fuels, chemicals, and building materials or could be compressed and transported by pipeline to be injected into deep geological rock formations.[6] Figure 2.3 schematically shows the processes involved in the CUS.

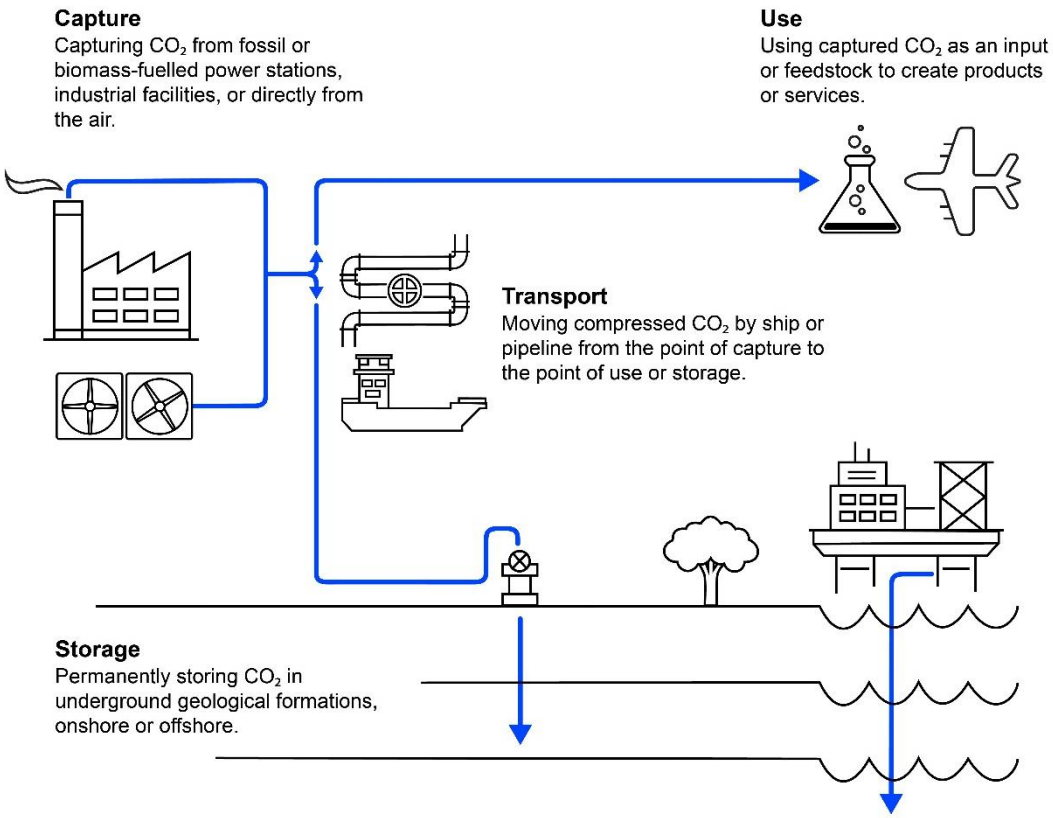

Figure 2.3: Schematic representation of carbon capture, utilization, and storage.[6] (Source: IEA (2020), Energy Technology Perspectives, All rights reserved.)

The Intergovernmental Panel on Climate Change (IPCC) and International Energy Agency (IEA) have been shown by many analyses that CCUS is an essential part of the lowest cost path towards meeting climate targets. To illustrate this, the IPCC's Fifth Annual Assessment Report (AR5) showed that excluding CCUS from the portfolio technologies used to reduce emissions would lead to doubling the cost which makes this the largest cost increase from the exclusion of any technology[7].

In the current scenario, the global development and deployment of the CCUS continued to gather pace as shown in Figure 2.4. The number of large-scale CCUS facilities increased to 51 in 2019, from which nineteen are in operation, four are under construction, ten are in advanced development, and eighteen are in early development.[7] Nevertheless, the establishment

of CCUS is not happening fast enough to reach the targets in global temperature projected by the Sustainable Development Scenario (SDS).

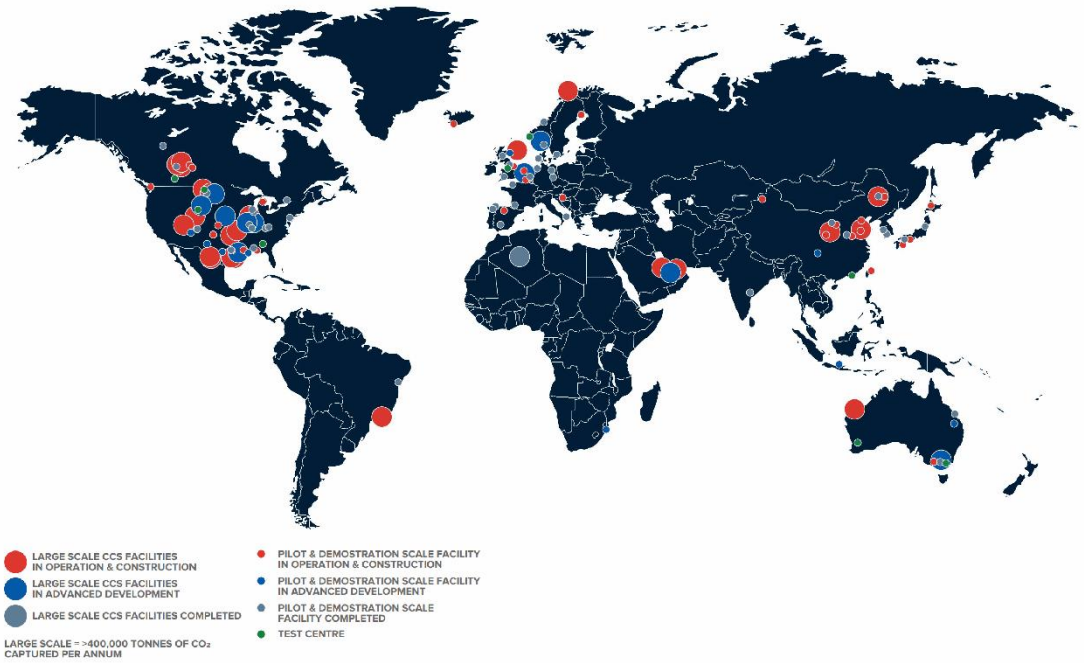

Figure 2.4: Current CCS facilities around the world.[7] (Source: Data from the Global CCS Institute CO_2RE database as of November 2019 (Global CCS Institute 2019a).

2.1.1 CO_2 capture technologies

CO_2 capture technologies are classified into three mains: (i) post-combustion, pre-combustion, and (iii) oxy-combustion CO_2 capture (Figure 2.5). In post-combustion capture, the CO_2 can be separated from gas flue stream which was produced by fuel combustion. In the pre-combustion CO_2 capture process, the carbon is removed from the fuel before its combustion and in oxy-combustion, the fuel is burned in a mixture of oxygen (and re-cycled CO_2) instead air to avoid the dilution of the CO_2 in N_2.

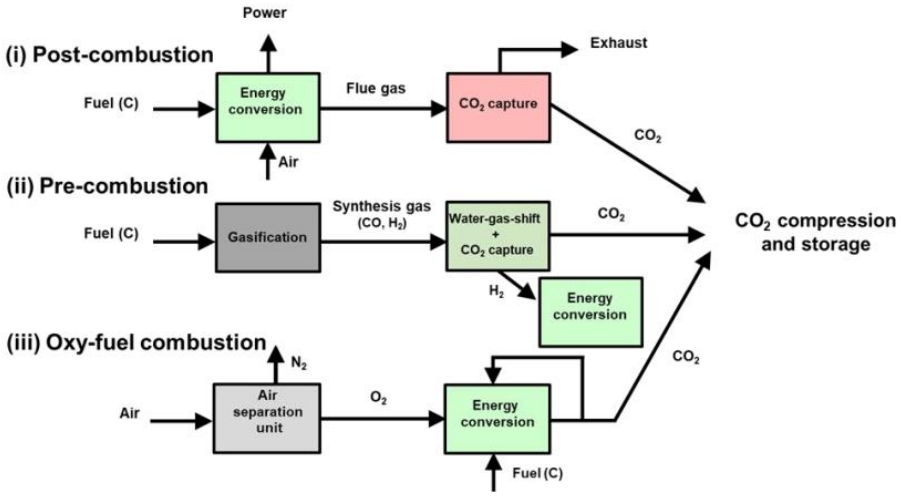

Figure 2.5: Schematic illustration of post-, pre-, and oxy-combustion schemes[8].

Many approaches have been established and developed to remove CO_2 from gas mixtures. In general, the separation of CO_2 from other light gases has been performed by four main approaches: cryogenic distillation, membrane purification, adsorption with liquids, and adsorption using solids.[9] Regarding cryogenic distillation, the process has a high energy cost making not a practical means. The use of membrane can be highly efficient when the species, which can pass through a selective membrane, is present in large concentrations.[10] Alternatively, the CO_2 adsorption technology involving liquid media as the absorbing phase is widely established. The absorption could be physical, e.g. methanol or poly (ethylene glycol) dimethyl ether, or chemical, e. g. amine solution or other fluids with a basic character that can absorb the acid gases.[11] The most used technology for CO_2 removal from gas mixture is amine scrubbing using monoethanolamine (MEA). Albeit, this process has several disadvantages such as a high estimated cost (\$60-107/t CO_2), the formation of toxic byproducts (e.g. nitroamines) and degradation of MEA due to thermal process and reaction with impurities.[12, 13] The use of solids in the adsorption process is also well-known and commonly used in cyclic operations of adsorption and desorption and/or desorption induced by a pressure or temperature swing.[14]

Several adsorbent materials have been used to capture CO_2 in a wide range of temperatures such as zeolites, activated carbons, metal-based sorbents (e.g. calcium oxides and magnesium oxides), hydrotalcite-like compounds organic and organic-inorganic hybrid adsorbents, and metal-organic frameworks (MOF) as shown in Figure 2.6. A lot of parameters are important to consider the material as a good CO_2 sorbent. They are adsorption/desorption kinetics, CO_2 capacity, good attrition resistance and mechanical strength, competitive cost, operation window, including adsorption and desorption temperature, ease of regeneration and

multicycle stability, and impact of common flue gas components or contaminants such as H_2O, Hg, SO_2, and NO_x.[14-17]

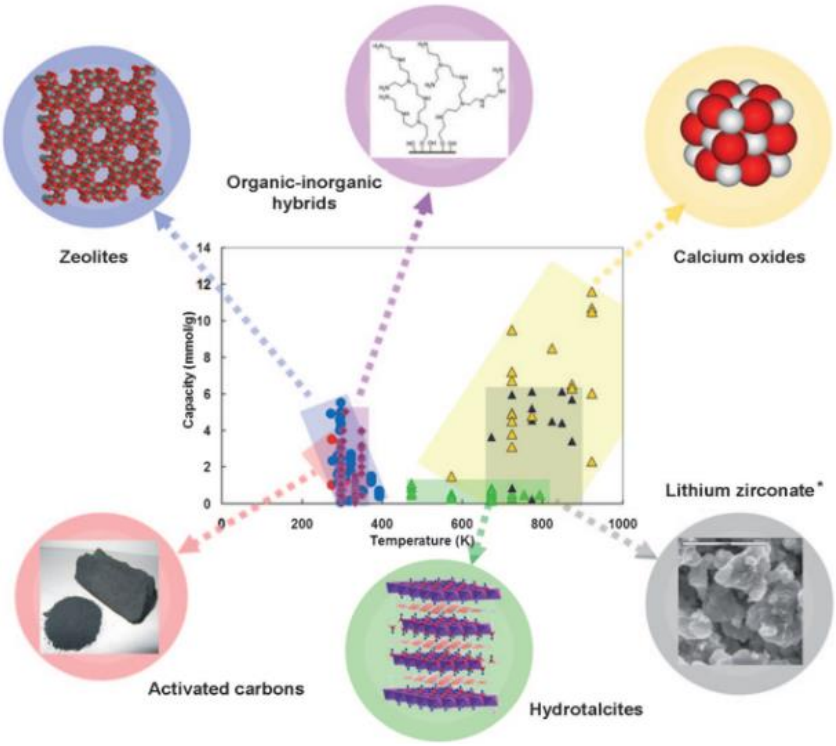

Figure 2.6: Comparison of the CO_2 sorption capacity of different types of sorbents. (Reproduced with permission from ref.[14] Copyright 2009 Wiley.)

2.2 Calcium oxide for CO_2 capture

Calcium oxide is one of the most attractive solids for CO_2 capture due to excellent properties. This sorbent presents low raw material cost (e.g. limestone and dolomite), low CO_2 capture cost ($12-32/t CO_2), high theoretical CO_2 sorption capacity (0.786 g CO_2/g sorbent), low toxicity, effectiveness at elevated temperatures and adequate kinetics of carbonation/regeneration reaction. The reversible reaction of CO_2 capture from calcium oxide sorbent is given by the Equation 2.1.

$$CaO + CO_2 \rightleftharpoons CaCO_3 \qquad \Delta H^0_{298K} = 178 \text{ kJ/mol} \qquad \text{Eq. 2.1}$$

The performance in CO_2 capture of metal-based sorbents is generally monitored by common thermogravimetric analyses due to the changes in the weight of solid. There are two reactions in the cyclic process: carbonation and calcination/regeneration. In the carbonation

process, the calcium oxide reacts with CO_2 forming calcium carbonate releasing heat since it has an exothermic nature. This heat could be recovered for electricity generation or to contribute to a possible endothermic cracking of hydrocarbon. The weight changes of material are characterized by two stages being (i) the kinetic regime that presents a fast change in the weight due to the formation of $CaCO_3$ layer in the external and internal surface of the material and (ii) diffusion regime which are sluggish and are limited by CO_2 diffusion through of $CaCO_3$ product layer formed during the first stage. This slow feature in this second stage is explained by the difference of two orders of magnitude between the diffusion coefficient of CaO (D_{CaO} = 0.3 cm^2/s) and $CaCO_3$ (D_{CaCO3} = 0.003 cm^2/s). It has been evidenced that the transition between the two stages is related to the thickness of the calcium carbonate product layer which needs to be approximately higher than 50 nm.[18, 19]

The optimal operating temperature for the carbonation and regeneration process could be given by analyzing the equilibrium partial pressure of CO_2 as a function of temperature (correlation of Barin and Platzki (1995)) as shown in Figure 2.7[20]. Thus, the range of carbonation temperature is 550 °C – 700 °C for calcium oxide which could provide an advantage in the systems that operate at high temperatures. On the other hand, the endothermic regeneration needs elevated temperatures (above 900 °C).

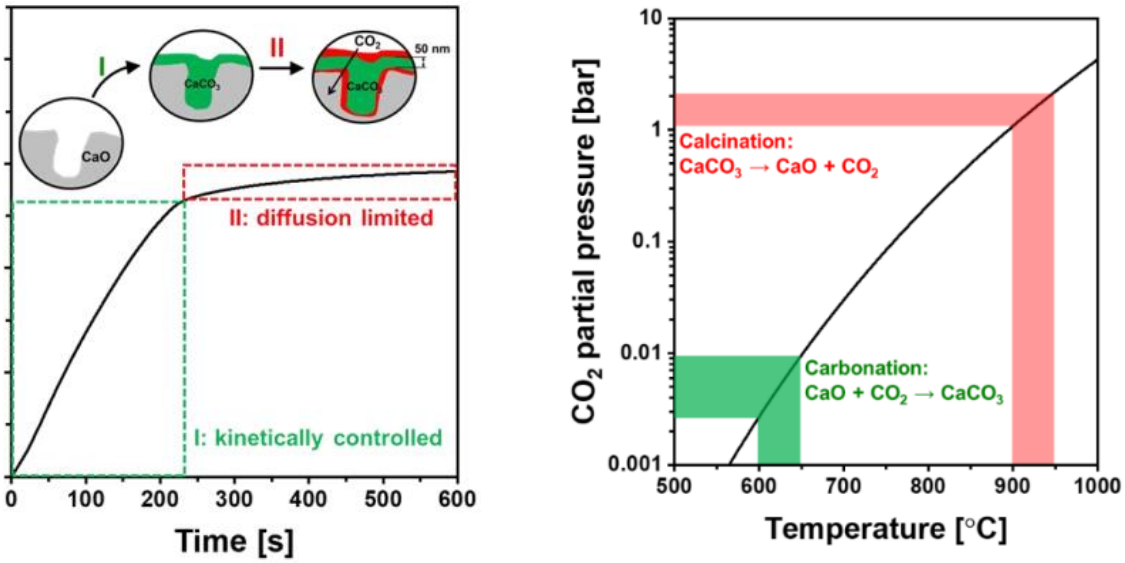

Figure 2.7: (a) CO_2 uptake of limestone in the 1st cycle as a function of carbonation time. The inset visualizes schematically the reaction regimes during carbonation. (b) Equilibrium partial pressure of CO_2 for the carbonation/calcination reaction as a function of temperature using the correlation of Barin and Platzki (1995). (Reproduced with permission from ref.[20] Copyright 1995 Wiley.)

Although CaO has some benefits as a CO_2 sorbent, the major disadvantages of the applicability to the industrial process are the poor stability and decrease in the sorption capacity with some repeated carbonation and calcination cycles. The thermal sintering of $CaCO_3$ during the regeneration stage is associated with the low Tammann temperature of $CaCO_3$ (~533 °C) which is below the calcium looping operation temperature (e. g. 650 °C – 900 °C). This Tammann temperature is defined as the temperature at which the atoms or molecules of the solid acquired sufficient energy for their bulk mobility and reactivity to become appreciable. In addition, another drawback of CaO is the substantial and large volumetric changes that occur since the molar volume of $CaCO_3$ (36.9 cm^3/mol) is more than twice as high as that CaO (16.7 cm^3/mol).[21] Therefore, the sintering phenomenon consists in the agglomeration of small particles, the change of pore shapes, and the pore shrinkage (Figure 2.8). The capacity decay of CaO sorbents depends on the operation temperature, the precursor type, multicycle quantity, and duration of the regeneration stage.

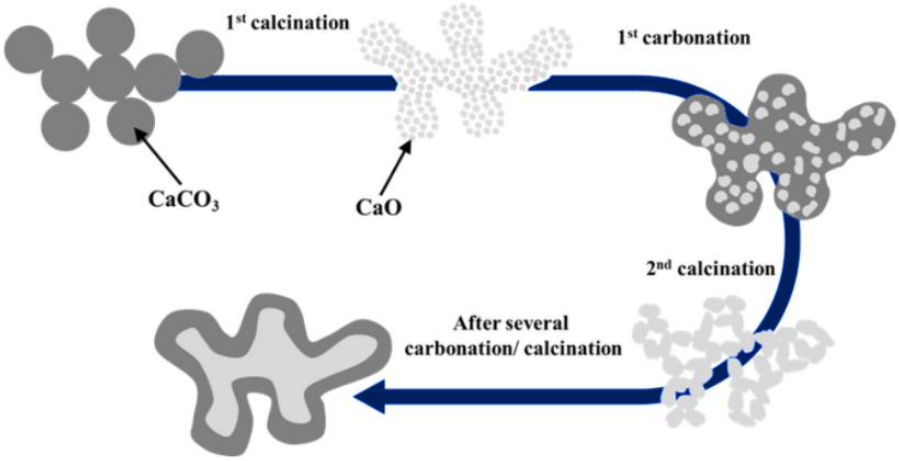

Figure 2.8: Schematic sketch of the morphological transformation of CaO-based CO_2 sorbents over multiple carbonation-calcination cycles.[22]

Some attempts need to be considered to overcome the drawbacks presented by CaO and to develop a sorbent more stable and effective for CO_2 adsorption. Some alternatives are (i) reactivation and use of additional treatment of sorbent[23-33], (ii) the application of various sources of calcium to produce CaO sorbent[34-36], (iii) synthesis method[37-52], (iv) incorporation of stable inert material into CaO structure[37, 38, 53-56], and (v) doping with alkali metals (Li, Na, K) salts[57-66].

2.2.1 Additional treatments

The CO_2 capacity and stability in a multicycle process of natural or synthetic calcium oxide could be enhanced by the application of several additional treatments such as hydration, thermal pretreatment, and chemical pretreatment. Some of these methods will be briefly exemplified and discussed below.

The hydration process consists of the addition of water/steam during some stage of the carbonation/calcination operation and it is classified in hydration treatment during carbonation, hydration treatment during calcination, and in a separated hydration process before or after the sorption process or regeneration.[67] The increase in carbonation conversion is explained by two different theories as described in the work published by Yancheshmeh et al.[68]: (i) the enhancement of carbonation conversion in the fast kinetically-controlled stage by the formation of $Ca(OH)_2$ as a transient intermediate, which carbonation is thermodynamically more favorable than that of CaO[69-72] and (ii) the enhancement of solid-state diffusion in the calcium carbonate product layer, which is more pronounced at lower carbonation temperature and for more sintered sorbents.[67, 73] Notably, the hydration could form cracks and larger pores in the interior of CaO particles making them less susceptible to pore blockage. Manovic and Anthony[74] evaluated the reactivation of spent limestone by steam treatment in a pressurized reactor at 200 °C. The results of activity tests showed that the reactivated sorbent exhibited the average CO_2 capture capacity around 0.55 g CO_2/g sorbent over 10 cycles, which was significantly higher than that of the original sorbent (0.27 to 0.31 g CO_2/g sorbent).

Although the hydration treatment could lead to some improvement in the CO_2 capacity, the method significantly increases the attrition tendency, which restricts the possible industrial application. Moreover, the costs associated with the steam generation could increase considerably the final cost of the process which is the matter concern about the feasibility of this strategy. In addition, pelletization can be an alternative to decrease the negative impact on the mechanical strength of sorbents by hydration treatment.[73, 75, 76]

Other treatments can be applied to improve the physical characteristics in the natural limestone as well as in Ca-based synthetic sorbents. Ridha et al.[32] investigated the application of acetification treatment before the pelletization to overcome the mechanical fragility of sorbent produced by limestone. Calcium aluminate was used as a binder to produce the pellets and the content was 10-14 wt.%. For acetification, acetic acid solution (10 vol.%) and commercial vinegar were used in the form of aqueous solution and vapor. The authors

demonstrated that the acetification of limestone with binder enhanced the CO_2 capture performance. The results showed that the acetified pellets captured 41% more CO_2 than un-acetified pellets after 10 cycles under severe calcination conditions at 920 °C in CO_2. However, the test with a synthetic mixture of 15% CO_2, 3% O_2, 0.45% SO_2, and 81.45% N_2 evidenced a problem related to acetification treatment. The reactivity of pellets with SO_2 is enhanced due to the expansion of the pores resulting in a necessity of complete removal of SO_2 from the flue gas before the CO_2 capture. Li et al.[25] evaluated the performance of CaO modified with ethanol/water during 15 cycles of carbonation calcination cycles. For that, calcium oxide derived by limestone was modified with 50%, 70%, and 90% ethanol/water solutions. As a result, all modified CaO sorbents had a higher carbonation conversion than CaO hydrated with distilled water. Also, a higher concentration of ethanol/water led to better results in CO_2 capture capacity and anti-sintering performance. Also, the specific surface area and pore volume of modified CaO were higher than the hydrated and calcined limestone. The authors elucidated that the ethanol molecule enhances H_2O molecule affinity and penetrability to CaO in the hydration reaction, which provides an expansion in the pores after the sorbent calcination.

Besides the aforementioned works regarding the additional treatment process, Table 2.1 shows some other examples that employed chemical treatments and preheat treatment.

Table 2.1: Summary of investigations on treated CaO sorbent. (Reprinted from ref.[68] Copyright 2016 with permission from Elsevier.)

Sorbent	Treated by	Reaction conditions		Reactor	N° of cycles	CO_2 uptake at last cycle	Ref
		Adsorption	Regeneration			(g CO_2/g ads)	
Limestone	Acetic acid	650 °C, 15% CO_2, 20 min	920 °C, 80% CO_2, 15 min	DFR	20	0.39	[23]
Limestone	Propionic acid	700 °C, 15% CO_2, 20 min	850 °C, 100% N_2, 10 min	DFR	100	0.24	[26]
Limestone	Pyroligneous acid	700 °C, 15% CO_2, 30 min	850 °C, 100% N_2, 15 min	DFR	103	0.26	[27]
Limestone	Citric acid	700 °C, 15% CO_2, 30 min	750 °C, 100% Ar, 30 min	TGA	18	0.485	[24]
Limestone	Ethanol	700 °C, 15% CO_2, 20 min	920 °C, 80% CO_2, 15 min	DFR	15	0.31	[25]
$Ca(Ac)_2$	Ethanol/water (3:1)	600 °C, 50% CO_2, 45 min	700 °C, 100% N_2, 20 min	TGA	11	0.62	[28]
Limestone	Acetic acid	650 °C, 15% CO_2, 20 min	920 °C, 100% CO_2, 10 min	TGA	20	0.09	[32]
Limestone	Acetic acid	650 °C, 15% CO_2, 20 min	850 °C, 100% N_2, 5 min	TGA	20	0.23	[33]
Limestone	Vinegar	650 °C, 15% CO_2, 20 min	850 °C, 100% N_2, 5 min	TGA	20	0.15	[33]
Limestone	Formic acid	650 °C, 15% CO_2, 20 min	850 °C, 100% N_2, 5 min	TGA	20	0.22	[33]
Limestone	Oxalic acid	650 °C, 15% CO_2, 20 min	850 °C, 100% N_2, 5 min	TGA	20	0.25	[33]
Limestone	10 wt.% Aluminate cement, 10% Starch	700 °C, 15% CO_2 in air, 30 min	900 °C, 100% air, 20 min	-	10	~0.65	[29]
Limestone	Steam (hydration)	650 °C, 15% CO_2 in air, 15 min	940 °C, 70% CO_2 in air, 20 min	FB	5	0.37	[30]
Limestone	Liquid water and steam hydration	780 °C, 100% CO_2, 40 min	960 °C, 100% N_2, 35 min	TGA	100	0.23	[31]

Notes: DFR = Dual Fixed-bed Reactor, TGA = Thermogravimetric Analyzer, FB = Fluidized Bed Reactor

2.2.2 Calcium precursors and synthesis technique

Calcium oxide has been widely used for CO_2 capture due to low-cost raw material, availability, and a good CO_2 capacity. Thereby, the most used precursor to produce the sorbent is the natural limestone or dolomite.[77] Other precursors include calcium hydroxide ($Ca(OH)_2$), calcium nitrate ($Ca(NO_3)_2$), calcium acetate ($Ca(CH_3COO)_2$), calcium oxalate (CaC_2O_4), and organometallic precursors (e.g. calcium D-gluconate monohydrate, calcium L-lactate hydrate, calcium formate, calcium citrate tetrahydrate, and calcium acetate hydrate).

Lu et al.[34] studied the influence of different precursors including $Ca(NO_3)_2.4H_2O$, $Ca(OH)_2$, $CaCO_3$, and $Ca(CH_3COO)_2.H_2O$ for calcium oxide synthesis. Among them, the sorbent prepared using $Ca(CH_3COO)_2.H_2O$ presented almost 100% carbonation at temperatures between 550 °C and 800 °C and, after 27th cycle carbonation/regeneration experiment, the molar conversion of CaO remained at 62% at 700 °C (mild conditions). Consequently, they concluded that the best precursors were the calcium acetate monohydrate achieving a high carbonation capacity with excellent stability over multiple capture cycles. Regarding $Ca(NO_3)_2$, the authors identified a bad performance with a low uptake capacity of CO_2 that was attributed to a low surface area caused by the low melting temperature of the precursor (561 °C). Martavaltzi et al[35] synthesized CO_2 sorbent using two different microporous CaO precursors, $Ca(OH)_2$ and $Ca(CH_3COO_2)$. With a similar conclusion obtained by Lu et al.[34], the calcined calcium acetate showed the highest CO_2 uptake capacity with 50% weight change of CaO at 690 °C and in a flow of 15% of CO_2 in N_2. Although, they observed decay in sorption capacity for both synthesized material over multicycle experiments. For this reason, they decided to evaluate the addition of an inert $Ca_{12}Al_{14}O_{33}$ to CaO by mixing. As a result of inert addition, the sorbent prepared with calcium acetate was more stable than prepared with calcium hydroxide. The inhibition of the sintering process of calcium oxide was associated with uniform dispersion and stabilization of the framework by $Ca_{12}Al_{14}O_{33}$.

The use of organometallic precursors for calcium oxide synthesis was also studied in the literature. One example is the work by Liu et al.[36] that compared the capacity for capturing CO_2 of 9 different precursors including organometallic salts, hydroxides, and carbonates. The organometallic salts exhibited higher surface areas and best initial conversions than carbonates and hydroxides. Notably, the D-gluconate

monohydrate showed great stability in addition to an increase in conversion for the first four cycles. The authors attributed this performance to a self-reactivation phenomenon due to a rearrangement in the crystal structure of the sorbent.

Furthermore, several synthesis techniques have been studied to produce a Ca-based sorbent with a high surface area and pore volume, as well as, to promote a high dispersion of inert into the structure. Some examples of these techniques are:

- wet mixing[35, 37, 38, 45-47];
- limestone acidification by citric acid followed by two-step calcination[48];
- solid-state reaction[49];
- ultrasonic spray pyrolysis (USP)[50];
- combination of precipitation and hydration[51];
- co-precipitation[52];
- citrate preparation[39];
- sol-gel[40, 41];
- citrate-assisted sol-gel technique followed by two-step calcination[42];
- single nozzle flame spray pyrolysis (FSP)[43];
- precipitation[44].

2.2.3 Supported CaO-based sorbent

The incorporation of inerts into the calcium oxide structure is one of the most studied approaches to mitigate the sintering phenomenon. This technique has been shown efficient to improve the stability of CaO derived from synthetic precursors. Basically, it consists of the addition of a support material that has a high Tammann temperature. Thus, during the synthesis, the inert material is dispersed among the CaO particles which inhibit the CaO grain sintering during the carbonation/calcination cycles. Among the inert support materials, there is aluminum oxide (Al_2O_3), zirconium oxide (ZrO_2) magnesium oxide (MgO), silica (SiO_2), titanium oxide (TiO_2), and yttrium oxide (Y_2O_3).

Due to the vast literature about this technique and different synthesis methods, some selected articles will be discussed. Zhou et al.[37] prepared an Al-stabilized CaO sorbent by wet mixing method using different calcium and aluminum

precursors. It is well reported by the literature and it was evidenced by the authors that the Al-stabilized phase, including Al_2O_3, $Ca_{12}Al_{14}O_{33}$, $Ca_9Al_6O_{18}$ or $Ca_3Al_2O_6$ could be formed depending on calcium and aluminum precursors used during the preparation. The experimental results revealed that all Al-stabilized CaO sorbents exhibited higher CO_2 sorption capacity and stability during the cycles than pure CaO. The authors attributed this good performance to features such as high specific surface area, an adequate number of small pores, and the uniform distribution of inert support among the CaO particles. The best sorbent was the $CaO/Ca_9Al_6O_{18}$ derived from calcium citrate and aluminum nitrate with CO_2 capture capacity of 0.51 g CO_2/g of sorbent after 28 cycles. They also proposed a mechanism to elucidate the formation of inert support as represented in Figure 2.9. The mechanism is based on the solid-state reaction between CaO and Al_2O_3 which were controlled by diffusion of Ca^{2+} through the reaction interface in the transition of steps 3 and 4.

$$\text{Ca \& Al precursors} \xrightarrow[-CO_2,-H_2O]{(1)} CaCO_3 + Al_2O_3 \xrightarrow[-CO_2]{(2)} CaO + Al_2O_3$$
$$\xrightarrow{(3)} Ca_{12}Al_{14}O_{33} \xrightarrow[CaO]{(4)} Ca_9Al_6O_{18}$$

Figure 2.9: Possible mechanism for Al-stabilizer formation (Reprinted from ref.[37]. Copyright 2012 with permission from Elsevier.)

Pacciani et al.[38] synthesized some sorbents based on calcium oxide supported in $Ca_{12}Al_{14}O_{33}$ with different CaO/inert material ratios. The preparation techniques were coprecipitation and hydrolysis and the amount of each precursor was selected to obtain the mass ratio of CaO to inert in the final sorbent equal to 25:75, 50:50, 63:37, 75:25, or 85:15. After that, these materials were tested using a fluidized bed reactor. The sorbent with 15 wt.% of $Ca_{12}Al_{14}O_{33}$ showed the highest CO_2 capture capacity (0.26 g CO_2/g sorbent after 20 cycles) and mechanical strength. In addition, the mechanical strength was attributed to the presence of mayenite into the material structure which provided a better attrition property than those supported on MgO.

Identically to Al-stabilizer, the addition of ZrO_2 has been widely applied as inert material for stabilization of calcium oxide structure. The Zr/Ca molar ratio[78, 79], precursors[48], and method synthesis parameters[43, 80] were the focus of several studies in the literature. Lu et al.[53] investigated the addition of refractory dopants (Si, Ti. Cr, Co,

Zr, and Ce) as support in Ca-based sorbents using flame spray pyrolysis (FSP). The purpose was to develop sorbents with good mechanical strength for CO_2 capture system. The calcium doped with zirconium exhibited the best CO_2 capture performance. Additionally, they found that the optimum Zr/Ca molar ratio was 0.3, which lead to the best reactivity. The sorbent also demonstrated excellent stability, operating in the presence of water vapor in the feed stream (10 vol.%). Thereby, the good CO_2 capacity and thermal stability were associated with the formation of nano-size particles, high surface area and large pore volume, and the presence of the refractory stabilizer. In a further study, the same research group investigated a wide range of zirconia loadings into CaO structure via the flame spray pyrolysis (FSP).[54] The Zr/Ca sorbent with molar ratio of 5/10 exhibited excellent CO_2 capture capacity and good stability up to 1200 cycles comparing with the other synthesized materials. Even in severe conditions, the sorbent presented an excellent resistance which was justified by the formation of well-dispersed $CaZrO_3$ nanoparticles that act as a barrier against sintering, preventing the CaO grain growth.

Although the FSP is a good method to produce an excellent Zr-doped CaO sorbent, the complexity of the technique can be the main difficulty for the implementation and large production in the industrial sector. Zhao et al.[55] synthesized a series of CaO-based sorbent with different inert material ($CaSiO_4$, $Ca_3Al_2O_6$, $CaTiO_3$, $CaZrO_3$, and MgO) using a simple citrate sol-gel method. They evaluated the cyclic CO_2 capture capacity and stability during the carbonation/calcination cycles and investigated the structure-property relationship of the sorbents. They observed significant effects on the sorbent structure and performance caused by parameters such as complexation time, dispersion agent, calcium precursor, and inert material. Among the synthesized sorbents, the best performance was presented by CaO stabilized with $CaZrO_3$ (29.1 wt.%) that had a stable CO_2 capture capacity of 0.45 g CO_2/g sorbent over 30 cycles. The reason for this excellent performance was ascribed to the small grains, accessible pores, and homogeneous distribution of the constituents CaO and $CaZrO_3$ in the sorbent.

Hu et al.[56] published a work to provide the basis and guideline for the selection of inert solid refractories that can be added in the calcium oxide sorbent. They selected 12 different refractories including Al-, Ti-, Mn-, Mg-, Y-, Si-, La-, Zr-, Ce-, Nd-, Pr- and Yb-based supports. All these sorbents were prepared by the same wet-mixing method and tested in the same carbonation/calcination conditions (carbonation: 650 °C

under 30% CO_2 for 25 min and calcination: 800 °C under 100% N_2 for 5 min). Figure 2.10 shows the cyclic performance of all the sorbents for 15 cycles. Briefly, the Y- and Al-based supports exhibited much superior performance than the other supported materials. Additionally, they found a relationship between the melting point and surface area with the comprehensive performance (combination of cyclic capacity and capacity loss rate – $N_{sorbent}$) as can be seen in Figure 2.11a and 2.11b. Higher values of $A_{sorbent}$ indicates the worse sintering resistant ability while higher $N_{sorbent}$ values means the better comprehensive performance for the synthetic sorbent. The performance was significantly affected by the melting point of inert support and surface area of synthetic sorbents. In essence, support with a higher melting point and a better dispersion presented better resistance against the sintering process. Furthermore, the authors summarized some results of the performance of CaO-based sorbents stabilized by different inert supports presented in the literature (Table 2.2).

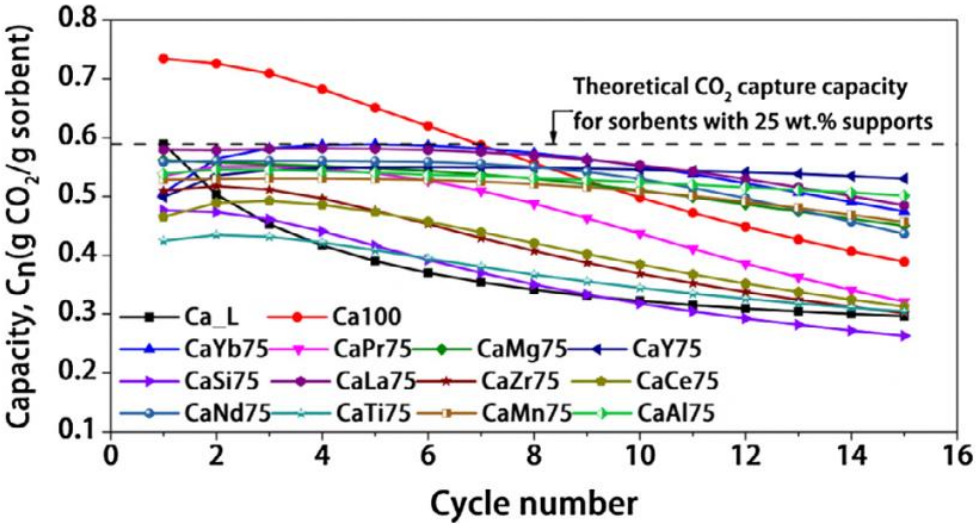

Figure 2.10: Cyclic performance of the synthetic sorbents under 'mild' conditions (calcination: 800 °C, 100% N_2, 5 min; carbonation: 650 °C, 30% CO_2, 25 min). (Reprinted from ref.[56]. Copyright 2016 with permission from Elsevier.)

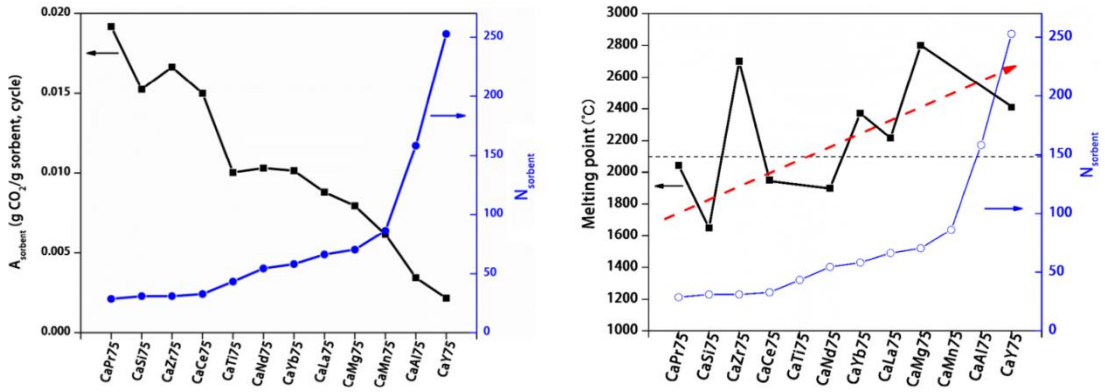

Figure 2.11: (a) Comparison of $A_{sorbent}$ and $N_{sorbent}$ for different synthetic sorbents; (b) The relationship between the melting points of supports and the comprehensive performance. (Reprinted from ref.[56]. Copyright 2016 with permission from Elsevier.)

Table 2.2: Summary of investigations on metal oxide stabilized CaO-based sorbents. (Data (adapted) from ref.[56] Copyright 2016 with permission from Elsevier.)

Authors	Supports (wt.%)	Calcination Conditions			Carbonation conditions			Cycle n°	Last-cycle capacity (g/g)	Ref.
		T (°C)	Atmosphere	t (min)	T (°C)	Atmosphere	t (min)			
Li et al.	$Ca_{12}Al_{14}O_{33}$ [25%]	950	20% CO_2	10	690	14% CO_2	30	13	0.33	[47]
Li et al.	$Ca_{12}Al_{14}O_{33}$ [25%]	980	100% CO_2	5	650	100% CO_2	30	56	0.22	[46]
Martavaltzi and Lemonidou	$Ca_{12}Al_{14}O_{33}$ [25%]	850	100% N_2	5	690	15% CO_2	30	45	~0.30	[35]
Martavaltzi and Lemonidou	$Ca_{12}Al_{14}O_{33}$ [25%]	850	100% N_2	10	690	15% CO_2	30	45	0.27	[81]
Broda et al.	$Ca_{12}Al_{14}O_{33}$ [17.84%]	900	100% N_2	10	650	20% CO_2	20	30	0.25	[82]
Broda and Müller	$Ca_{12}Al_{14}O_{33}$ [17.84%]	750	100% N_2	20	750	40% CO_2	20	30	~0.53	[40]
Koirala et al.	$Ca_{12}Al_{14}O_{33}$ [41.65%]	950	30% CO_2	10	850	100% CO_2	10	100	~0.25	[43]
Stendardo et al.	$Ca_{12}Al_{14}O_{33}$ [25%]	1000	86% CO_2	15	600	14% CO_2	25	200	~0.09	[49]
Luo et al.	$Ca_{12}Al_{14}O_{33}$ [20%]	950	15% CO_2	2.5	650	15% CO_2	2.5	100	0.13	[83]
Radfarnia and Iliuta	$Ca_9Al_6O_{18}$ [22.1%]	930	30% CO_2	10	650	30% CO_2	30	25	~0.23	[48]
Radfarnia and Sayari	$Ca_9Al_6O_{18}$ [20%]	930	100% CO_2	5	650	100% CO_2	30	31	0.33	[42]
Li et al.	$Ca_3Al_2O_6$ [25%]	850	100% N_2	5	650	16% CO_2	30	15	0.2	[46]
Li et al.	$Ca_3Al_2O_6$ [25%]	850	100% N_2	10	700	15% CO_2	30	50	0.38	[84]
Aihara et al.	$CaTiO_3$ [70.8%]	750	100% N_2	60	750	20% CO_2	60	10	0.14	[85]
Wu and Zhu	$CaTiO_3$ [28.15%]	750	100% N_2	10	600	20% CO_2	10	40	0.23	[86]
Lu et al.	$CaZrO_3$ [57.8%]	700	100% He	30	700	30% CO_2 + 10% H_2O	30	100	~0.21	[53]
Koirala et al.	$CaZrO_3$ [76.17%]	700	100% He	30	700	99.5% CO_2	30	1200	0.11	[54]
Radfarnia and Iliuta	$CaZrO_3$ [58%]	750	100% Ar	30	700	100% CO_2	30	15	~0.25	[78]
Broda and Müller	$CaZrO_3$ [26.2%]	800	100% N_2	~15	800	50% CO_2	5	90	0.34	[80]

Authors	Supports (wt.%)	Calcination Conditions			Carbonation conditions			Cycle n°	Last-cycle capacity (g/g)	Ref.
		T (°C)	Atmosphere	t (min)	T (°C)	Atmosphere	t (min)			
Zhao et al.	$CaZrO_3$ [30%]	950	100% CO_2	0	650	100% CO_2	15	30	0.31	[79]
Luo et al.	Ca_2MnO_4 [20%]	950	15% CO_2	2.5	650	15% CO_2	2.5	100	0.07	[83]
Albrecht et al.	MgO [20%]	750	100% N_2	30	750	25% CO_2	20	1250	0.17	[87]
Li et al.	MgO [42%]	758	100% N_2	30	758	100% CO_2	30	70	~0.44	[88]
Radfarnia and Iliuta	MgO [6.7%]	750	100% Ar	30	650	15% CO_2	30	25	~0.31	[48]
Luo et al.	MgO [20%]	950	100% CO_2	2.5	650	15% CO_2	2.5	100	0.15	[83]
Lan and Wu	MgO [25%]	850	100% N_2	6	650	20% CO_2	10	51	0.27	[89]
Li et al.	$MgAl_2O_4$ [10%]	758	100% CO_2	30	758	100% CO_2	30	132	~0.45	[90]
Derevschikiov et al.	Y_2O_3 [80.1%]	740	100% Ar	10	740	24.67% CO_2	10	190	~0.077	[91]
Radfarnia and Iliuta	Y_2O_3 [16.8%]	750	100% Ar	30	650	15% CO_2	30	25	~0.27	[48]
Zhang et al.	Y_2O_3 [20%]	950	100% CO_2	5	650	20% CO_2	30	10	~0.48	[92]
Radfarnia and Iliuta	ZrO_2 [23.1%]	750	100% Ar	30	650	15% CO_2	30	25	~0.22	[48]
Lu et al.	ZrO_2 [39.7%]	750	100% He	10	750	30% CO_2	10	50	~0.10	[53]
Radfarnia and Iliuta	Al_2O_3 [8.3%]	750	100% Ar	30	650	15% CO_2	30	25	~0.26	[48]
Zhao et al.	SiO_2 [34.9%]	700	100% N_2	5	600	66.7% CO_2	60	50	0.33	[93]
Lu et al.	SiO_2 [9.68%]	700	100% He	30	700	30% CO_2	30	100	~0.26	[53]
Radfarnia and Iliuta	TiO_2 [16.56%]	750	100% N_2	10	600	20% CO_2	10	40	~0.187	[86]
Wu and Zhu	Nd_2O_3 [70%]	1000	100% N_2	5	650	15% CO_2	30	100	0.04	[94]
Hu et al.	La_2O_3 [20%]	950	15% CO_2	2.5	650	15% CO_2	2.5	100	0.06	[83]
Lu et al.	CeO_2 [23.5%]	700	100% He	30	700	30% CO_2	30	100	~0.19	[53]
Wang et al.	CeO_2 [15%]	700	100% N_2	20	600	50% CO_2	45	18	0.59	[95]

Table 2.2: Summary of investigations on metal oxide stabilized CaO-based sorbents (continued)

2.2.4 Doping calcium oxide

The addition of alkaline metal components into metal oxide is another approach that has been received much attention in the last years. In recent works, the improvements such as good stable sorption uptake, good oxygen mobility and CO_2 diffusion, and fast sorption kinetics in metal oxide sorbents were attributed to the addition of molten salts.

Concerning doping by alkaline metals, Reddy et al.[57] synthesized several basic sorbents based on CaO which was tested for the sorption of CO_2. The authors examined the effect of promoting the surface with alkaline metals which are known to generate basic or super basic surface on alkaline-earth-metal oxides. For this purpose, the sorbents were prepared with 20 wt.% of alkali metal (Li, Na, K, Rb, and Cs) and CaO using wet impregnation and tested under 40 vol.% CO_2 in helium at different adsorption temperatures such as 50, 450, 600, and 700 °C in a thermogravimetric analyzer (TGA). In general, the sorbents exhibited a high CO_2 sorption capacity, rapid sorption/desorption, and high selective chemisorption of CO_2 as shown by TGA results. The good performance was attributed to the basic nature which was highlighted as the key feature of this family sorbents. Also, the increase in CO_2 sorption capacity follows the increase in atomic radii of the alkaline metals (Li < Na < K < Rb < Cs). This trend was associated with the change of electropositivity of the alkali metals, which increase from top to bottom in the periodic table. Figure 2.12 shows the results of CO_2 sorption experiments at 600 °C which illustrate this tendency in the performance of the studied sorbents. Additionally, using X-ray photoelectron spectroscopy (XPS) analyses, they observed hardly any affinity with other elements (N_2, O_2, and water) in the most effective sorbent (Cs/CaO). The Cs precursor had an important influence on the CO_2 sorption performance. CsOH- and Cs_2CO_3-doped CaO provide significantly higher adsorption of CO_2 than CsCl justified by the formation of a highly dispersed Cs_2O on the CaO support.

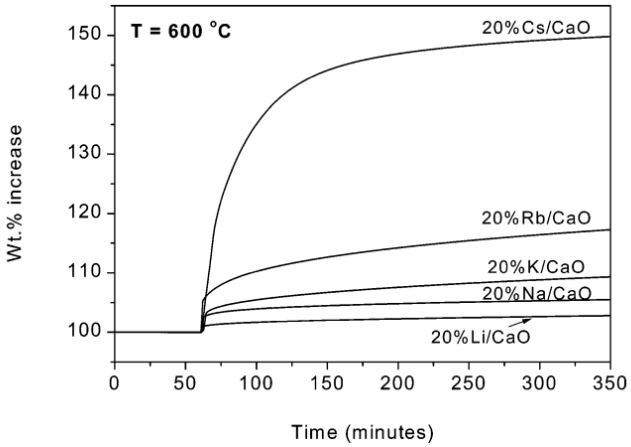

Figure 2.12: CO_2 adsorption on CaO doped with akali metal hydroxides at 600 °C. (Conditions: concentration of CO_2 = 99.999%; flow = 50 mL/min (40% CO_2/He)). (Reprinted with permission from ref. [57] Copyright 2004 American Chemical Society.)

Although using a moderate adsorption temperature and magnesium as the CO_2 captor, Lee et al.[58] obtained interesting results for Na-Mg double salt sorbents. First, the sorbents were prepared using the precipitation method. After that, they evaluated the properties and CO_2 sorption behavior in a temperature range of 300-500 °C. The results showed high CO_2 sorption uptake for the Na-Mg double salt at 375 °C (about 3.48 mol/kg – 15.3 wt.%) and good stability during the carbonation/calcination cycles. Furthermore, they pointed out characteristics such as fast CO_2 sorption/desorption kinetics, high regeneration capacity, and high CO_2 sorption capacity which make this a promising system for further application.

To better understand these positive effects, the CO_2 sorption mechanism was proposed using a theoretical sorption model. The reaction between CaO and sorbate CO_2 to produce $CaCO_3$ is exothermic and thermodynamically controlled. Thereby, Bhatia et al.[96] proposed a mechanism in the system CaO-$CaCO_3$-CO_2 in which Ca^{2+} and CO_3^{2-} ions are predominant in $CaCO_3$. They postulated that the CO_3^{-2} is the mobile species in ionic conduction through $CaCO_3$ and the O^{2-} ions, generated from the sorbent surface, are a counter-current of a negatively charged species to maintain electroneutrality. According to the studies[57, 97, 98], the addition of dopant components can decrease the enthalpy change (ΔH) for the carbonation of metal oxides such as CaO and MgO. Wu et al.[59] suggested theoretical models based on free ion migration for the carbonation of metal oxide-based sorbents. From the previous results, Lee et al.[60] describe and schematize (Figure 2.13) the following order for CO_2 sorption

mechanism of Na_2CO_3-doped CaO sorbent which was represented by Equations 2.2 to 2.6.

i. gas-phase CO_2 adsorbs onto the sorbent surface;
ii. free O^{2-} ions are derived from CaO at high temperatures as $[Na_2Ca(CO_3)]^{2+}$ is co-generated to compensate the charge;
iii. the adsorbed CO_2 combines with an O^{2-} ion to form CO_3^{2-};
iv. the anion reacts with $[Na_2Ca(CO_3)]^{2+}$ and the double salt $Na_2Ca(CO_3)_2$ is generated after the Na_2CO_3 dopant is fully converted to the double salt by reacting with CaO and CO_2;
v. the CO_3^{2-} ion continues reacting with CaO to produce $CaCO_3$.

$$CO_2(g) \rightleftharpoons (CO_2)_{ads} \quad \text{Eq. 2.2}$$

$$Na_2CO_3 + CaO \xrightarrow{k_1} [Na_2Ca(CO_3)]^{2+} + O^{2-} \quad \text{Eq. 2.3}$$

$$O^{2-} + (CO_2)_{ads} \underset{k_3}{\overset{k_2}{\rightleftharpoons}} CO_3^{2-} \quad \text{Eq. 2.4}$$

$$[Na_2Ca(CO_3)]^{2+} + CO_3^{2-} \xrightarrow{k_4} Na_2Ca(CO_3)_2 \quad \text{Eq. 2.5}$$

$$CO_3^{2-} + CaO \xrightarrow{k_5} CaCO_3 + O^{2-} \quad \text{Eq. 2.6}$$

where k_i is the rate constant for each reaction. Finally, the double salt formation reaction can be described as a function of the coverage ratio θ in Equation 2.7, and the coverage ratios are related as in Equations 2.8 and 2.9.

$$r = k_4 \theta_{Na_2Ca(CO_3)^{2+}} \theta_{CO_3^{2-}} \quad \text{Eq. 2.7}$$

$$\theta_{Na_2Ca(CO_3)^{2+}} = k_1 \theta_{Na_2CO_3} \theta_{CaO} \quad \text{Eq. 2.8}$$

$$k_3 \theta_{CO_3^{2-}} = k_2 \theta_{O^{2-}} \theta_{(CO_2)_{ads}} \quad \text{Eq. 2.9}$$

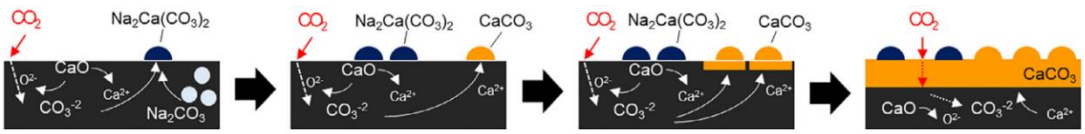

Figure 2.13: CO_2 sorption mechanism onto the Na_2CO_3-CaO sorbent. (Reprinted from ref.[60]. Copyright 2018 with permission from Elsevier.)

Also, in this same work, Lee and coworkers prepared Na_2CO_3-CaO sorbent using the precipitation method for application in high-temperature CO_2 sorption process. The *in situ* X-ray diffraction analyses confirmed that the reaction of CO_2 with CaO and Na_2CO_3 in the sorbent to form $Na_2Ca(CO_3)_2$ is favorable compared to conventional carbonation of CaO at relatively low sorption temperatures (600-700 °C) (Figure 2.14). Besides that, the authors developed kinetic models to describe the CO_2 behavior of Na_2CO_3-CaO.

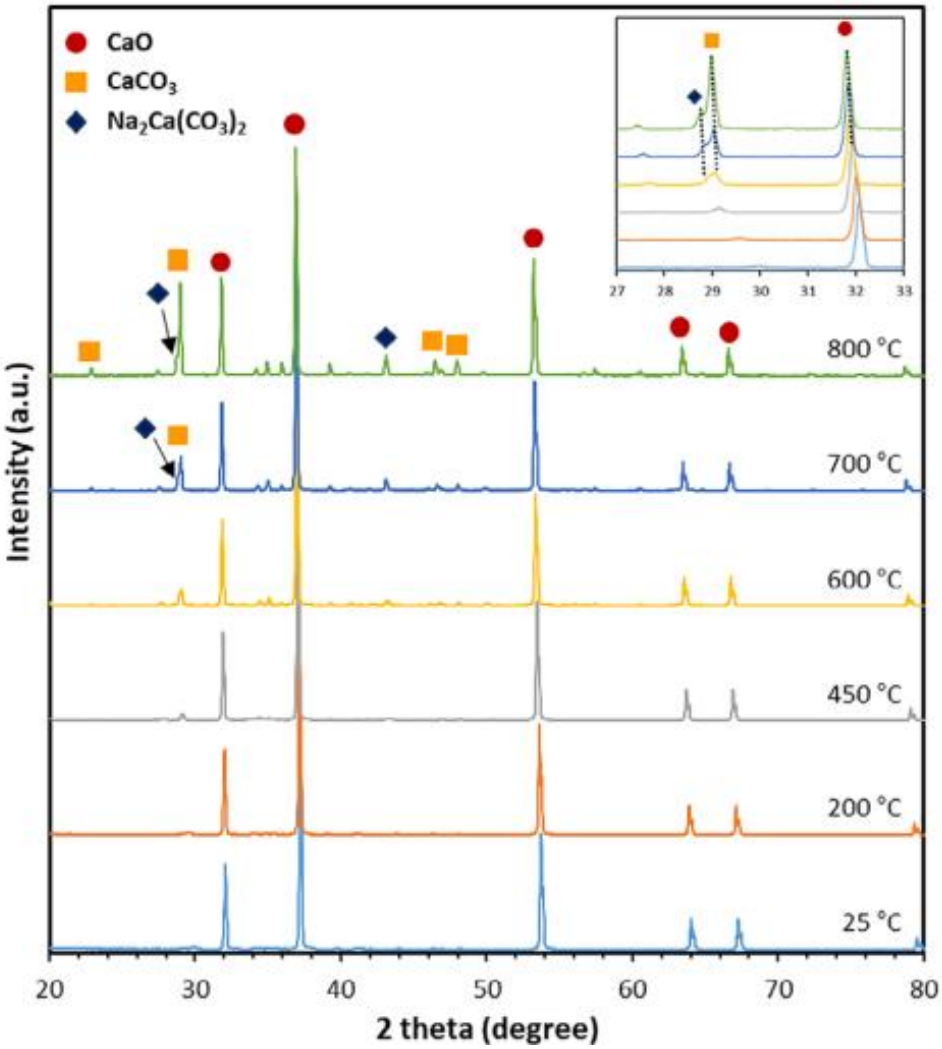

Figure 2.14: *In situ* XRD spectra of Na_2CO_3-CaO at different temperatures in a CO_2 flow. Inset detailed XRD spectra between 27° and 33°. (Reprinted from ref.[60]. Copyright 2018 with permission from Elsevier.)

Al-Mamoori et al.[61] synthesized Na-promoted and K-promoted CaO-based sorbents with various molar ratio Na/Ca and K/Ca using the precipitation technique.

The CO_2 capture performance was evaluated considering the effects of K or Na concentration as well as adsorption temperature which were in a range of 300-400 °C. The optimum CO_2 capacities were obtained at 375 °C and 1 bar with 3.8 mmol/g K-Ca and 3.2 mmol/g Na-Ca which indicate that these sorbents have a relatively high capacity, fast kinetics, and good stability (in the case of K-Ca) as point out by the authors. Furthermore, the influence of a higher temperature range (300-700 °C) on adsorption kinetics and CO_2 capacity was investigated as shown in Figure 2.15. Above the 650 °C, the sorption capacity intensely decreases indicating that the double salts start to decompose losing their effectiveness in the CO_2 capture process. Moreover, the results showed that higher temperature enhances the maximum CO_2 uptake, for instance, reaching 10.7 mmol/g for K/Ca (molar ratio equal to 6.7) and 9.5 mmol/g for Na/Ca (molar ratio equal 4.2) at 650 °C.

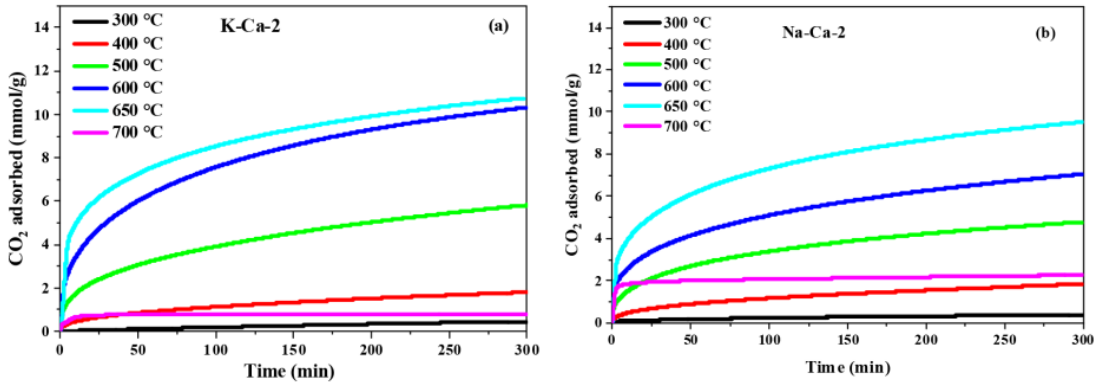

Figure 2.15: CO_2 uptake over (a) K-Ca-2 and (b) Na-Ca-2 double salts as a function of temperature (Reprinted with permission from ref.[61]. Copyright 2017 American Chemical Society.)

In addition to the articles already referenced in this section, it is also worth mentioning others[62-66] that studied the doping with alkaline components as an approach to enhance the performance of metal oxide in CO_2 capture. The application of these materials has been received a widespread focus due to the excellent benefits provided by the sorbents for CO_2 capture. The industrial use of these materials is generally associated with energetic improvements and mitigation of CO_2 emission for the atmosphere. The hydrogen production by steam reforming process is an interesting process to apply these materials and it will be discussed in the next section.

2.3 Hydrogen production

Hydrogen has been vastly applied in several ways over the years. Some examples are the first demonstrations of water electrolysis and fuel cells in the 1800s, the uses as fuel in the first internal combustion engines, as a gas lighter than air to provide the lift to balloons and airships in the 18th and 19th centuries, as a rocket propeller that toolmaking to the moon in the 1960s. Also, hydrogen helped to feed the growing global population due to its presence in ammonia fertilizer and to be an important part of the energy industry since the 20th century (continuous use in oil refining).

Hydrogen presents some characteristics that provide a growing interest in the use. It is light, storable, reactive, has high energy content per unit mass, and can be readily produced at industrial scale.[99, 100] Additionally, two important features are highlighted: (i) hydrogen can be used without direct emissions of air pollutants, particulates, or greenhouse gases; and (ii) it can be made from a diverse range of low-carbon energy sources. It is important to point out that hydrogen is not an energy source but an energy carrier that is very versatile regarding use and production. Also, if it used in a fuel cell, it only produces water. To illustrate the energetic benefits of hydrogen, the physical properties and comparison with common transport fuel are listed in Table 2.3.

Table 2.3: Physical properties of hydrogen.[100] (Source: IEA (2006), Hydrogen Production and Storage, All rights reserved.)

Property	**Hydrogen**	**Comparison**
Density (gaseous)	0.089 kg/m^3 (0 °C, 1 bar)	1/10 of natural gas
Density (liquid)	70.79 kg/m^3 (-253 °C, 1 bar)	1/6 of natural gas
Boiling point	-252.76 °C (1 bar)	90 °C below LNG
Energy per unit of mass (LHV)	120.1 MJ/kg	3x that of gasoline
Energy density (ambient cond., LHV)	0.01 MJ/L	1/3 of natural gas
Specific energy (liquefied, LHV)	8.5 MJ/L	1/3 of LNG
Flame velocity	346 cm/s	8x methane
Ignition range	4-77% in air by volume	6x wider than methane
Autoignition temperature	585 °C	220 °C for gasoline
Ignition energy	0.02 MJ	1/10 of methane

Notes: LHV = lower heating value; LNG = liquified natural gas

The report prepared by International Energy Agency (IEA) presents interesting data about hydrogen demand in different sectors (Figure 2.16). The current demand worldwide for hydrogen is around 115 million tonnes per year (Mt) being that 70 Mt is for "pure" hydrogen and 45 Mt is for hydrogen as part of a mixture gases such as synthesis gas. The "pure" hydrogen has only small levels of additives or contaminants and is mainly used in oil refining and ammonia production for fertilizers while the hydrogen mixtures are utilized in methanol production and steel production.[100]

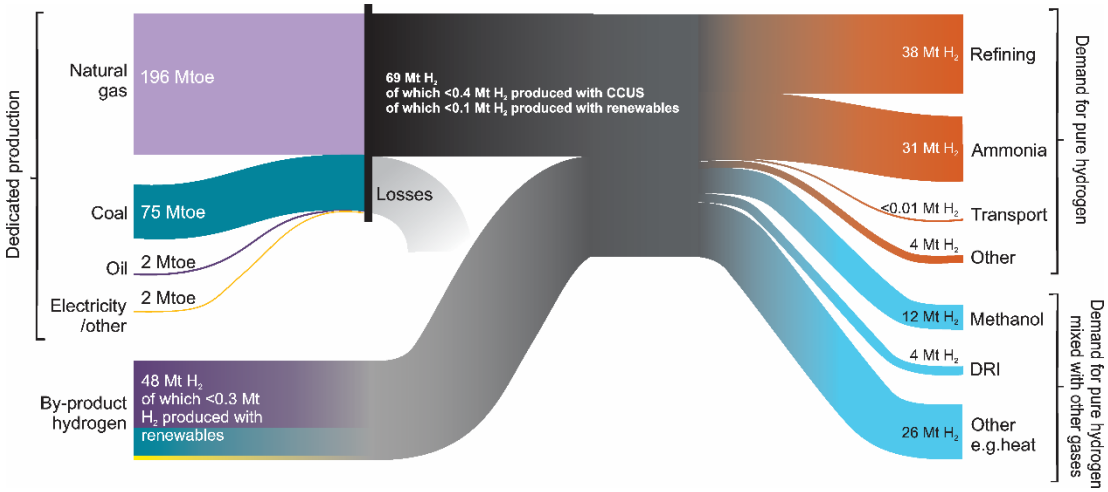

Figure 2.16: Current hydrogen value chains.[99] (Source: IEA (2019), The Future of Hydrogen, All rights reserved.)

To meet the current demand, hydrogen can be produced from several processes and extracted from sources as shown in Figure 2.17.[99-101] Specifically, natural gas is currently the primary source and accounts for around three-quarters of the annual global dedicated hydrogen production of around 70 million tonnes of hydrogen (Mt H_2). The methane steam reformers using natural gas are the main means for hydrogen production in the ammonia and methanol industries and refineries. The next source is coal due to its dominant role in China. In an estimative, China is responsible for 23% of global dedicated hydrogen production and consume 107 Mt of coal (2% of global coal use). The other parcel for dedicated production is filled with oil and electricity.[99]

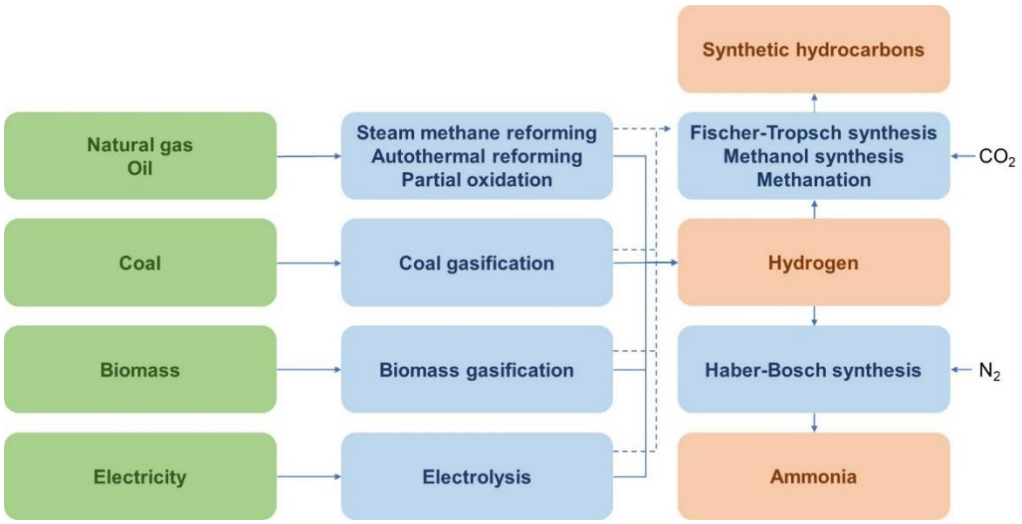

Figure 2.17: Potential pathways for producing hydrogen and hydrogen-based products.[99] (Source: IEA (2019), The Future of Hydrogen, All rights reserved.)

In summary, the majority of hydrogen produced today is from fossil fuels which generate significant CO_2 emissions around 830 Mt CO_2/year. Moreover, in contrast, less than 0.7% of dedicated hydrogen production is from renewables or fossil fuel plants equipped with CCUS, which can produce low-carbon hydrogen. Therefore, producing hydrogen by a cleaner way is essential and vital to reduce the CO_2 emissions to lower levels and, then, to control the rising in global temperature as previously discussed in the background section of this work.

2.3.1 Conventional steam reforming of methane (SRM)

The main commercial routes for hydrogen production are steam reforming, auto-thermal reforming, partial oxidation, and coal gasification. Particularly, the steam reforming of methane (SRM), using nickel as the metallic phase, is the dominating technology for H_2 production and it covers nearly half of the world's H_2 demand. Even though the SRM is a consolidated process in the industry, significant changes are currently required to make this technology more efficient given the changes in climate scenario. It is an energy-intensive process with a poor energy integration since typically operated at severe conditions of temperature and pressure (800-1000 °C and 1.53 MPa).[101-103] Furthermore, the reactions occur in vertical array tubes placed in a furnace and filled with the Ni-based catalyst (packed bed reactor). Regarding active phase for SRM systems, metallic nickel is one of the most used materials due to

economic reasons associated with high catalytic activity. These features make nickel an excellent choice for SRM which is usually supported on modified alumina.[102, 104] The reactant gas feed is generally constituted by natural gas and steam in excess (steam to carbon molar ratio between 2.5 and 5). The main goal of using excess steam is to avoid the carbon formation over the catalytic surface and, as consequence, avoid Ni deactivation, pore/tubes obstruction, and problems related to pressure drop increase in the reactor. Furthermore, the elevated temperature of conventional bed reformers is used to achieve the complete conversion of methane, which is limited by the thermodynamic equilibrium of the reversible reactions and, also to avoid the carbon deposition.[102]

The flowsheet of conventional SRM process is schematized in Figure 2.18. The first reforming step (eq. 2.10) consists of the reaction between methane and steam fed into the reformer furnace to produce hydrogen and carbon monoxide in an endothermic reaction.

$$CH_4 + H_2O \rightleftharpoons CO + 3H_2 \qquad \Delta H°_{298K} = 206 \text{ kJ/mol} \qquad \text{Eq. 2.10}$$

The reformer products are fed into the water gas shift reactor to produce more hydrogen and carbon dioxide (eq. 2.11). The reaction is exothermic and favored at low temperatures (300-400 °C).

$$CO + 2H_2O \rightleftharpoons CO_2 + H_2 \qquad \Delta H°_{298K} = -41 \text{ kJ/mol} \qquad \text{Eq. 2.11}$$

The typical gas composition on a dry basis in the effluent of shift reactor is 76 vol.% H_2, 3 vol.% CO, 17 vol.% CO_2, and 4 vol.% unreacted CH_4.[105] The outlet gas can pass for some systems such as a scrubbing-stripping system with amines solution or pressure swing adsorption systems with solid sorbents to obtain a high-purity H_2 and remove the CO_2 produced.

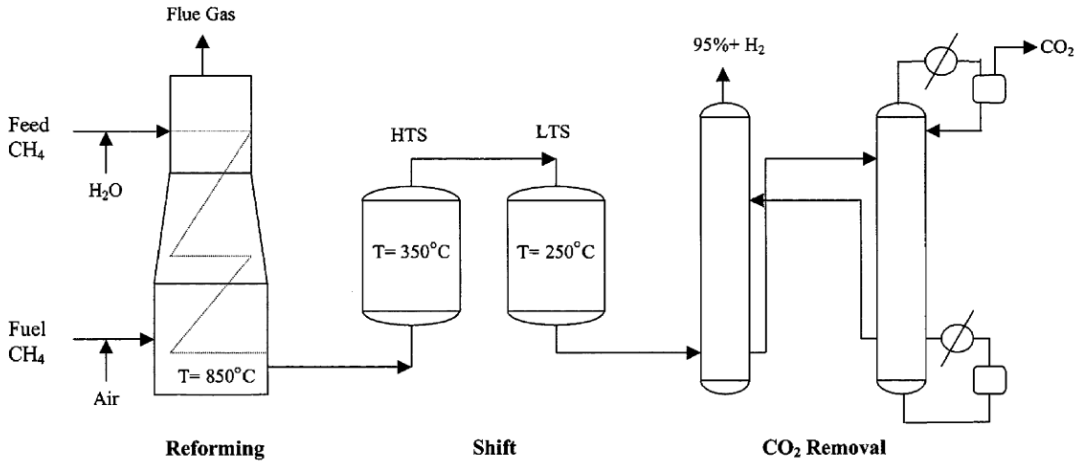

Figure 2.18: Flowsheet for a conventional steam reforming of methane process. (Reprinted from ref. [102]. Copyright 2008 with permission from Elsevier.)

2.3.2 Sorption-enhanced steam reforming process (SE-SRP)

As already mentioned, the steam reforming of methane has some drawbacks related to high energy consumption, for instance, the requirement for an additional step for hydrogen purification by chemical adsorption or PSA, which increases the capital investment and the process efficiency.[101] Moreover, the WGS system does not provide enough energy integration to contribute with the high endothermic nature of the reforming reaction and the PSA is characterized to be a relatively complex process with losses around 10 % of the H_2 fed. Accordingly, the cost of both stages is estimated to be around 30% of the total cost of H_2 production unit.[105] For these reasons, the sorption-enhanced steam reforming process was proposed as a novel efficient technology to improve the energetic efficiency and reactant conversion and/or hydrogen selectivity. The principle is based on the utilization of a mixture of a catalyst for hydrogen production and a selective regenerable solid sorbent for CO_2 separation in the reforming reactor. Then, the equilibrium of reversible reactions (eq. 2.10 and eq. 2.11) are shifted according to Le Chatelier's principle to enhance high-purity hydrogen production thought *in situ* CO_2 removal.[68, 103] The SE-SRM is a technology that can make possible to carry out the steam reforming of methane at lower temperatures (450-600 °C) as well as obtain H_2 concentration with 95 vol.% on dry basis in a single step (max. 80 vol.% on dry basis for conventional SRM) as shown by Figure 2.19.

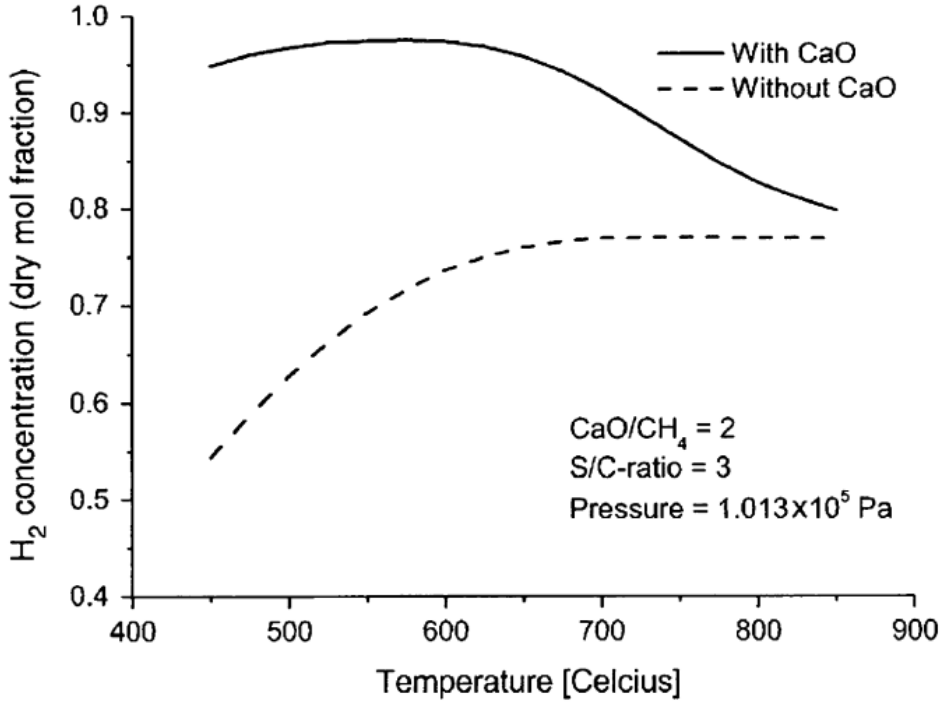

Figure 2.19: Hydrogen content at equilibrium as a function of temperature for pressure of $1.013x10^5$ Pa, H_2O:CH_4 molar ratio of 3 and CaO:CH_4 molar ratio of 2. (Reprinted from ref. [102]. Copyright 2008 with permission from Elsevier.)

The review published by Yancheshmeh et al.[68] listed the several advantages of SE-SRM which are also highlighted in the literature.[38, 105, 106]

- Highly efficient in H_2 production;
- Smaller emissions of by-products (CO_2 and CO) to atmosphere;
- Eliminating the individual reactor for water gas shift reaction;
- Saving energy of 20% to 25% compared to the conventional SRM;
- Achieving high methane conversion with a significant reduction of operation temperature (450-600 ºC) compared to traditional SRM process (750-900 ºC);
- Fewer problems related to carbon deposition in the reformer;
- Relatively pure CO_2 suitable for sequestration or use in different processes.

In addition to reactions of SRM and WGS, the non-catalytic highly exothermic carbonation reaction (eq. 2.12) occurs using a solid sorbent (MeO represents a metal oxide such as CaO):

$$MeO_{(s)} + CO_{2(g)} \rightleftharpoons MeCO_{3(g)} \qquad \Delta H° < 0 \qquad \text{Eq. 2.12}$$

So, the overall reactions for SE-SRM that occurs in a single reactor is given by (eq. 2.13):

$$CH_{4(g)} + 2H_2O_{(g)} + MeO_{(s)} \rightleftharpoons 4H_{2(g)} + MeCO_{3(s)} \quad \Delta H° \sim 0 \qquad \text{Eq. 2.13}$$

The feasibility of solid sorbent for SE-SRP is linked with features such as satisfactory CO_2 sorption capacity and rate, to be able to resist in severe cyclic conditions required for regeneration process and the carbonation temperature be compatible with reforming temperature.[68]

The process presents three distinct periods which are pre-breakthrough, breakthrough, and post-breakthrough as shown in Figure 2.20.

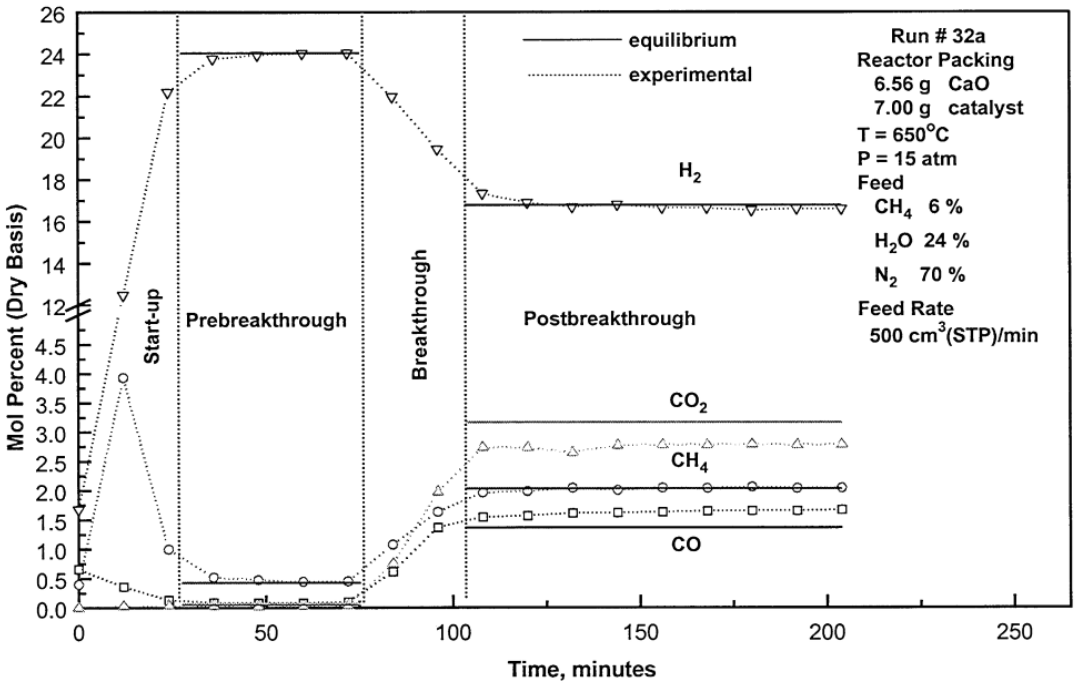

Figure 2.20: Typical reactor response curves. (Reprinted from ref. [102]. Copyright 2008 with permission from Elsevier.)

Following the unsteady state start-up period, the pre-breakthrough (first stage) occurs with maximum efficiency for all reactions (high-purity hydrogen production

attached with CO_2 removal by sorbent) and with molar fraction nears to the equilibrium one. After that, the efficiency begins to decline. This period is called by breakthrough where the sorbent capacity decreases and, consequently, lose their adsorption efficiency. In the last period, post-breakthrough, the sorbent is already fully saturated and only the reforming reaction occurs with the molar fraction equal to conventional SRM.

Several contributions made about SE-SRM using CaO-based sorbent investigated operational aspects including reactant flow, reforming and regeneration temperature, presence of inert, synthesis method, etc. In 1999, Balasubramanian et al.[107] studied the effects of temperature, methane concentration in the feed gas, steam-to-methane ratio, feed gas flow rate, and sorbent-to-catalyst ratio in a SE-SRM process. The material used for SE-SRM consists of a mixture of a commercial Ni/Al_2O_3 and CaO from calcined $CaCO_3$. The authors obtained H_2 molar fraction higher than 95% (dry basis) at 650 °C and steam/carbon ratio of 4. The thermodynamics analyses demonstrated that higher temperatures favored the CH_4 conversion, but decrease the CO_2 adsorption capacity and rate. On the other hand, the H_2 content was relatively independent of the temperature (bellow 750 °C), but at lower temperatures, the main impurity was the unconverted CH_4. Besides the aforementioned potential advantages about SE-SRM, the authors mentioned some unsolved problems include continuous separation of catalyst and sorbent and the stability/durability of the sorbent for multiple cycle operations under severe conditions.

Recently, Garcia-Lario et. al.[108] tested a physical mixture of CaO, NiO, and calcium cement aluminate for SE-SRM at 650 °C, S/C of 3, and 1200 h^{-1} CH_4 spatial velocity. The NiO content of the hybrid materials was 9, 14, and 18.5 wt.%. As a catalytic result, they reached pre-breakthrough H_2 composition higher than 94 vol.% (dry basis) and gas product composition very close to thermodynamic equilibrium. Under realistic conditions, the cyclic tests of 18.5 wt.% NiO sample exhibited a small increase of NiO crystal size whereby a slight decrease in the activity. Nevertheless, the H_2 concentration remained above 90 vol.% on dry basis.

Di Giuliano et al.[109] adopted a different approach from the previous studies which use physical mixing of sorbent and catalyst. First, they synthesized the CaO-$Ca_{12}Al_{14}O_{33}$ sorbent using wet mixing method to produce mayenite or CaO-mayenite with various fractions of free CaO. After that, they impregnated the nickel using the

wet impregnation obtaining Ni-mayenite (SRM catalyst) and Ni-CaO-mayenite (SE-SRM catalyst) with different Ni loading. SE-SRM tests in a packed-bed reactor showed that samples with free CaO fractions equal to or higher than 30 wt.% had a detrimental influence on catalytic activity. Furthermore, the materials impregnated only with 3 wt.% Ni exhibited the worst performance (X_{CH4} < 10% after 3h) while samples with 10 wt.% were fully active for SE-SRM (stable X_{CH4} > 95%). In addition, the multicycle TGA tests proved the positive effect of the presence of $Ca_{12}Al_{14}O_{33}$ on CaO stability during the CO_2 adsorption cycles.

Kim et al.[51] prepared one-body Ni-CaO-$Ca_{12}Al_{14}O_{33}$ (CaO:Inert 75:25) catalytic sorbents by a combination of preparation and hydration and investigated the influence of the aluminum addition in different preparation steps. The introduction of aluminum precursor in the first precipitation step induced the formation of the $Ca_{12}Al_{14}O_{33}$ that gives stability to CO_2 sorbent. The excellent result was justified by focused ion beam - transmission electron microscopy (FIB-TEM) analysis which confirms the formation of porous structures in sorbent providing a spacious pathway for the CO_2 diffusion. They also investigated different Ni loadings (3, 5, 7, and 10 wt.% of Ni) with the synthesized sorbent and compared them with a physical mixture of the sorbent and a commercial reforming catalyst. The fixed bed reactor was prepared with 12 g in case of synthesized material and 9 g of sorbent and 3 g for Ni catalyst in case of the physical mixture. The SE-SRM tests were carried out at 630 °C, CH_4 flow = 70 mL/min and water vapor = 210 mL/min. The regeneration step was performed at 780 °C under N_2 gas flow. They found that all Ni loads were active for SE-SRM with pre-breakthrough H_2 concentration around 95 vol.% (dry basis) during 70 min and showed good preservation of the pre-breakthrough period over the cycles. Moreover, the catalyst with 7 wt.% of Ni presented the best performance compared with all samples and, also, with the mixed catalyst.

Cesário et al.[110] used a microwave-assisted self-combustion to synthesize the Ni-CaO-mayenite and compared it with the wet mixing method. The final composition of the material was 5 wt.% Ni and 90% or 75% of free CaO on $Ca_{12}Al_{14}O_{33}$. The authors point out that the developed method was a promising way to produce catalyst/sorbent with high surface area and, consequently, increase the CO_2 capture capacity. Moreover, the sample prepared by this microwave method and with the lowest CaO content was the most active and stable in SE-SRM with pre-breakthrough H_2 concentration 100 vol.% on dry basis, methane conversion close to 100% for 15h

experiments. Additionally, they reported a deactivation towards CH_4 conversion for samples with higher free CaO.

Chanburanasiri et al.[111] studied the SE-SRM process using Ni/Al_2O_3, Ni/CaO, and Ni/MG30-K. The catalyst was prepared by incipient wetness with several Ni loadings (8 wt.%, 10 wt.%, and 12.5 wt.%), and the tests were carried out in a fixed bed reactor system. The authors found that the optimum operation parameters were at atmospheric pressure, steam to methane ratio of 3, T = 873 K. For the catalyst, 12.5 wt.% Ni/CaO was the appropriate ratio resulting in high hydrogen concentration (above 80 vol.%) during the pre-breakthrough period. Furthermore, the authors suggest that the high-purity hydrogen production provided by the multifunctional catalysts is a good reason to substitute the Al_2O_3 for CO_2 sorbent as support despite the fact that the alumina containing catalyst presented high activity.

Broda et al.[112] synthesized a bifunctional catalyst contained 45 wt.% of Ni reforming catalyst and 21 wt.% of Ca-based CO_2 sorbent dispersed in the hydrotalcite (HTlc) structure via co-precipitation method. The authors obtained a hybrid material with appropriate surface area (54 m^2/g) and high dispersion of Ni and Ca in the HTlc containing Mg and Al (Figure 2.21). These features resulted in high H_2 production (99 vol.% on dry basis) and in high CO_2 capacity and stability during carbonation/calcination cycles, which was very different compared to a mixture of limestone and Ni/SiO_2 or nickel HTlc-derived catalyst. In contrast, they affirmed that low CaO loading is a downside since a high amount of hybrid material is required to obtain an adequate CO_2 adsorption capacity.

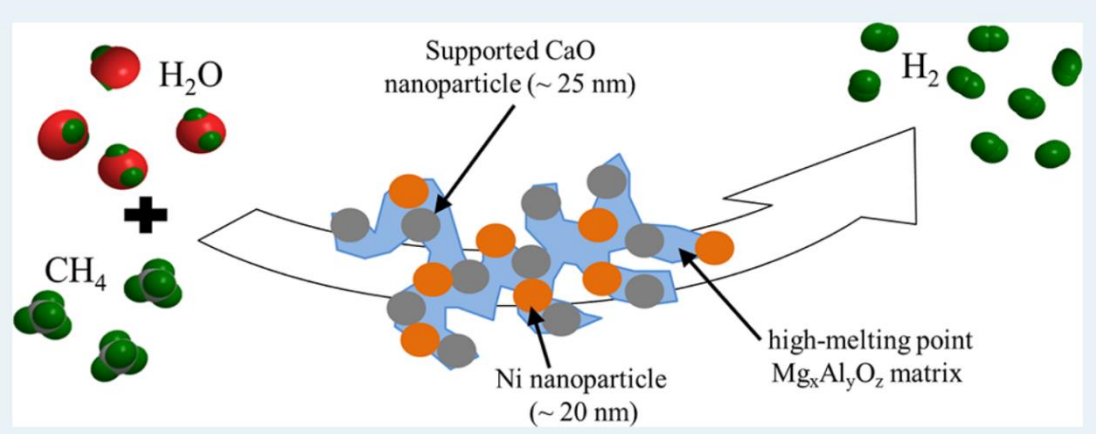

Figure 2.21: Schematic diagram of hybrid catalyst-CO_2 sorbent arrangement. (Reprinted with permission from ref. [112] Copyright 2012 American Chemical Society.)

In a further study, Broda et al.[113] also synthesized a Ni-hydrotalcite derived catalyst via a co-precipitation method and CaO-based sorbent support on aluminate calcium via a sol-gel technique. The SE-SRM conditions were T = 550 °C and S/C = 4 and the regeneration was at 750 °C under an inert atmosphere for 10 cycles. The amount of sample in the fixed bed reactor was 5.7 g of Ni-hydrotalcite and 1.26 g of $CaO/Ca_{12}Al_{14}O_{33}$. The authors demonstrate a relationship between the quantity of H_2 produced and the breakthrough characteristic. For example, the pre-breakthrough H_2 concentration was close to 99 vol.% on dry basis for the Ni-HTlc + Ca:Al 80:20 and the average decay rate of H_2 production with cycle number was 1.9% per cycle as determined from ten-cycle experiment, which was 275% lower than that of Ni-HTlc + limestone. The authors argue that these excellent results were attributed to the nanostructured morphology and the homogeneously dispersed high Tammann temperature support ($Ca_{12}Al_{14}O_{33}$), which provides resistance against the sintering of calcium oxide.

Radfarnia et al.[114] investigated the influence of operation parameters, including CH_4 flow and steam to carbon ratio, using Al-stabilized CaO-Ni hybrid material for 10 cycles of SE-SRM. According to the experimental results, the catalyst with NiO loadings of 25 wt.% exhibited the best performance with the CaO molar conversion of 41.2% at the end of 25th sorption cycle and the average CH_4 conversion and the pre-breakthrough H_2 concentration during 10 SE-SRM cycles of 99.1% and 96.1%, respectively. SE-SRM process efficiency was favored by higher S/C ratio but was disfavored by higher CH_4 flow rate, which decreases the H_2 yield and shortens the pre-breakthrough period. With an average H_2 yield of 97.3% during 30 cycles, the authors verified the stability in long-term operation and demonstrated that the proposed material is a promising hybrid sorbent-catalyst for application in hydrogen production by SE-SRM process. In another article[115], the same authors synthesized Ni/CaO-$CaZrO_3$ (13,18, and 20.5 wt.% NiO) sorbent-material by wet-mixing/sonification technique. With the same role as $Ca_{12}Al_{14}O_{33}$, the $CaZrO_3$ provides effective thermal stability under severe conditions in order to avoid deactivation of CaO sorbent by sintering. The material with the highest nickel loading (20.5 wt.% NiO) showed the highest H_2 production at the end of 10th cycle (91 vol.%).

Using zirconium as a stabilizer, Zhao et al.[116] developed a series of Ni/CaO-$CaZrO_3$ bifunctional catalysts with different Ni loading and CaO content via a citrate-

based sol-gel method. The CO_2 adsorption and SE-SRM experiments showed that the material with $CaZrO_3$ inert into the structure had higher stability in cyclic operation than Ni/CaO. Moreover, in terms of activity, stability, and duration of pre-breakthrough, the best material composition tested was Ni:CaO:$CaZrO_3$ equal to 15:60.3:24.7 due to the formation of small grains, narrow Ni particle size distribution, and uniform elemental distribution.

2.4 The use of CO_2

The CCUS is part of the technologies that are needed to mitigate climate change. It involves the capture of CO_2 for subsequent storage or recycled to be used. The use of CO_2 is considered as a complement, not an alternative, to the storage into a deep rock formation in order to achieve the climate goals.[117] Thus, the implementation of the CCUS is associated with the development of opportunities for the use of carbon dioxide. In this scenario, the availability and origin of the CO_2 are important aspects to evaluate the technical and economic feasibility of the processes that use the CO_2.

As can be seen in Figure 2.22, the CO_2 can come from fossil fuels processing, biomass, underground deposits, and directly from the air.[117] Furthermore, several applications could be derived from the use of CO_2, which can be directly used without a chemical alteration (non-conversion) or converted via multiple chemical and biological processes. As recently reported by the IEA[117], two of the important key commercial drivers for these applications are the conversion of hydrogen into a fuel that is as easy to handle and use as gaseous or liquid fossil fuels and the integration of carbon derived CO_2 into carbon-containing chemical products with lower CO_2 emissions than their fossil equivalents. One example of CO_2 emissions comes from the fertilizer industry, where around 130 Mt of CO_2 per year is generated from the steam reforming of natural gas to generate H_2 in ammonia production and, subsequently, used on-site in the urea synthesis.[99]

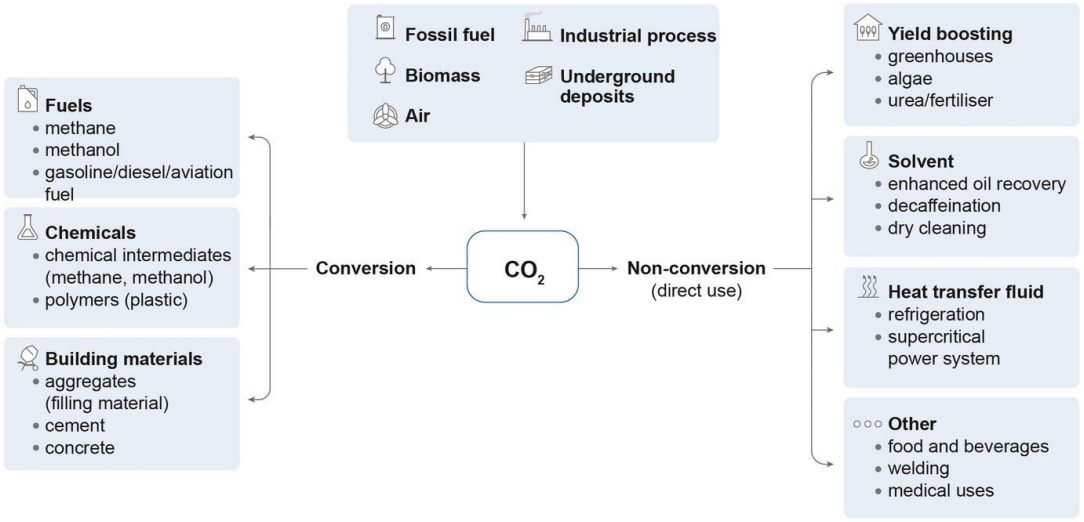

Figure 2.22: Short classification of the possible pathways for CO_2 use.[117] (Source: IEA (2019), Putting CO_2 to use, All rights reserved.)

Specifically, the chemical conversion involving the reaction of CO_2 and hydrogen has been received wide attraction, since results in a carbon-containing fuel that is easier to handle and use than pure hydrogen. The origin of the hydrogen could be from the SE-SRP or through the electrolysis of water. The combination of CO_2 and H_2 also is an alternative to fossil fuels in the production of value-added chemicals, including plastics, fibers, and synthetic rubber.[118, 119] From these chemicals, methanol has been highlighted since it is one of the top five chemical commodities commercialized in the world, and it can be converted into chemical intermediates such as olefins and aromatics.[118, 120] Its production can be from direct hydrogenation of CO_2 or via reverse water gas shift reaction, known as CAMERE, whereby the CO_2 is first converted to CO followed by methanol synthesis (Figure 2.23). Interestingly, the CAMERE process has 20% higher methanol yields than direct hydrogenation.[119, 121]

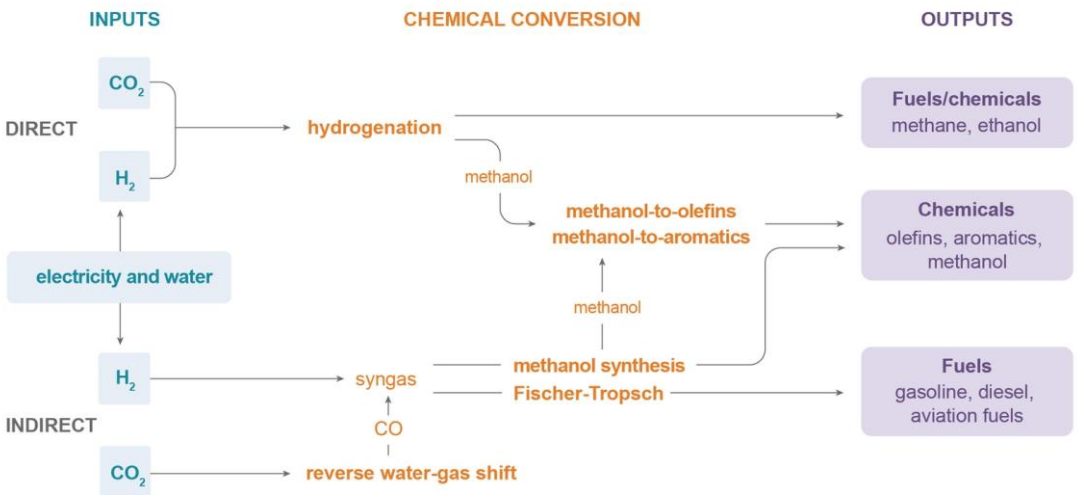

Figure 2.23: Mature conversion route for CO_2-derived fuels and chemicals intermediates.[117] (Source: IEA (2019), Putting CO_2 to use, All rights reserved.)

2.5 Reverse water gas shift reaction (rWGS)

The CAMERE process has the reverse water gas shift as the first step of the methanol production, as shown in Figure 2.24. In the first reaction, CO_2 and H_2 produce CO and H_2O at moderate temperature and pressure (eq. 2.14). This reaction has been widely explored because the produced CO is an important and versatile C1 building block that could be feedstock for chemicals and fuels. Moreover, the rWGS reaction has been received great interest due to the possibility of use in space exploration since the atmosphere on Mars has a high CO_2 concentration (~95%) and high availability of H_2 as a byproduct of oxygen generation.[119, 122]

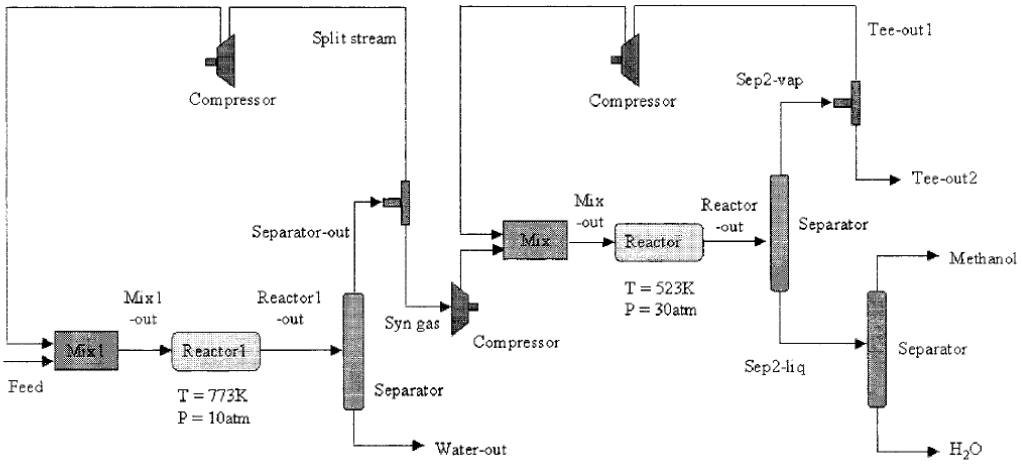

Figure 2.24: Scheme diagram of CAMERE process. (Reprinted with permission from ref. [121] Copyright 1999 American Chemical Society.)

The rWGS reaction could be considered a process in itself or as an intermediate reaction in another CO_2 hydrogenation process. For example, the main side reactions are the CO_2 and CO hydrogenation (eq. 2.15 and 2.16, respectively) whereby the production of methane and other oxygenated compounds like dimethyl ether, alcohols, and larger alkanes occurs via tandem reaction with the rWGS reaction as the first step. The presence of these side reactions affects the process selectivity, which becomes crucial importance for designing effective and selective catalysts for CO production.

Reverse water gas shift reaction (rWGS)

$CO_2 + H_2 \rightleftharpoons CO + H_2O$ $\Delta H^0 = 41.2$ kJ mol^{-1} Eq. 2.14

Sabatier reaction

$CO_2 + 4H_2 \rightleftharpoons CH_4 + 2H_2O$ $\Delta H^0 = -165$ kJ mol^{-1} Eq. 2.15

Methanation

$CO + 3H_2 \rightleftharpoons CH_4 + H_2O$ $\Delta H^0 = -206$ kJ mol^{-1} Eq. 2.16

The rWGS reaction is an endothermic process, and the reaction is thermodynamically favored at high temperatures. Kaiser et al.[123] analyzed the equilibrium composition for a molar H_2/CO_2 inlet ratio equal to 3 and temperature range from 100 °C to 1000 °C. The results as shown in Figure 2.25 revealed that the methanation is favored at low temperatures (<600 °C) while methane is almost not

formed above 700 °C, remaining only CO as the main product. Nonetheless, the low temperature is desirable to decrease the operational costs and energy losses.[123] Consequently, methane production will decrease the efficiency of CO production and the feasibility of the use. A deep understanding of the chain mechanism of the rWGS reaction and the reaction kinetics is essential to develop catalysts that are highly active and selective to CO.

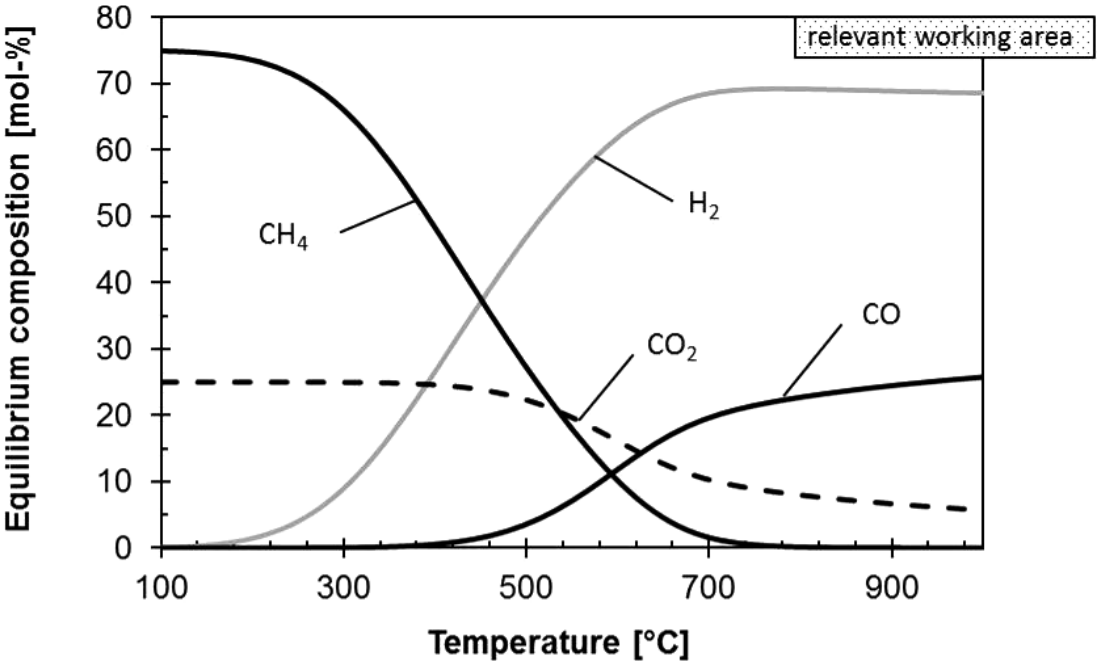

Figure 2.25: Thermodynamic equilibrium composition of the product gas of rWGS reaction at 1 bar and H_2/CO_2 molar ratio of 3. (Reproduced with permission from ref. [123] Copyright 2013 Wiley.)

2.5.1 Mechanism of rWGS reaction

The investigations about the rWGS reaction mechanism have been constructed by monitoring the absorbed species on the catalyst surface using *in situ* techniques, reaction kinetics, spectroscopy, isotopic tracer methods, and DFT calculations (Figure 2.26).[124-128] There are two main reaction mechanisms proposed for the rWGS reaction in the literature: redox mechanism and associative mechanism.[122, 129]

The redox mechanism consists of the reduction of the CO_2 molecule to CO with the catalyst being directly oxidized, and subsequent H_2 reduction of the catalyst to complete the catalytic turnover. This mechanism was originally proposed for Cu-

based catalyst. Ginés et al.[124] investigated the reaction kinetics with controlled experiments under different H_2/CO_2 ratios using commercial $Cu/ZnO/Al_2O_3$ catalyst. The results followed the redox mechanism where the CO_2 oxidizes the active Cu sites to Cu^+ and forms CO, while H_2 reduces the generated Cu^+ to Cu^0 and releases H_2O.

The associative mechanism is based on the formation of intermediates. CO_2 adsorbs on the surface and reacts with the dissociated H to form an intermediate that can be formate (*HCOO), carboxyl (*COOH), carbonate (CO_3^{2-}), and bicarbonate (HCO_3^-). Afterward, these intermediates are decomposed to CO and H_2O.[122, 127] This type of mechanism was originally evidenced on catalysts that contain a metal/reducible support.[127, 130, 131] For instance, Goguet et al.[127] performed a combination of mass spectrometry (MS) and diffuse reflectance infrared Fourier transform spectroscopy (DRIFT) analysis during steady-state isotopic transient kinetic analysis (SSITKA) to investigate the surface species formed on the Pt/CeO_2 catalyst. In summary, the authors evidenced the formation of carbonate, carbonyl, and formate species which were consumed by half in 54 ±5 s, 48 ±5 s, and 660 ±30 s, respectively. Moreover, they concluded that surface carbonates are the main surface intermediate in the formation of CO in the gas phase. Thereby, the key intermediate of the associative mechanism can vary depending on the catalytic system as well as under different reaction conditions. These variables turn the determination of the main intermediate or even the dominant mechanism very difficult, which makes both mechanisms still debatable.

Associated with the mechanism of the rWGS reaction, the design of the catalyst for this reaction is crucial to mitigate side reactions. An active catalyst needs to be able to (i) adsorb CO_2 and disrupt one C-O bond of CO_2 and (ii) dissociate H_2 and hydrogenate the oxygen to form H_2O. Moreover, the high selective rWGS catalyst requires a balance between C-O dissociation and hydrogenation ability to avoid the formation of CH_4 and methanol and, consequently, the decrease in the CO selectivity.[129, 132]

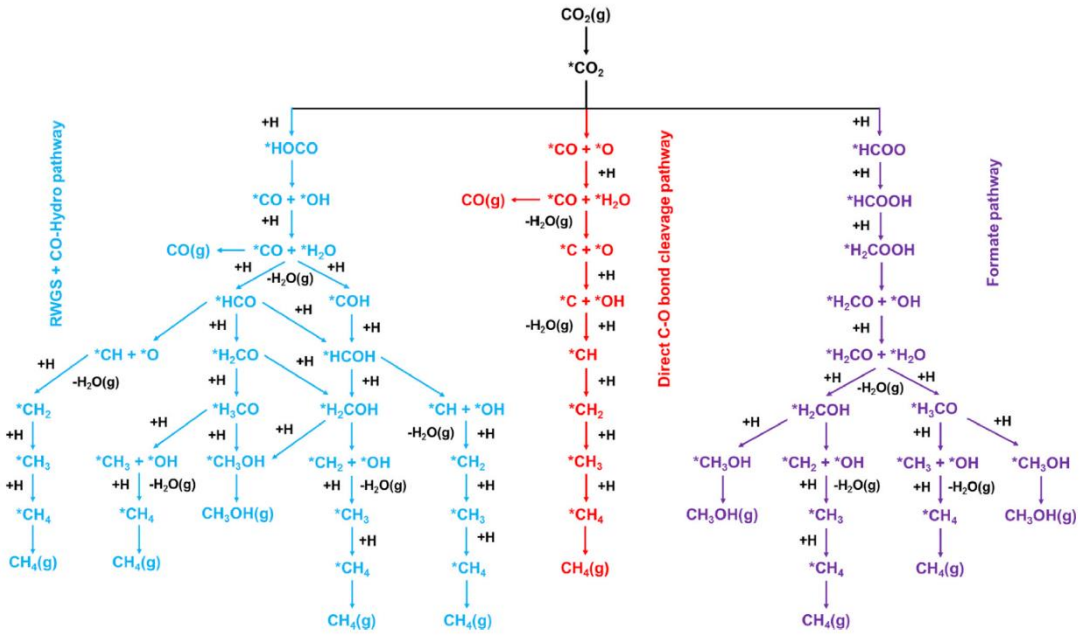

Figure 2.26: Representative scheme of the possible reaction pathways of the conversion of CO_2 to CO, CH_3OH, and CH_4 where *X indicates adsorbed species. (Reprinted (adapted) with permission from ref. [133] Copyright 2017 American Chemical Society.)

2.5.2 Catalysts for rWGS reaction

In general, several features of the metal and support determine how good a catalyst is for a specific reaction. For instance, for the metal, characteristics such as the particle size and dispersion, loading, corrosion and oxidation resistance, thermal stability and, for the support, its reducibility, thermal and mechanical stability, and its interaction with the metal as well as the nature of the active species formed at the interfacial sites.[132] The most common rWGS catalysts are the supported precious metals such as Au[134,135], Pt[136], Rh[137], and Pd[138] and supported non-precious metals such as Cu[125, 139-143], Fe[144], and Ni[145, 146]. Furthermore, a variety of supports including SiO_2[147], Al_2O_3[148, 149], TiO_2[150, 151], ZrO_2[151-153], CeO_2[150], ZnO[154], and In_2O_3[155] has been used to disperse these metals. Despite having good activity and being selective for rWGS reaction, the noble metals have high costs and low stability capacity, which makes them economically unviable for a large-scale process. In this scenario, copper and nickel appear as promising candidates to substitute the precious metals due to their low cost, excellent catalytic hydrogenation activity, and high availability.

Specifically, Cu-based catalyst has been widely studied for rWGS reaction due to performing at low temperature and low selectivity for methane. It has been found that the catalytic activity is comparable to the noble metals at low temperature, and it is highly sensitive to the metal dispersion/particle size and surface morphology.[139, 156, 157] However, Cu-based catalysts have some disadvantages such as the necessity of a high H_2/CO_2 feed ratio to achieve significant CO_2 conversions, sintering of the particles, and poor thermal stability at high temperature.[119, 132] During the reaction, the metallic Cu tends to oxidize by CO_2 forming Cu^{2+} species, which results in Cu agglomerates.[158] This sintering process leads to a loss of surface area, decreasing the activity of the rWGS reaction.

For Ni-based catalysts, the main drawback is the relatively low CO selectivity because of the high methanation activity. Several strategies have been tested to avoid the problems of both Ni- and Cu-based catalysts in order to improve the activity, CO selectivity, and stability of the active phase during the rWGS reaction. They are promoting with alkali metals, varying the support, tuning the metal-support interaction, controlling the particle size, and alloying the metal with other metals (e.g. Ga, In, Fe).[120, 129, 132]

2.6 Intermetallic compounds

The use of bimetallic catalyst, resulting from the interaction of two metallic elements, has been shown an effective strategy to increase the activity/selectivity in various reactions. The improvement is due to the synthesis of the new material with different chemical properties compared to the parent metals.[159-161] During the synthesis process, the resulting crystal structure could be a disordered alloy or ordered alloy. In the disordered alloy, also known as a solid solution, the atoms are randomly occupying the crystallographic sites of the crystal structure of one of the metals. On the other hand, the ordered alloy or better known as intermetallic compounds has a complex crystal structure which leads to a unique combination of electronic and geometric structure that is a result of a ligand effect and a specific atom disposition, respectively.[159, 160, 162]

For an intermetallic compound consisting of two elements, M and N, the formation of the ordered structure is a result of a redistribution of three classes of bond, M-M, M-N, and N-N of the disordered alloy structure. Depending on the composition

of the compound, these three types of bonds are balanced to minimize the Gibbs free energy, forming a stable phase (eq. 2.17).[163, 164] One strategy to overcome the barriers associated with atomic diffusion is the increase of the temperature, which know as annealing step.[164] Moreover, the correct temperature window is required to obtain the intermetallic phase, otherwise, only the disordered alloy is formed.

$$\Delta G_{mix} = \Delta H_{mix} - T\Delta S_{mix} \qquad \text{Eq. 2.17}$$

Recently, Armbrüster[159] showed the number of publications approaching the application of intermetallic compounds and catalysis has been increasing with time, as can be seen in Figure 2.27.

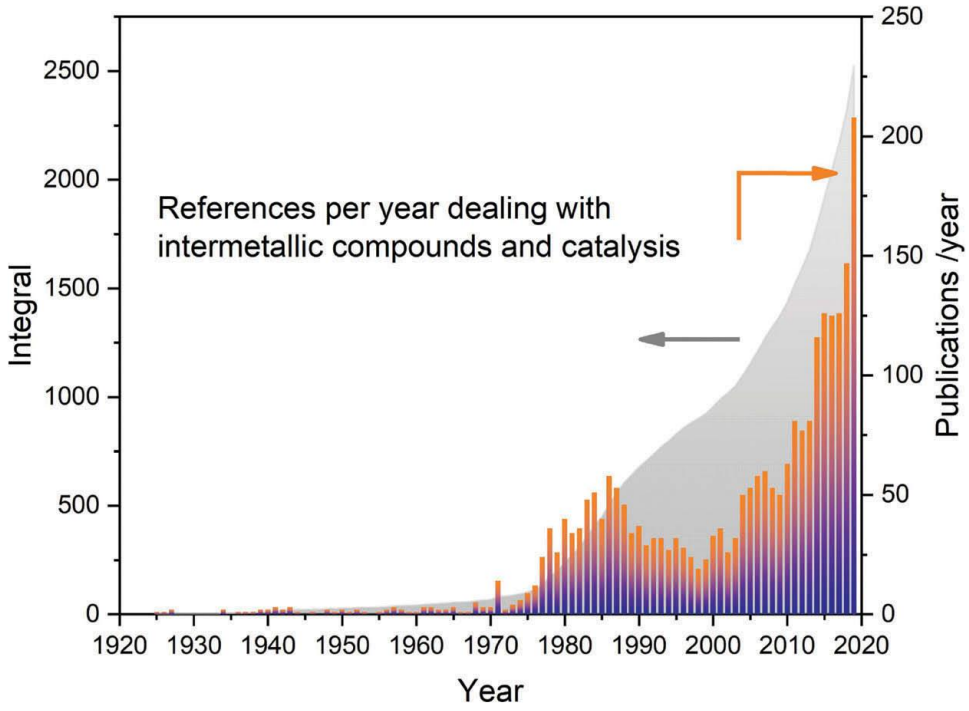

Figure 2.27: Number of relevant scientific publications per year involving the intermetallic compounds and the investigation of the catalytic properties.[159]

The recent surge of interest is due to the improvement in the catalytic performance of the metals provided by the alteration of the local coordination environment and the electronic structure, which influence the adsorption behaviors of reactants or intermediates.[161] For instance, Studt et al.[165] discovered the potential of the intermetallic Ni-Ga catalyst prepared by incipient wetness impregnation for methanol synthesis. The authors compared the Ni-Ga catalyst with the commercial $Cu/ZnO/Al_2O_3$ highlighting the effects caused in activity and selectivity for rWGS

reaction and methanol synthesis. According to them, the high activity presented by the Ni-Ga catalyst is related to the number of active sites where the intermetallic compound does not need a promoter while in the Cu-Zn catalyst, the copper particles will be active at few places where they are promoted by zinc. Moreover, the gallium-rich sites promote the methanol synthesis and the nickel-rich sites do the rWGS/methanation which, after a while, become self-poisoned by CO and carbon. On the other hand, both processes occur in the same surface site in Cu-Zn catalyst where a higher rWGS reaction is observed because the strength of the CO binding is not enough to poison the copper active sites. Therefore, they found that Ni_5Ga_3 is the best candidate due to the high activity and selectivity to methanol synthesis.

Interestingly, a study published by Kovnir et al.[166] revealed the excellent performance of intermetallic Pd-Ga catalyst for the semi hydrogenation of acetylene to ethylene. The authors attributed the high selectivity and long-term stability of the Pd-Ga catalyst to the presence of only isolated and stable sites on the surface (Figure 2.28).

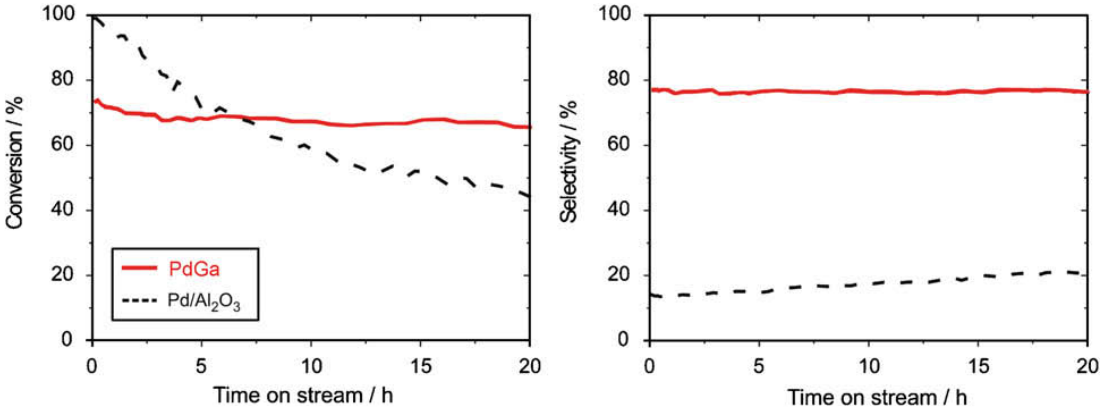

Figure 2.28: Acetylene conversion and selectivity to ethylene of PdGa and Pd/Al_2O_3 catalysts for the hydrogenation of acetylene. (Reprinted with permission from ref. [166] © 2007 Elsevier Science Ltd.)

Employing quantum chemical calculations and XPS measurements, the authors found that a significant difference between the electronic structure of the intermetallic compound and Pd metal, which matches with the covalent bonding found by the electron localizability indicator (ELI). Fourier transform infrared spectroscopy measurements also showed the electronic and geometric effect by analyzing the CO adsorption band position. They observed a shift of the CO band adsorption to lower

wavenumbers compared to the metallic Pd catalyst and the absence of the bands related to bridging CO in the region 1900-2000 cm^{-1}, which indicates that the active sites of PdGa are structurally isolated.

Feng et al.[167] also studied the semi hydrogenation of acetylene using the intermetallic Pd-In catalyst. They used the density functional theory (DFT) to predict selectivity for ethylene on the PdIn(110) and Pd_3In(111) surfaces. The results showed higher selectivity for semi hydrogenation of alkynes on the PdIn (110) surface compared to Pd_3In(111) surface. The PdIn surface exhibits complete isolation of Pd atoms via In atom, whereas the Pd_3In surface has Pd trimer sites that decrease the selective towards this reaction. As shown in Figure 2.29, the authors validated this idea by experimental results. The PdIn nanocrystals showed much higher selective for acetylene hydrogenation (92%) than Pd_3In nanocrystals (21%) at 90 °C.

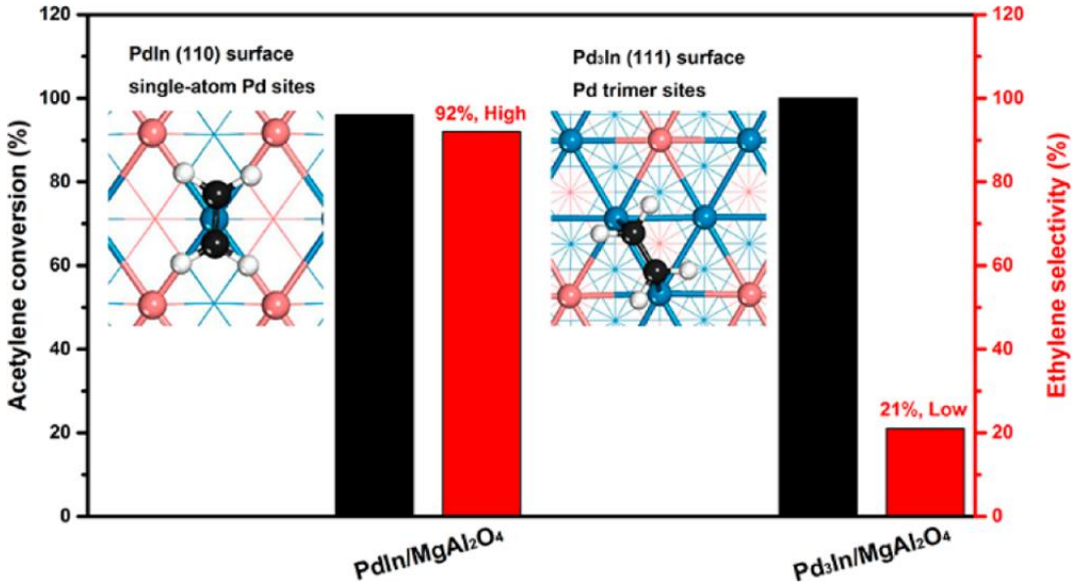

Figure 2.29: Adsorption configuration of acetylene on PdIn (110) surface and Pd_3In (111) surface and the catalytic activity and selectivity for semi hydrogenation of acetylene. (Reprinted with permission from ref. [167] Copyright 2017 American Chemical Society.)

Porossoff and Chen[168] investigated the CO_2 reduction using Pt-Ni, Pt-Co, and Pd-Ni intermetallic compounds supported on two different oxides: CeO_2 and Al_2O_3. The reaction was performed in an FTIR spectrometer at 300 °C, 0.04 bar, and H_2/CO_2 feed ratio equal to 3. Regarding the effect of the support, the reducible CeO_2 showed higher catalytic activity than the non-reducible Al_2O_3, which was justified by the

oxygen storage capacity and the interaction of it with the bimetallic bonds. Furthermore, the authors evaluated the effects of the alloying of two different metals on the CO/CH_4 ratio, correlating with the calculation of d-band center. Among the monometallic and bimetallic catalysts studied, $PdNi/CeO_2$ showed the highest activity but formed a high amount of CH_4, while the most selective to CO was the $PtCo/\gamma$-Al_2O_3. In summary, the selectivity trend followed the electronic properties of the supported catalyst, which were estimated using the values of surface d-band center.

Also investigating the reduction of the CO_2 to CO, Liu et al.[169] investigated the impact of the silica support and the chemical and electronic interaction of Pt-Ni bimetallic catalyst on the activity and selectivity to CO. The reaction conditions were at 400 °C, 1 bar, H_2:CO_2:Ar = 2:1:5 in a total flow of 40 mL/min. Using *in situ* XAS and DRIFTS, the authors revealed that (i) there are complex reactions that occur between the metals and support under *operando* conditions and (ii) there is a strong metal-silica bonding interaction. These prevent the formation of alloy phases containing Ni-Ni bonds, which provide only heterometallic Pt-Ni interactions on the surface of the catalyst. According to the authors, this specific atomic arrangement is responsible for the high activities and selectivity towards CO in the bimetallic catalyst for the rWGS reaction.

2.6.1 Intermetallic Ni-In compound and its application

In substitution of Ga and noble metals, indium has also been employed as a second metal to alloy Ni, forming a range of disordered alloys and intermetallic compounds as can be seen in Figure 2.30.[170]

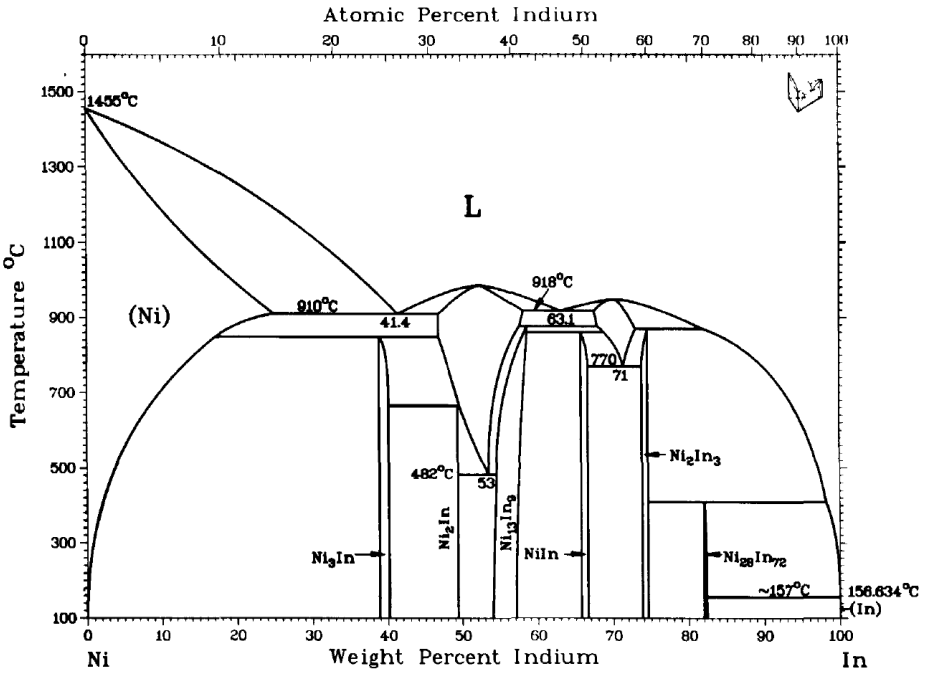

Figure 2.30: Diagram phase of the binary Ni-In system. (Reprinted from ref. [170] Copyright 1997 with permission from Elsevier.)

Ni-In catalyst was also studied for selective hydrogenation of acetylene as well as Pd-Ga and Pd-In catalysts. Chen et al.[171] investigated the effect of In on the performance of Ni-based catalysts and the relationship between the structure and performance of the intermetallic compounds for selective hydrogenation of acetylene. The materials were supported on SiO_2 to reduce the support effect due to its inert character. According to the obtained results, two influences of indium were observed. First, In atoms geometrically isolate the active Ni sites which inhibit the formation of strongly adsorbed multi-σ-bonded hydrocarbon species. Second, XPS measurements revealed a charge transfer from In to Ni atoms weakening the adsorption of acetylene and ethylene which restrain the C-C hydrogenolysis and the polymerization of acetylene and the intermediate compounds. However, the authors highlighted that there is an optimal Ni:In composition to improve the selectivity. The formation of C4+ hydrocarbons tends to increase because of the enhanced catalyst acidity. The charger transfer makes the In atoms act as Lewis acid sites, promoting the polymerization reaction.

The same kind of electronic interaction between In and Ni atoms was observed by Wang et al.[172]. They synthesized Ni_2In, NiIn, and Ni_2In_3 supported on SiO_2 via sol-gel method and tested for selective hydrogenation of fatty acid methyl esters. The

intermetallic Ni-In catalyst showed a remarkable suppression of the decarbonylation/decarboxylation and C-C bond hydrogenolysis, resulting in a higher selectivity to fatty alcohols when compared to metallic Ni. According to the XPS data, there is a strong interaction between Ni and In atoms that provide the charge transfer from In to Ni. The authors affirm that the positively charged In species may act as Lewis acid sites to adsorb oxygen in ester and so to activate the C=O/C−O bond, favoring the selective hydrogenation. Thereby, this synergetic effect between Ni and In facilitates the selective hydrogenation to yield fatty alcohols, which reached above 94%. Another example of the application of intermetallic Ni-In catalyst is the hydrodeoxygenation of anisole. Wang et al.[173] obtained high selectivities for benzene, toluene, xylene, and cyclohexane using Ni-In catalysts, although the conversions of anisole were lower than the monometallic catalyst. These excellent selectivities were attributed to the suppression of benzene ring hydrogenation and C-C bond hydrogenolysis caused by the geometric and electronic effect present in the bimetallic catalyst.

Li et al.[174] synthesized a highly dispersed bimetallic Ni-In catalyst with different compositions via coprecipitation method. For that, the layered double hydroxides were used as precursors. The resulting intermetallic phases were Ni_3In, Ni_2In, NiIn, and Ni_2In_3 being confirmed by the XRD results. The catalysts were tested in the selective hydrogenation of various unsaturated aldehydes including furfural, 1-phenyltanol, crotonaldehyde, and 2-hexenal. The excellent conversions and selectivity to desirable products were justified by the modulation of the chemical composition and the particle size of the intermetallic Ni-In catalyst. In this study, the authors also evidenced the electronic and geometric effect in this Ni-In system using the XAS characterization and DFT calculations. In summary, both effects contributed to the nucleophilic addition process of C=C group instead of the electrophilic addition of C=C, which greatly enhanced hydrogenation selectivity showed by bimetallic Ni-In catalyst as can be seen schematically in Figure 2.31.

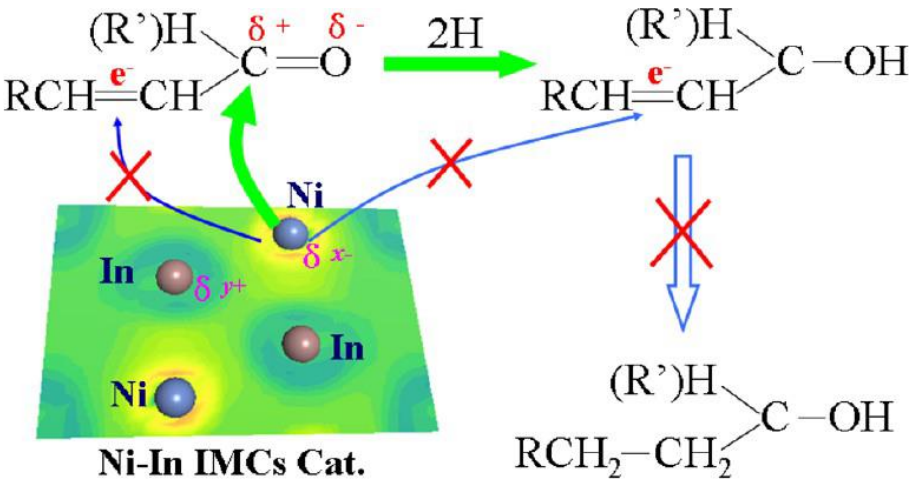

Figure 2.31: Schematic illustration representing the reaction path for the selective hydrogenation of unsaturated carbonyl compounds over the Ni-In catalysts. (Reprinted with permission from ref. [174] Copyright 2013 American Chemical Society.)

Besides enhancing activities and selectivities, the addition of a second metal to form intermetallic compounds could also be used to provide stability to a specific catalyst. Károlyi et al.[175] reported that a Ni-In catalyst was employed to decrease the coke formation in the dry reforming of methane. The bimetallic catalysts prepared by deposition-precipitation method exhibited high stability by preventing the formation of multi-bonded carbon species. The CO pulse chemisorption experiments showed that the adsorption of CO on Ni/SiO_2 is stronger than on $Ni\text{-}In/SiO_2$ indicating that the Boudouard reaction is less favored on the bimetallic catalyst.

Therefore, the literature review of the intermetallic compounds illustrated the promising future of these materials and the wide range of application possibilities as catalysts. Particularly, the special properties of intermetallic compounds can be valuable to optimize catalytic processes of CO_2 valorization in order to produce value-added chemicals and fuels.

2.7 References

1. RIN21 *Renewables global status report*; 2019.
2. IEA *Global energy & CO_2 status*; 2019.
3. IEA *Global Energy Review*; Paris, 2021.
4. IPCC *Climate Change 2014: Synthesis Report. Contribution of Working Groups I, II and III to the Fifth Assessment Report of the Intergovernmental Panel on Climate Change*; Geneva, Switzerland, 2014; p 151.
5. IEA *Energy Technology Perspectives* 2016.
6. IEA *Energy Technology Perspectives*; Paris, 2020.

7. Instituite, G. C. *GCC-Global status of CCS*; 2019.
8. Kim, S. M.; Development of effective sorbents and catalysts for the capture and conversion of CO_2. ETH Zürich, 2019. https://doi.org/10.3929/ethz-b-000375084
9. Aaron, D.; Tsouris, C., Separation of CO_2 from flue gas: a review. *Separation Science and Technology* **2011,** *40* (1-3), 321-348. https://doi.org/10.1081/ss-200042244
10. Sridhar, S.; Smitha, B.; Aminabhavi, T. M., Separation of carbon dioxide from natural gas mixtures through polymeric membranes—a review. *Separation & Purification Reviews* **2007,** *36* (2), 113-174. https://doi.org/10.1080/15422110601165967
11. Danckwerts, P., The reaction of CO_2 with ethanolamines. *Chemical Engineering Science* **1979,** *34* (4), 443-446. https://doi.org/10.1016/0009-2509(79)85087-3
12. Fennell, P., Economics of chemical and calcium looping. In *Calcium and Chemical Looping Technology for Power Generation and Carbon Dioxide (CO_2) Capture*, 2015; pp 39-48.
13. MacKenzie, A.; Granatstein, D.; Anthony, E. J.; Abanades, J., Economics of CO_2 capture using the calcium cycle with a pressurized fluidized bed combustor. *Energy & fuels* **2007,** *21* (2), 920-926. https://doi.org/10.1021/ef0603378
14. Choi, S.; Drese, J. H.; Jones, C. W., Adsorbent materials for carbon dioxide capture from large anthropogenic point sources. *ChemSusChem* **2009,** *2* (9), 796-854. https://doi.org/10.1002/cssc.200900036
15. Kumar, S., The effect of elevated pressure, temperature and particles morphology on the carbon dioxide capture using zinc oxide. *Journal of CO_2 Utilization* **2014,** *8*, 60-66. https://doi.org/10.1016/j.jcou.2014.07.002
16. Kumar, S.; Saxena, S. K., A comparative study of CO_2 sorption properties for different oxides. *Materials for Renewable and Sustainable Energy* **2014,** *3* (3). https://doi.org/10.1007/s40243-014-0030-9
17. Yong, Z.; Mata, V.; Rodrigues, A. r. E., Adsorption of carbon dioxide at high temperature—a review. *Separation and purification technology* **2002,** *26* (2-3), 195-205. https://doi.org/10.1016/S1383-5866(01)00165-4
18. Alvarez, D.; Abanades, J. C., Determination of the critical product layer thickness in the reaction of CaO with CO_2. *Industrial & engineering chemistry research* **2005,** *44* (15), 5608-5615. https://doi.org/10.1021/ie050305s
19. Barker, R., The reversibility of the reaction $CaCO_3 \rightleftarrows CaO + CO_2$. *Journal of applied Chemistry and biotechnology* **1973,** *23* (10), 733-742. https://doi.org/10.1002/jctb.5020231005
20. Barin, I.; Platzki, G., *Thermochemical data of pure substances*. Wiley Online Library: 1995; Vol. 304.
21. Naeem, M. A.; Armutlulu, A.; Imtiaz, Q.; Donat, F.; Schaublin, R.; Kierzkowska, A.; Muller, C. R., Optimization of the structural characteristics of CaO and its effective stabilization yield high-capacity CO_2 sorbents. *Nat Commun* **2018,** *9* (1), 2408. https://doi.org/10.1038/s41467-018-04794-5
22. Broda, M. Synthetic calcium-based sorbents for pre-and post-combustion CO_2 capture. ETH Zürich, 2014. https://doi.org/10.3929/ethz-a-010252508
23. Li, Y.; Zhao, C.; Chen, H.; Liang, C.; Duan, L.; Zhou, W., Modified CaO-based sorbent looping cycle for CO_2 mitigation. *Fuel* **2009,** *88* (4), 697-704. https://doi.org/10.1016/j.fuel.2008.09.018
24. Radfarnia, H. R.; Iliuta, M. C., Limestone Acidification Using Citric Acid Coupled with Two-Step Calcination for Improving the CO_2 Sorbent Activity. *Industrial & Engineering Chemistry Research* **2013,** *52* (21), 7002-7013. https://doi.org/10.1021/ie400277q
25. Li, Y. J.; Zhao, C. S.; Qu, C. R.; Duan, L. B.; Li, Q. Z.; Liang, C., CO_2 Capture Using CaO Modified with Ethanol/Water Solution during Cyclic Calcination/Carbonation. *Chemical Engineering & Technology* **2008,** *31* (2), 237-244. https://doi.org/10.1002/ceat.200700371
26. Sun, R.; Li, Y.; Wu, S.; Liu, C.; Liu, H.; Lu, C., Enhancement of CO_2 capture capacity by modifying limestone with propionic acid. *Powder Technology* **2013,** *233*, 8-14. https://doi.org/10.1016/j.powtec.2012.08.011

27. Li, Y.; Sun, R.; Liu, H.; Lu, C., Cyclic CO_2 Capture Behavior of Limestone Modified with Pyroligneous Acid (PA) during Calcium Looping Cycles. *Industrial & Engineering Chemistry Research* **2011,** *50* (17), 10222-10228. https://doi.org/10.1021/ie2007455
28. Wang, S.; Shen, H.; Fan, S.; Zhao, Y.; Ma, X.; Gong, J., Enhanced CO_2 adsorption capacity and stability using CaO-based adsorbents treated by hydration. *AIChE Journal* **2013,** *59* (10), 3586-3593. https://doi.org/10.1002/aic.14126
29. Chen, H.; Zhao, C.; Yang, Y., Enhancement of attrition resistance and cyclic CO_2 capture of calcium-based sorbent pellets. *Fuel Processing Technology* **2013,** *116*, 116-122. https://doi.org/10.1016/j.fuproc.2013.05.012
30. Coppola, A.; Salatino, P.; Montagnaro, F.; Scala, F., Reactivation by water hydration of the CO_2 capture capacity of a calcium looping sorbent. *Fuel* **2014,** *127*, 109-115. https://doi.org/10.1016/j.fuel.2013.09.059
31. Li, C.-C.; Cheng, J.-Y.; Liu, W.-H.; Huang, C.-M.; Hsu, H.-W.; Lin, H.-P., Enhancement in cyclic stability of the CO_2 adsorption capacity of CaO-based sorbents by hydration for the calcium looping cycle. *Journal of the Taiwan Institute of Chemical Engineers* **2014,** *45* (1), 227-232. https://doi.org/10.1016/j.jtice.2013.06.019
32. Ridha, F. N.; Manovic, V.; Wu, Y.; Macchi, A.; Anthony, E. J., Pelletized CaO-based sorbents treated with organic acids for enhanced CO_2 capture in Ca-looping cycles. *International Journal of Greenhouse Gas Control* **2013,** *17*, 357-365. https://doi.org/10.1016/j.ijggc.2013.05.009
33. Ridha, F. N.; Manovic, V.; Macchi, A.; Anthony, M. A.; Anthony, E. J., Assessment of limestone treatment with organic acids for CO_2 capture in Ca-looping cycles. *Fuel Processing Technology* **2013,** *116*, 284-291. https://doi.org/10.1016/j.fuproc.2013.07.007
34. Lu, H.; Reddy, E. P.; Smirniotis, P. G., Calcium oxide based sorbents for capture of carbon dioxide at high temperatures. *Industrial & engineering chemistry research* **2006,** *45* (11), 3944-3949. https://doi.org/10.1021/ie051325x
35. Martavaltzi, C. S.; Lemonidou, A. A., Development of new CaO based sorbent materials for CO_2 removal at high temperature. *Microporous and Mesoporous Materials* **2008,** *110* (1), 119-127. https://doi.org/10.1016/j.micromeso.2007.10.006
36. Liu, W.; Low, N. W.; Feng, B.; Wang, G.; Diniz da Costa, J. C., Calcium precursors for the production of CaO sorbents for multicycle CO_2 capture. *Environmental science & technology* **2010,** *44* (2), 841-847. https://doi.org/10.1021/es902426n
37. Zhou, Z.; Qi, Y.; Xie, M.; Cheng, Z.; Yuan, W., Synthesis of CaO-based sorbents through incorporation of alumina/aluminate and their CO_2 capture performance. *Chemical Engineering Science* **2012,** *74*, 172-180. https://doi.org/10.1016/j.ces.2012.02.042
38. Pacciani, R.; Müller, C. R.; Davidson, J. F.; Dennis, J. S.; Hayhurst, A. N., Synthetic Ca-based solid sorbents suitable for capturing CO_2 in a fluidized bed. *The Canadian Journal of Chemical Engineering* **2008,** *86* (3), 356-366. https://doi.org/10.1002/cjce.20060
39. Zhang, M.; Peng, Y.; Sun, Y.; Li, P.; Yu, J., Preparation of $CaO–Al_2O_3$ sorbent and CO_2 capture performance at high temperature. *Fuel* **2013,** *111*, 636-642. https://doi.org/10.1016/j.fuel.2013.03.078
40. Broda, M.; Muller, C. R., Synthesis of highly efficient, Ca-based, Al_2O_3-stabilized, carbon gel-templated CO_2 sorbents. *Adv Mater* **2012,** *24* (22), 3059-64. https://doi.org/10.1002/adma.201104787
41. Angeli, S. D.; Martavaltzi, C. S.; Lemonidou, A. A., Development of a novel-synthesized Ca-based CO_2 sorbent for multicycle operation: parametric study of sorption. *Fuel* **2014,** *127*, 62-69. https://doi.org/10.1016/j.fuel.2013.10.046
42. Radfarnia, H. R.; Sayari, A., A highly efficient CaO-based CO_2 sorbent prepared by a citrate-assisted sol–gel technique. *Chemical Engineering Journal* **2015,** *262*, 913-920. https://doi.org/10.1016/j.cej.2014.09.074
43. Koirala, R.; Reddy, G. K.; Smirniotis, P. G., Single nozzle flame-made highly durable metal doped Ca-based sorbents for CO_2 capture at high temperature. *Energy & Fuels* **2012,** *26* (5), 3103-3109. https://doi.org/10.1021/ef3004015

44. Florin, N. H.; Blamey, J.; Fennell, P. S., Synthetic CaO-Based Sorbent for CO_2 Capture from Large-Point Sources. *Energy & Fuels* **2010,** *24* (8), 4598-4604. https://doi.org/10.1021/ef100447c
45. Dennis, J. S.; Pacciani, R., The rate and extent of uptake of CO_2 by a synthetic, CaO-containing sorbent. *Chemical Engineering Science* **2009,** *64* (9), 2147-2157. https://doi.org/10.1016/j.ces.2009.01.051
46. Li, Z.-s.; Cai, N.-s.; Huang, Y.-y., Effect of preparation temperature on cyclic CO_2 capture and multiple carbonation− calcination cycles for a new Ca-based CO_2 sorbent. *Industrial & Engineering Chemistry Research* **2006,** *45* (6), 1911-1917. https://doi.org/10.1021/ie0512111
47. Li, Z.-s.; Cai, N.-s.; Huang, Y.-y.; Han, H.-j., Synthesis, experimental studies, and analysis of a new calcium-based carbon dioxide absorbent. *Energy & Fuels* **2005,** *19* (4), 1447-1452. https://doi.org/10.1021/ef0496799
48. Radfarnia, H. R.; Iliuta, M. C., Metal oxide-stabilized calcium oxide CO_2 sorbent for multicycle operation. *Chemical Engineering Journal* **2013,** *232*, 280-289. https://doi.org/10.1016/j.cej.2013.07.049
49. Stendardo, S.; Andersen, L. K.; Herce, C., Self-activation and effect of regeneration conditions in CO_2–carbonate looping with CaO–$Ca_{12}Al_{14}O_{33}$ sorbent. *Chemical Engineering Journal* **2013,** *220*, 383-394. https://doi.org/10.1016/j.cej.2013.01.045
50. Sayyah, M.; Ito, B. R.; Rostam-Abadi, M.; Lu, Y.; Suslick, K. S., CaO-based sorbents for CO_2 capture prepared by ultrasonic spray pyrolysis. *RSC Advances* **2013,** *3* (43). https://doi.org/10.1039/c3ra44566f
51. Kim, J.-N.; Ko, C. H.; Yi, K. B., Sorption enhanced hydrogen production using one-body CaO–$Ca_{12}Al_{14}O_{33}$–Ni composite as catalytic absorbent. *International Journal of Hydrogen Energy* **2013,** *38* (14), 6072-6078. https://doi.org/10.1016/j.ijhydene.2012.12.022
52. Kierzkowska, A. M.; Poulikakos, L. V.; Broda, M.; Müller, C. R., Synthesis of calcium-based, Al_2O_3-stabilized sorbents for CO_2 capture using a co-precipitation technique. *International Journal of Greenhouse Gas Control* **2013,** *15*, 48-54. https://doi.org/10.1016/j.ijggc.2013.01.046
53. Lu, H.; Khan, A.; Pratsinis, S. E.; Smirniotis, P. G., Flame-made durable doped-CaO nanosorbents for CO_2 capture. *Energy & Fuels* **2009,** *23* (2), 1093-1100. https://doi.org/10.1021/ef8007882
54. Koirala, R.; Gunugunuri, K. R.; Pratsinis, S. E.; Smirniotis, P. G., Effect of zirconia doping on the structure and stability of CaO-based sorbents for CO_2 capture during extended operating cycles. *The Journal of Physical Chemistry C* **2011,** *115* (50), 24804-24812. https://doi.org/10.1021/jp207625c
55. Zhao, C.; Zhou, Z.; Cheng, Z., Sol–gel-Derived Synthetic CaO-Based CO_2 Sorbents Incorporated with Different Inert Materials. *Industrial & Engineering Chemistry Research* **2014,** *53* (36), 14065-14074. https://doi.org/10.1021/ie502559t
56. Hu, Y.; Liu, W.; Chen, H.; Zhou, Z.; Wang, W.; Sun, J.; Yang, X.; Li, X.; Xu, M., Screening of inert solid supports for CaO-based sorbents for high temperature CO_2 capture. *Fuel* **2016,** *181*, 199-206. https://doi.org/10.1016/j.fuel.2016.04.138
57. Reddy, E. P.; Smirniotis, P. G., High-temperature sorbents for CO_2 made of alkali metals doped on CaO supports. *The journal of physical chemistry B* **2004,** *108* (23), 7794-7800. https://doi.org/10.1021/jp031245b
58. Lee, C. H.; Mun, S.; Lee, K. B., Characteristics of Na–Mg double salt for high-temperature CO_2 sorption. *Chemical Engineering Journal* **2014,** *258*, 367-373. https://doi.org/10.1016/j.cej.2014.07.082
59. Wu, S. F.; Lan, P. Q., A kinetic model of nano-CaO reactions with CO_2 in a sorption complex catalyst. *AIChE Journal* **2012,** *58* (5), 1570-1577. https://doi.org/10.1002/aic.12675
60. Lee, C. H.; Choi, S. W.; Yoon, H. J.; Kwon, H. J.; Lee, H. C.; Jeon, S. G.; Lee, K. B., Na2CO3-doped CaO-based high-temperature CO_2 sorbent and its sorption kinetics. *Chemical Engineering Journal* **2018,** *352*, 103-109. https://doi.org/10.1016/j.cej.2018.06.141
61. Al-Mamoori, A.; Thakkar, H.; Li, X.; Rownaghi, A. A.; Rezaei, F., Development of potassium- and sodium-promoted CaO adsorbents for CO_2 capture at high temperatures.

Industrial & Engineering Chemistry Research **2017,** *56* (29), 8292-8300. https://doi.org/10.1021/acs.iecr.7b01587
62. Huang, L.; Xu, C.; Ren, R.; Zheng, Q.; Wang, Z.; Louis, B.; Wang, Q., Revealing how molten salts promote CO_2 capture on CaO via an impedance study and sorption kinetics simulation. *Sustainable Energy & Fuels* **2018,** *2* (1), 68-72. https://doi.org/10.1039/c7se00502d
63. Huang, L.; Zhang, Y.; Gao, W.; Harada, T.; Qin, Q.; Zheng, Q.; Hatton, T. A.; Wang, Q., Alkali Carbonate Molten Salt Coated Calcium Oxide with Highly Improved Carbon Dioxide Capture Capacity. *Energy Technology* **2017,** *5* (8), 1328-1336. https://doi.org/10.1002/ente.201600628
64. Xiao, G.; Singh, R.; Chaffee, A.; Webley, P., Advanced adsorbents based on MgO and K_2CO_3 for capture of CO_2 at elevated temperatures. *International Journal of Greenhouse Gas Control* **2011,** *5* (4), 634-639. https://doi.org/10.1016/j.ijggc.2011.04.002
65. Zhang, K.; Li, X. S.; Duan, Y.; King, D. L.; Singh, P.; Li, L., Roles of double salt formation and $NaNO_3$ in Na_2CO_3-promoted MgO absorbent for intermediate temperature CO_2 removal. *International Journal of Greenhouse Gas Control* **2013,** *12*, 351-358. https://doi.org/10.1016/j.ijggc.2012.11.013
66. Lee, C. H.; Kwon, H. J.; Lee, H. C.; Kwon, S.; Jeon, S. G.; Lee, K. B., Effect of pH-controlled synthesis on the physical properties and intermediate-temperature CO_2 sorption behaviors of K–Mg double salt-based sorbents. *Chemical Engineering Journal* **2016,** *294*, 439-446. https://doi.org/10.1016/j.cej.2016.03.003
67. Rong, N.; Wang, Q.; Fang, M.; Cheng, L.; Luo, Z.; Cen, K., Steam Hydration Reactivation of CaO-Based Sorbent in Cyclic Carbonation/Calcination for CO_2 Capture. *Energy & Fuels* **2013,** *27* (9), 5332-5340. https://doi.org/10.1021/ef4007214
68. Shokrollahi Yancheshmeh, M.; Radfarnia, H. R.; Iliuta, M. C., High temperature CO_2 sorbents and their application for hydrogen production by sorption enhanced steam reforming process. *Chemical Engineering Journal* **2016,** *283*, 420-444. https://doi.org/10.1016/j.cej.2015.06.060
69. Symonds, R. T.; Lu, D. Y.; Hughes, R. W.; Anthony, E. J.; Macchi, A., CO_2 capture from simulated syngas via cyclic carbonation/calcination for a naturally occurring limestone: pilot-plant testing. *Industrial & engineering chemistry research* **2009,** *48* (18), 8431-8440. https://doi.org/10.1021/ie900645x
70. Wang, Y.; Lin, S.; Suzuki, Y., Limestone calcination with CO_2 capture (II): decomposition in CO_2/steam and CO_2/N_2 atmospheres. *Energy & fuels* **2008,** *22* (4), 2326-2331. https://doi.org/10.1021/ef800039k
71. Yang, S.; Xiao, Y., Steam catalysis in CaO carbonation under low steam partial pressure. *Industrial & engineering chemistry research* **2008,** *47* (12), 4043-4048. https://doi.org/10.1021/ie8000265
72. Symonds, R. T.; Lu, D. Y.; Macchi, A.; Hughes, R. W.; Anthony, E. J., CO_2 capture from syngas via cyclic carbonation/calcination for a naturally occurring limestone: Modelling and bench-scale testing. *Chemical Engineering Science* **2009,** *64* (15), 3536-3543. https://doi.org/10.1016/j.ces.2009.04.043
73. Broda, M.; Manovic, V.; Anthony, E. J.; Muller, C. R., Effect of pelletization and addition of steam on the cyclic performance of carbon-templated, CaO-based CO_2 sorbents. *Environ Sci Technol* **2014,** *48* (9), 5322-8. https://doi.org/10.1021/es405668f
74. Manovic, V.; Anthony, E. J., Steam Reactivation of Spent CaO-Based Sorbent for Multiple CO_2 Capture Cycles. *Environmental Science & Technology* **2007,** *41* (4), 1420-1425. https://doi.org/10.1021/es0621344
75. Materic, V.; Hyland, M.; Jones, M. I.; Holt, R., Investigation of the friability of Ca looping sorbents during and after hydration based reactivation. *Fuel* **2014,** *127*, 70-77. https://doi.org/10.1016/j.fuel.2013.09.061
76. Martínez, I.; Grasa, G.; Murillo, R.; Arias, B.; Abanades, J. C., Evaluation of CO_2 Carrying Capacity of Reactivated CaO by Hydration. *Energy & Fuels* **2011,** *25* (3), 1294-1301. https://doi.org/10.1021/ef1015582

77. Salaudeen, S. A.; Acharya, B.; Dutta, A., CaO-based CO_2 sorbents: a review on screening, enhancement, cyclic stability, regeneration and kinetics modelling. *Journal of CO_2 Utilization* **2018,** *23*, 179-199. https://doi.org/10.1016/j.jcou.2017.11.012
78. Radfarnia, H. R.; Iliuta, M. C., Development of zirconium-stabilized calcium oxide absorbent for cyclic high-temperature CO_2 capture. *Industrial & Engineering Chemistry Research* **2012,** *51* (31), 10390-10398. https://doi.org/10.1021/ie301287k
79. Zhao, M.; Bilton, M.; Brown, A. P.; Cunliffe, A. M.; Dvininov, E.; Dupont, V.; Comyn, T. P.; Milne, S. J., Durability of CaO–$CaZrO_3$ Sorbents for High-Temperature CO_2 Capture Prepared by a Wet Chemical Method. *Energy & Fuels* **2014,** *28* (2), 1275-1283. https://doi.org/10.1021/ef4020845
80. Broda, M.; Müller, C. R., Sol–gel-derived, CaO-based, ZrO_2-stabilized CO_2 sorbents. *Fuel* **2014,** *127*, 94-100. https://doi.org/10.1016/j.fuel.2013.08.004
81. Martavaltzi, C. S.; Lemonidou, A. A., Parametric study of the CaO− Ca12Al14O33 synthesis with respect to high CO_2 sorption capacity and stability on multicycle operation. *Industrial & engineering chemistry research* **2008,** *47* (23), 9537-9543. https://doi.org/10.1021/ie800882d
82. Broda, M.; Kierzkowska, A. M.; Muller, C. R., Influence of the calcination and carbonation conditions on the CO_2 uptake of synthetic Ca-based CO_2 sorbents. *Environ Sci Technol* **2012,** *46* (19), 10849-56. https://doi.org/10.1021/es302757e
83. Luo, C.; Zheng, Y.; Yin, J.; Qin, C.; Ding, N.; Zheng, C.; Feng, B., Effect of support material on carbonation and sulfation of synthetic CaO-based sorbents in calcium looping cycle. *Energy & Fuels* **2013,** *27* (8), 4824-4831. https://doi.org/10.1021/ef400564j
84. Li, Y.; Su, M.; Xie, X.; Wu, S.; Liu, C., CO_2 capture performance of synthetic sorbent prepared from carbide slag and aluminum nitrate hydrate by combustion synthesis. *Applied Energy* **2015,** *145*, 60-68. https://doi.org/10.1016/j.apenergy.2015.01.061
85. Aihara, M.; Nagai, T.; Matsushita, J.; Negishi, Y.; Ohya, H., Development of porous solid reactant for thermal-energy storage and temperature upgrade using carbonation/decarbonation reaction. *Applied Energy* **2001,** *69* (3), 225-238. https://doi.org/10.1016/S0306-2619(00)00072-6
86. Wu, S.; Zhu, Y., Behavior of $CaTiO_3$/nano-CaO as a CO_2 reactive adsorbent. *Industrial & Engineering Chemistry Research* **2010,** *49* (6), 2701-2706. https://doi.org/10.1021/ie900900r
87. Albrecht, K. O.; Wagenbach, K. S.; Satrio, J. A.; Shanks, B. H.; Wheelock, T. D., Development of a CaO-based CO_2 sorbent with improved cyclic stability. *Industrial & Engineering Chemistry Research* **2008,** *47* (20), 7841-7848. https://doi.org/10.1021/ie8007743
88. Li, L.; King, D. L.; Nie, Z.; Howard, C., Magnesia-stabilized calcium oxide absorbents with improved durability for high temperature CO_2 capture. *Industrial & Engineering Chemistry Research* **2009,** *48* (23), 10604-10613. https://doi.org/10.1021/ie901166b
89. Lan, P.; Wu, S., Synthesis of a Porous Nano-CaO/MgO-Based CO_2 Adsorbent. *Chemical Engineering & Technology* **2014,** *37* (4), 580-586. https://doi.org/10.1002/ceat.201300709
90. Li, L.; King, D. L.; Nie, Z.; Li, X. S.; Howard, C., $MgAl_2O_4$ spinel-stabilized calcium oxide absorbents with improved durability for high-temperature CO_2 capture. *Energy & Fuels* **2010,** *24* (6), 3698-3703. https://doi.org/10.1021/ef100245q
91. Derevschikov, V. S.; Lysikov, A. I.; Okunev, A. G., High temperature CaO/Y_2O_3 carbon dioxide absorbent with enhanced stability for sorption-enhanced reforming applications. *Industrial & Engineering Chemistry Research* **2011,** *50* (22), 12741-12749. https://doi.org/10.1021/ie2015334
92. Zhang, X.; Li, Z.; Peng, Y.; Su, W.; Sun, X.; Li, J., Investigation on a novel CaO–Y_2O_3 sorbent for efficient CO_2 mitigation. *Chemical Engineering Journal* **2014,** *243*, 297-304. https://doi.org/10.1016/j.cej.2014.01.017

93. Zhao, M.; Yang, X.; Church, T. L.; Harris, A. T., Novel CaO-SiO_2 sorbent and bifunctional Ni/Co-CaO/SiO_2 complex for selective H_2 synthesis from cellulose. *Environ Sci Technol* **2012,** *46* (5), 2976-83. https://doi.org/10.1021/es300135d
94. Hu, Y.; Liu, W.; Sun, J.; Li, M.; Yang, X.; Zhang, Y.; Xu, M., Incorporation of CaO into novel Nd_2O_3 inert solid support for high temperature CO_2 capture. *Chemical Engineering Journal* **2015,** *273*, 333-343. https://doi.org/10.1016/j.cej.2015.03.074
95. Wang, S.; Fan, S.; Fan, L.; Zhao, Y.; Ma, X., Effect of cerium oxide doping on the performance of CaO-based sorbents during calcium looping cycles. *Environ Sci Technol* **2015,** *49* (8), 5021-7. https://doi.org/10.1021/es5052843
96. Bhatia, S.; Perlmutter, D., Effect of the product layer on the kinetics of the CO_2-lime reaction. *AIChE Journal* **1983,** *29* (1), 79-86. https://doi.org/10.1002/aic.690290111
97. Roesch, A.; Reddy, E. P.; Smirniotis, P. G., Parametric study of Cs/CaO sorbents with respect to simulated flue gas at high temperatures. *Industrial & engineering chemistry research* **2005,** *44* (16), 6485-6490. https://doi.org/10.1021/ie0402741
98. Duan, Y.; Zhang, K.; Li, X. S.; King, D. L.; Li, B.; Zhao, L.; Xiao, Y., ab initio Thermodynamic study of the CO_2 capture properties of M_2CO_3 (M = Na, K)- and $CaCO_3$-promoted MgO sorbents towards forming double salts. *Aerosol and Air Quality Research* **2014,** *14* (2), 470-479. https://doi.org/10.4209/aaqr.2013.05.0178
99. IEA *The Future of Hydrogen*; Paris, 2019.
100. IEA *Hydrogen Production and Storage*; Paris, 2006.
101. Di Giuliano, A.; Gallucci, K., Sorption enhanced steam methane reforming based on nickel and calcium looping: a review. *Chemical Engineering and Processing - Process Intensification* **2018,** *130*, 240-252. https://doi.org/10.1016/j.cep.2018.06.021
102. Barelli, L.; Bidini, G.; Gallorini, F.; Servili, S., Hydrogen production through sorption-enhanced steam methane reforming and membrane technology: a review. *Energy* **2008,** *33* (4), 554-570. https://doi.org/10.1016/j.energy.2007.10.018
103. Fernández, J. R.; Abanades, J. C., Sorption enhanced reforming of methane combined with an iron oxide chemical loop for the production of hydrogen with CO_2 capture: Conceptual design and operation strategy. *Applied Thermal Engineering* **2017,** *125*, 811-822. https://doi.org/10.1016/j.applthermaleng.2017.07.063
104. Broda, M.; Manovic, V.; Imtiaz, Q.; Kierzkowska, A. M.; Anthony, E. J.; Muller, C. R., High-purity hydrogen via the sorption-enhanced steam methane reforming reaction over a synthetic CaO-based sorbent and a Ni catalyst. *Environ Sci Technol* **2013,** *47* (11), 6007-14. https://doi.org/10.1021/es305113p
105. Harrison, D. P., Sorption-enhanced hydrogen production: a review. *Industrial & Engineering Chemistry Research* **2008,** *47* (17), 6486-6501. https://doi.org/10.1021/ie800298z
106. Carvill, B. T.; Hufton, J. R.; Anand, M.; Sircar, S., Sorption-enhanced reaction process. *AIChE Journal* **1996,** *42* (10), 2765-2772. https://doi.org/10.1002/aic.690421008
107. Balasubramanian, B.; Ortiz, A. L.; Kaytakoglu, S.; Harrison, D., Hydrogen from methane in a single-step process. *Chemical Engineering Science* **1999,** *54* (15-16), 3543-3552. https://doi.org/10.1016/S0009-2509(98)00425-4
108. García-Lario, A. L.; Grasa, G. S.; Murillo, R., Performance of a combined CaO-based sorbent and catalyst on H_2 production, via sorption enhanced methane steam reforming. *Chemical Engineering Journal* **2015,** *264*, 697-705. https://doi.org/10.1016/j.cej.2014.11.116
109. Di Giuliano, A.; Girr, J.; Massacesi, R.; Gallucci, K.; Courson, C., Sorption enhanced steam methane reforming by Ni–CaO materials supported on mayenite. *International Journal of Hydrogen Energy* **2017,** *42* (19), 13661-13680. https://doi.org/10.1016/j.ijhydene.2016.11.198
110. Cesário, M. R.; Barros, B. S.; Courson, C.; Melo, D. M. A.; Kiennemann, A., Catalytic performances of Ni–CaO–mayenite in CO_2 sorption enhanced steam methane reforming. *Fuel Processing Technology* **2015,** *131*, 247-253. https://doi.org/10.1016/j.fuproc.2014.11.028
111. Chanburanasiri, N.; Ribeiro, A. M.; Rodrigues, A. E.; Arpornwichanop, A.; Laosiripojana, N.; Praserthdam, P.; Assabumrungrat, S., Hydrogen production via sorption

enhanced steam methane reforming process using Ni/CaO multifunctional catalyst. *Industrial & Engineering Chemistry Research* **2011,** *50* (24), 13662-13671. https://doi.org/10.1021/ie201226j
112. Broda, M.; Kierzkowska, A. M.; Baudouin, D.; Imtiaz, Q.; Copéret, C.; Müller, C. R., Sorbent-enhanced methane reforming over a Ni–Ca-based, bifunctional catalyst sorbent. *ACS Catalysis* **2012,** *2* (8), 1635-1646. https://doi.org/10.1021/cs300247g
113. Broda, M.; Kierzkowska, A. M.; Müller, C. R., Sorbent-enhanced steam methane reforming reaction studied over a Ca-based CO_2 sorbent and Ni catalyst. *Chemical Engineering & Technology* **2013,** *36* (9), 1496-1502. https://doi.org/10.1002/ceat.201200643
114. Radfarnia, H. R.; Iliuta, M. C., Development of Al-stabilized CaO–nickel hybrid sorbent–catalyst for sorption-enhanced steam methane reforming. *Chemical Engineering Science* **2014,** *109*, 212-219. https://doi.org/10.1016/j.ces.2014.01.033
115. Radfarnia, H. R.; Iliuta, M. C., Hydrogen production by sorption-enhanced steam methane reforming process using CaO-Zr/Ni bifunctional sorbent–catalyst. *Chemical Engineering and Processing: Process Intensification* **2014,** *86*, 96-103. https://doi.org/10.1016/j.cep.2014.10.014
116. Zhao, C.; Zhou, Z.; Cheng, Z.; Fang, X., Sol-gel-derived, $CaZrO_3$-stabilized Ni/CaO-$CaZrO_3$ bifunctional catalyst for sorption-enhanced steam methane reforming. *Applied Catalysis B: Environmental* **2016,** *196*, 16-26. https://doi.org/10.1016/j.apcatb.2016.05.021
117. IEA *Putting CO_2 to use*; 2019.
118. Peter Styring, E. A. Q., Katy Armstrong, *Carbon Dioxide Utilisation: Closing the Carbon Cycle*. 2014.
119. Daza, Y. A.; Kuhn, J. N., CO_2 conversion by reverse water gas shift catalysis: comparison of catalysts, mechanisms and their consequences for CO_2 conversion to liquid fuels. *RSC Advances* **2016,** *6* (55), 49675-49691. https://doi.org/10.1039/c6ra05414e
120. González-Castaño, M.; Dorneanu, B.; Arellano-García, H., The reverse water gas shift reaction: a process systems engineering perspective. *Reaction Chemistry & Engineering* **2021,** *6* (6), 954-976. https://doi.org/10.1039/d0re00478b
121. Joo, O.-S.; Jung, K.-D.; Moon, I.; Rozovskii, A. Y.; Lin, G. I.; Han, S.-H.; Uhm, S.-J., Carbon dioxide hydrogenation to form methanol via a reverse-water-gas-shift reaction (the CAMERE process). *Industrial & Engineering Chemistry Research* **1999,** *38* (5), 1808-1812. https://doi.org/10.1021/ie9806848
122. Su, X.; Yang, X.; Zhao, B.; Huang, Y., Designing of highly selective and high-temperature endurable RWGS heterogeneous catalysts: recent advances and the future directions. *Journal of Energy Chemistry* **2017,** *26* (5), 854-867. https://doi.org/10.1016/j.jechem.2017.07.006
123. Kaiser, P.; Unde, R. B.; Kern, C.; Jess, A., Production of liquid hydrocarbons with CO_2 as carbon source based on reverse water-gas shift and Fischer-Tropsch synthesis. *Chemie Ingenieur Technik* **2013,** *85* (4), 489-499. https://doi.org/10.1002/cite.201200179
124. Ginés, M. J. L.; Marchi, A. J.; Apesteguía, C. R., Kinetic study of the reverse water-gas shift reaction over $CuO/ZnO/Al_2O_3$ catalysts. *Applied Catalysis A: General* **1997,** *154* (1), 155-171. https://doi.org/10.1016/S0926-860X(96)00369-9
125. Chen, C.-S.; Cheng, W.-H.; Lin, S.-S., Mechanism of CO formation in reverse water–gas shift reaction over Cu/Al_2O_3 catalyst. *Catalysis letters* **2000,** *68* (1), 45-48. https://doi.org/10.1023/A:1019071117449
126. Fujita, S.-I.; Usui, M.; Takezawa, N., Mechanism of the reverse water gas shift reaction over Cu/ZnO catalyst. *Journal of Catalysis* **1992,** *134* (1), 220-225. https://doi.org/10.1016/0021-9517(92)90223-5
127. Goguet, A.; Meunier, F. C.; Tibiletti, D.; Breen, J. P.; Burch, R., Spectrokinetic investigation of reverse water-gas-shift reaction intermediates over a Pt/CeO_2 catalyst. *The Journal of Physical Chemistry B* **2004,** *108* (52), 20240-20246. https://doi.org/10.1021/jp047242w
128. Zhang, M.; Zijlstra, B.; Filot, I. A. W.; Li, F.; Wang, H.; Li, J.; Hensen, E. J. M., A theoretical study of the reverse water-gas shift reaction on Ni(111) and Ni(311) surfaces.

The Canadian Journal of Chemical Engineering **2019,** *98* (3), 740-748. https://doi.org/10.1002/cjce.23655
129. Zhu, M.; Ge, Q.; Zhu, X., Catalytic reduction of CO_2 to CO via reverse water gas shift reaction: recent advances in the design of active and selective supported metal catalysts. *Transactions of Tianjin University* **2020,** *26* (3), 172-187. https://doi.org/10.1007/s12209-020-00246-8
130. Chen, X.; Su, X.; Liang, B.; Yang, X.; Ren, X.; Duan, H.; Huang, Y.; Zhang, T., Identification of relevant active sites and a mechanism study for reverse water gas shift reaction over Pt/CeO_2 catalysts. *Journal of Energy Chemistry* **2016,** *25* (6), 1051-1057. https://doi.org/10.1016/j.jechem.2016.11.011
131. Jacobs, G.; Davis, B. H., Reverse water-gas shift reaction: steady state isotope switching study of the reverse water-gas shift reaction using *in situ* DRIFTS and a Pt/ceria catalyst. *Applied Catalysis A: General* **2005,** *284* (1), 31-38. https://doi.org/10.1016/j.apcata.2005.01.013
132. Xu, D.; Wang, Y.; Ding, M.; Hong, X.; Liu, G.; Tsang, S. C. E., Advances in higher alcohol synthesis from CO_2 hydrogenation. *Chem* **2021,** *7* (4), 849-881. https://doi.org/10.1016/j.chempr.2020.10.019
133. Kattel, S.; Liu, P.; Chen, J. G., Tuning selectivity of CO_2 hydrogenation reactions at the metal/oxide interface. *J Am Chem Soc* **2017,** *139* (29), 9739-9754. https://doi.org/10.1021/jacs.7b05362
134. Mathew, T.; Saju, S.; Raveendran, S. N., Survey of heterogeneous catalysts for the CO_2 reduction to CO via reverse water gas shift. In *Engineering Solutions for CO_2 Conversion*, 2021; pp 281-316.
135. Wang, L.-C.; Khazaneh, M. T.; Widmann, D.; Behm, R. J., TAP reactor studies of the oxidizing capability of CO_2 on a Au/CeO_2 catalyst– a first step toward identifying a redox mechanism in the reverse water–gas shift reaction. *Journal of catalysis* **2013,** *302*, 20-30. https://doi.org/10.1016/j.jcat.2013.02.021
136. Kim, G. J.; Lee, S. M.; Chang Hong, S.; Kim, S. S., Active oxygen species adsorbed on the catalyst surface and its effect on formaldehyde oxidation over Pt/TiO_2 catalysts at room temperature; role of the Pt valence state on this reaction? *RSC Advances* **2018,** *8* (7), 3626-3636. https://doi.org/10.1039/C7RA11294G
137. Inoue, T.; Iizuka, T.; Tanabe, K., Hydrogenation of carbon dioxide and carbon monoxide over supported rhodium catalysts under 10 bar pressure. *Applied Catalysis* **1989,** *46* (1), 1-9. https://doi.org/10.1016/S0166-9834(00)81390-1
138. Pettigrew, D. J.; Trimm, D. L.; Cant, N. W., The effects of rare earth oxides on the reverse water-gas shift reaction on palladium/alumina. *Catalysis Letters* **1994,** *28* (2), 313-319. https://doi.org/10.1007/BF00806061
139. Wang, G.-C.; Nakamura, J., Structure sensitivity for forward and reverse water-gas shift reactions on copper surfaces: a DFT study. *The Journal of Physical Chemistry Letters* **2010,** *1* (20), 3053-3057. https://doi.org/10.1021/jz101150w
140. Chen, C.-S.; Cheng, W.-H.; Lin, S.-S., Enhanced activity and stability of a Cu/SiO_2 catalyst for the reverse water gas shift reaction by an iron promoter. *Chemical Communications* **2001,** (18), 1770-1771. https://doi.org/10.1039/B104279N
141. Chen, C.-S.; Cheng, W.-H., Study on the mechanism of CO formation in reverse water gas shift reaction over Cu/SiO_2 catalyst by pulse reaction, TPD and TPR. *Catalysis letters* **2002,** *83* (3), 121-126. https://doi.org/10.1023/A:1021006718974
142. Yoshihara, J.; Parker, S.; Schafer, A.; Campbell, C. T., Methanol synthesis and reverse water-gas shift kinetics over clean polycrystalline copper. *Catalysis letters* **1995,** *31* (4), 313-324. https://doi.org/10.1007/BF00808595
143. Nakamura, I.; Fujitani, T.; Uchijima, T.; Nakamura, J., The synthesis of methanol and the reverse water-gas shift reaction over Zn-deposited Cu (100) and Cu (110) surfaces: comparison with Zn/Cu (111). *Surface science* **1998,** *400* (1-3), 387-400. https://doi.org/10.1016/S0039-6028(97)00899-6

144. Loiland, J. A.; Wulfers, M. J.; Marinkovic, N. S.; Lobo, R. F., Fe/γ-Al_2O_3 and Fe–K/γ-Al_2O_3 as reverse water-gas shift catalysts. *Catalysis Science & Technology* **2016,** *6* (14), 5267-5279. https://doi.org/10.1039/c5cy02111a
145. Wolf, A.; Jess, A.; Kern, C., Syngas production via reverse water-gas shift reaction over a Ni-Al_2O_3 catalyst: catalyst stability, reaction kinetics, and modeling. *Chemical Engineering & Technology* **2016,** *39* (6), 1040-1048. https://doi.org/10.1002/ceat.201500548
146. Sun, F.-m.; Yan, C.-f.; Guo, C.-q.; Huang, S.-l., Ni/Ce–Zr–O catalyst for high CO_2 conversion during reverse water gas shift reaction (RWGS). *International journal of hydrogen energy* **2015,** *40* (46), 15985-15993. https://doi.org/10.1016/j.ijhydene.2015.10.004
147. Galhardo, T. S.; Braga, A. H.; Arpini, B. H.; Szanyi, J.; Goncalves, R. V.; Zornio, B. F.; Miranda, C. R.; Rossi, L. M., Optimizing Active Sites for High CO Selectivity during CO_2 Hydrogenation over Supported Nickel Catalysts. *J Am Chem Soc* **2021,** *143* (11), 4268-4280. https://doi.org/10.1021/jacs.0c12689
148. Pan, Y.-x.; Liu, C.-j.; Ge, Q., Effect of surface hydroxyls on selective CO_2 hydrogenation over Ni_4/γ-Al_2O_3: A density functional theory study. *Journal of Catalysis* **2010,** *272* (2), 227-234. https://doi.org/10.1016/j.jcat.2010.04.003
149. Zhang, R.; Wang, B.; Liu, H.; Ling, L., Effect of surface hydroxyls on CO_2 hydrogenation over Cu/γ-Al_2O_3 catalyst: a theoretical study. *The Journal of Physical Chemistry C* **2011,** *115* (40), 19811-19818. https://doi.org/10.1021/jp206065y
150. Graciani, J.; Mudiyanselage, K.; Xu, F.; Baber, A. E.; Evans, J.; Senanayake, S. D.; Stacchiola, D. J.; Liu, P.; Hrbek, J.; Sanz, J. F., Highly active copper-ceria and copper-ceria-titania catalysts for methanol synthesis from CO_2. *Science* **2014,** *345* (6196), 546-550. https://doi.org/10.1126/science.1253057
151. Kattel, S.; Yan, B.; Yang, Y.; Chen, J. G.; Liu, P., Optimizing binding energies of key intermediates for CO_2 hydrogenation to methanol over oxide-supported copper. *Journal of the American Chemical Society* **2016,** *138* (38), 12440-12450. https://doi.org/10.1021/jacs.6b05791
152. Tang, Q.-L.; Hong, Q.-J.; Liu, Z.-P., CO_2 fixation into methanol at Cu/ZrO_2 interface from first principles kinetic Monte Carlo. *Journal of Catalysis* **2009,** *263* (1), 114-122. https://doi.org/10.1016/j.jcat.2009.01.017
153. Larmier, K.; Liao, W. C.; Tada, S.; Lam, E.; Verel, R.; Bansode, A.; Urakawa, A.; Comas-Vives, A.; Copéret, C., CO_2-to-methanol hydrogenation on zirconia-supported copper nanoparticles: reaction intermediates and the role of the metal–support interface. *Angewandte Chemie International Edition* **2017,** *56* (9), 2318-2323. https://doi.org/10.1002/anie.201610166
154. Kattel, S.; Ramírez, P. J.; Chen, J. G.; Rodriguez, J. A.; Liu, P., Active sites for CO_2 hydrogenation to methanol on Cu/ZnO catalysts. *Science* **2017,** *355* (6331), 1296-1299. https://doi.org/10.1126/science.aal3573
155. Ye, J.; Liu, C.-j.; Mei, D.; Ge, Q., Methanol synthesis from CO_2 hydrogenation over a Pd_4/In_2O_3 model catalyst: A combined DFT and kinetic study. *Journal of catalysis* **2014,** *317*, 44-53. https://doi.org/10.1016/j.jcat.2014.06.002
156. Nakamura, I.; Nakano, H.; Fujitani, T.; Uchijima, T.; Nakamura, J., Synthesis and decomposition of formate on Cu(111) and Cu(110) surfaces: structure sensitivity. *Journal of Vacuum Science & Technology A* **1999,** *17* (4), 1592-1595. https://doi.org/10.1116/1.581856
157. Wang, G.-C.; Jiang, L.; Pang, X.-Y.; Cai, Z.-S.; Pan, Y.-M.; Zhao, X.-Z.; Morikawa, Y.; Nakamura, J., A theoretical study of surface-structural sensitivity of the reverse water-gas shift reaction over Cu(hkl) surfaces. *Surface Science* **2003,** *543* (1), 118-130. https://doi.org/10.1016/S0039-6028(03)00876-8
158. Sagar, G. V.; Rao, P. V. R.; Srikanth, C. S.; Chary, K. V. R., Dispersion and reactivity of copper catalysts supported on Al_2O_3−ZrO_2. *The Journal of Physical Chemistry B* **2006,** *110* (28), 13881-13888. https://doi.org/10.1021/jp0575153
159. Armbruster, M., Intermetallic compounds in catalysis - a versatile class of materials meets interesting challenges. *Sci Technol Adv Mater* **2020,** *21* (1), 303-322. https://doi.org/10.1080/14686996.2020.1758544

160. Furukawa, S.; Komatsu, T.; Shimizu, K.-i., Catalyst design concept based on a variety of alloy materials: a personal account and relevant studies. *Journal of Materials Chemistry A* **2020,** *8* (31), 15620-15645. https://doi.org/10.1039/d0ta03733h
161. Liu, K.; Qin, R.; Zheng, N., Insights into the interfacial effects in heterogeneous metal nanocatalysts toward selective hydrogenation. *J Am Chem Soc* **2021,** *143* (12), 4483-4499. https://doi.org/10.1021/jacs.0c13185
162. Gilroy, K. D.; Ruditskiy, A.; Peng, H.-C.; Qin, D.; Xia, Y., Bimetallic nanocrystals: syntheses, properties, and applications. *Chemical Reviews* **2016,** *116* (18), 10414-10472. https://doi.org/10.1021/acs.chemrev.6b00211
163. Williams, B. P.; Qi, Z.; Huang, W.; Tsung, C. K., The impact of synthetic method on the catalytic application of intermetallic nanoparticles. *Nanoscale* **2020,** *12* (36), 18545-18562. https://doi.org/10.1039/d0nr04699j
164. Zhou, M.; Li, C.; Fang, J., Noble-metal based random alloy and intermetallic nanocrystals: syntheses and applications. *Chem Rev* **2021,** *121* (2), 736-795. https://doi.org/10.1021/acs.chemrev.0c00436
165. Studt, F.; Sharafutdinov, I.; Abild-Pedersen, F.; Elkjaer, C. F.; Hummelshoj, J. S.; Dahl, S.; Chorkendorff, I.; Norskov, J. K., Discovery of a Ni-Ga catalyst for carbon dioxide reduction to methanol. *Nat Chem* **2014,** *6* (4), 320-4. https://doi.org/10.1038/nchem.1873
166. Kovnir, K.; Armbrüster, M.; Teschner, D.; Venkov, T. V.; Jentoft, F. C.; Knop-Gericke, A.; Grin, Y.; Schlögl, R., A new approach to well-defined, stable and site-isolated catalysts. *Science and Technology of Advanced Materials* **2007,** *8* (5), 420-427. https://doi.org/10.1016/j.stam.2007.05.004
167. Feng, Q.; Zhao, S.; Wang, Y.; Dong, J.; Chen, W.; He, D.; Wang, D.; Yang, J.; Zhu, Y.; Zhu, H.; Gu, L.; Li, Z.; Liu, Y.; Yu, R.; Li, J.; Li, Y., Isolated single-atom Pd sites in intermetallic nanostructures: high catalytic selectivity for semihydrogenation of alkynes. *J Am Chem Soc* **2017,** *139* (21), 7294-7301. https://doi.org/10.1021/jacs.7b01471
168. Porosoff, M. D.; Chen, J. G., Trends in the catalytic reduction of CO_2 by hydrogen over supported monometallic and bimetallic catalysts. *Journal of Catalysis* **2013,** *301*, 30-37. https://doi.org/10.1016/j.jcat.2013.01.022
169. Liu, D.; Li, Y.; Kottwitz, M.; Yan, B.; Yao, S.; Gamalski, A.; Grolimund, D.; Safonova, O. V.; Nachtegaal, M.; Chen, J. G.; Stach, E. A.; Nuzzo, R. G.; Frenkel, A. I., Identifying dynamic structural changes of active sites in Pt–Ni bimetallic catalysts using multimodal approaches. *ACS Catalysis* **2018,** *8* (5), 4120-4131. https://doi.org/10.1021/acscatal.8b00706
170. Durussel, P.; Burri, G.; Feschotte, P., The binary system Ni-In. *Journal of Alloys and Compounds* **1997,** *257* (1), 253-258. https://doi.org/10.1016/S0925-8388(97)00033-9
171. Chen, Y.; Chen, J., Selective hydrogenation of acetylene on SiO_2 supported Ni-In bimetallic catalysts: Promotional effect of In. *Applied Surface Science* **2016,** *387*, 16-27. https://doi.org/10.1016/j.apsusc.2016.06.067
172. Wang, L.; Niu, X.; Chen, J., SiO_2 supported Ni-In intermetallic compounds: efficient for selective hydrogenation of fatty acid methyl esters to fatty alcohols. *Applied Catalysis B: Environmental* **2020,** *278*. https://doi.org/10.1016/j.apcatb.2020.119293
173. Wang, X.; Chen, J., Effects of indium on Ni/SiO_2 catalytic performance in hydrodeoxygenation of anisole as model bio-oil compound: Suppression of benzene ring hydrogenation and C–C bond hydrogenolysis. *Chinese Journal of Catalysis* **2017,** *38* (11), 1818-1830. https://doi.org/10.1016/s1872-2067(17)62910-3
174. Li, C.; Chen, Y.; Zhang, S.; Xu, S.; Zhou, J.; Wang, F.; Wei, M.; Evans, D. G.; Duan, X., Ni–In intermetallic nanocrystals as efficient catalysts toward unsaturated aldehydes hydrogenation. *Chemistry of Materials* **2013,** *25* (19), 3888-3896. https://doi.org/10.1021/cm4021832
175. Károlyi, J.; Németh, M.; Evangelisti, C.; Sáfrán, G.; Schay, Z.; Horváth, A.; Somodi, F., Carbon dioxide reforming of methane over $Ni–In/SiO_2$ catalyst without coke formation. *Journal of Industrial and Engineering Chemistry* **2018,** *58*, 189-201. https://doi.org/10.1016/j.jiec.2017.09.024

Chapter 3 - OBJECTIVES

The main objective of this thesis is to develop strategies to (i) enhance the efficiency and stability of hybrid-material for application in sorption enhanced steam reforming process to produce high-purity hydrogen with simultaneous CO_2 capture, and (ii) to investigate the performance of intermetallic/alloy Ni-In catalyst and understand the relationship between the structure and activity/selectivity for the rWGS reaction.

Specifically, the objectives are:

i. Synthesize and characterize the Na_2CO_3-CaO and Ni/Al_2O_3 by precipitation method and incipient wetness impregnation, respectively.
ii. Understand the influence of sodium-doping in CaO-based sorbent for CO_2 capture.
iii. Investigate the performance of the physical mixture Ni/Al_2O_3 and the synthesized sorbent in sorption enhanced steam reforming of methane (SE-SRM).
iv. Synthesize different phases of Ni-In compounds by hydrothermal method.
v. Characterize the intermetallic/alloy compounds identifying the formed phases.
vi. Evaluate the performance of the bi metallic materials under various feed compositions in the reverse water gas shift.
vii. Identify the effect of the indium in the catalyst on the catalytic performance for the rWGS reaction.

Chapter 4 - Performance of sodium doping CaO-based sorbent in sorption-enhanced steam reforming of methane

4.1 Introduction

The use of hydrogen as a fuel has attracted interest due to many advantages such as waste-free combustion and high energy mass density. Hydrogen is also used as a raw material in several processes such as ammonia, urea and methanol synthesis, hydrocracking and hydroprocessing in refineries, metallurgical processes, and glass production.[1, 2] There are many routes to obtain hydrogen, for instance, reforming of both fossil and renewable hydrocarbons, electrolysis of water, ammonia dissociation, and partial oxidation.[3] The most conventional way to obtain hydrogen is the steam methane reforming (SMR) because it is a relatively simple, low cost, and high efficiency compared with other processes.[4-6] Nevertheless, the SMR is a highly endothermic process occurring at high temperatures (above 700 °C), which can emit around 8-ton CO_2 per ton H_2 produced.[1, 7]

Thereby, a large research effort has been made in the last decades trying to improve the hydrogen production process with considerable low CO_2 emissions, since it is one of the main greenhouse gases. One technology that has received widespread attention is sorption-enhanced steam methane reforming (SE-SMR) that combines the steam reaction with simultaneous CO_2 capture in one vessel.[3, 5, 8, 9] The principle of the SE-SMR process is shifting the equilibrium of the reversible reactions (eq. 4.1 and 4.2) based on Le Chatelier's principle to produce high purity hydrogen with *in-situ* CO_2 capture with a sorbent material.[8-10] The key reactions of the process are the reform of methane with steam (eq. 4.1), water gas shift reaction (WGSR) (eq. 4.2) and CO_2 capture (eq. 4.3):

$CH_{4(g)} + H_2O_{(v)} \rightleftharpoons CO_{(g)} + 3H_{2(g)}$	ΔH°_{298K}= +206 kJ/mol	Eq. 4.1
$CO_{(g)} + H_2O_{(v)} \rightleftharpoons CO_{2(g)} + H_{2(g)}$	ΔH°_{298K}= -41 kJ/mol	Eq. 4.2
$CaO_{(s)} + CO_{2(g)} \rightleftharpoons CaCO_{3(s)}$	ΔH°_{298K}= -178 kJ/mol	Eq. 4.3

Some advantages presented by SE-SMR are higher efficiency in H_2 production, smaller emission of by-products (CO_2 and CO) to the atmosphere, and the possibility

to capture relatively pure CO_2 suitable for sequestration or use in different processes. Furthermore, in this type of process, the elimination of individual reactor for water-gas shift and further H_2 purification can be possible, using 20% to 25% less energy compared to the conventional SMR.[5, 11, 12]

Many materials are used as CO_2 sorbents such as zeolites, activated carbon, metal-based sorbents, ceramic materials (e. g. hydrotalcite, CaO, MgO, Li_2ZrO_3, Li_4SiO_4, and Na_2ZrO_3), and organic materials (e.g. amines and Metal-Organic Frameworks (MOF's).[13] Among all of these materials, calcium oxide is the most studied one. The wide availability in nature as limestone or dolomite, low-cost raw material, high CO_2 sorption capacity, and adequate kinetics reaction are the advantages presented by CaO.[14, 15] Another important characteristic is the high temperature for CO_2 adsorption proved by calcium oxide which is usually required for SE-SMR (e. g. 600 °C to 800 °C). On the other hand, the main disadvantage of CaO is the fast deactivation and loss of CO_2 capacity by sintering phenomenon and blocking pores during the operation time. Consequently, some approaches have been developed to overcome the drawback related to the stability of sorbent such as the use of different calcium precursors, incorporation of inert support, additional treatments (e.g. hydration, thermal and chemical pretreatments), preparation technique (e.g. wet-mixing, co-precipitation, sol-gel, dry-mixing, etc.) and the doping with alkali metal components for double salt formation.[16-22]

Focusing on the doping approach of CaO based sorbents, Al-Mamoori et al.[16] studied the development of a series of double salts such as potassium-promoted calcium (K−Ca) and sodium-promoted calcium (Na−Ca) adsorbents for CO_2 capture. In general, they concluded that the addition of K and Na improved the performance of CaO since these materials presented high CO_2 sorption capacity, fast kinetics, and good stability (only for K-Ca) above 300 °C. Lee et al.[17] performed a comparative study of sorption and regeneration kinetics of synthesized CaO doped with Na_2CO_3 and conventional CaO sorbent. In this study, the authors concluded that the addition of sodium carbonate in calcium sorbent can improve the cyclic stability of CO_2 sorption with fast kinetics.

Based on these studies that only approached the carbonation/calcination performance, the objective of this work was to investigate the applicability and feasibility of sodium doping in the Ca-based sorbent for sorption enhanced steam methane reforming. Further, the physico-chemical properties of the sorbents were

evaluated to explain the performance of the physical mixture between Ni/γ-Al_2O_3 and the synthesized sorbent in the cyclic SE-SMR.

4.2 Experimental section

4.2.1 Solids preparation

The double-salts materials were prepared using the precipitation method previously reported by Lee and coworkers.[17] For the synthesis of Na_2CO_3-CaO sorbent, 50 g of sodium carbonate (Na_2CO_3; Vetec, 99%) was gradually added to 500mL of 0.3 M calcium nitrate tetrahydrate ($Ca(NO_3)_2.4H_2O$; Dinâmica, 99%) solution. After that, the reactants were vigorously stirred for 1h and settled down for 9 h to form a precipitated slurry. The precipitated particles were separated using vacuum filtration and the filter cake was dried in an oven at 110 °C overnight. The dried mass was ground using a mortar and pestle and then thermally treated at 800° C under air condition for 10 h (heating rate 10 °C/min). For comparison, calcium oxide was prepared by calcination of calcium carbonate ($CaCO_3$; Synth, 99%) in the same conditions used for double-salt samples.

To prepare 10%Ni/γ-Al_2O_3, Boehmite (AlO(OH), Catapal A Sasol) was calcined at 800 °C during 6 h (heating rate 10 °C/min). Then, the addition of nickel nitrate hexahydrate ($Ni(NO_3)_2.6H_2O$; Vetec, 97%) solution was made by an incipient wetness method. The samples were dried in an oven at 120 °C for 12 hours. Finally, the material was calcined under air conditions at 400 °C for 3 hours with a heating rate of 10 °C/min.

The final material used in the catalytic tests consisted of a physical mixture of Ni/Al_2O_3 and sorbent in a proportion of 1:1 (w/w). In this work, the mixed catalysts were denominated as NiCa for Ni/Al_2O_3 mixed with CaO and NiCaNa for Ni/Al_2O_3 mixed with Na_2CO_3/CaO.

4.2.2 Sorption-enhanced steam methane reforming (SE-SMR)

The catalytic tests coupled with CO_2 capture were carried out in a fixed bed reactor system. The quartz reactor was loaded with 4 g of a physical mixture of the

sample (50 wt.%:50wt.% Ni/Al_2O_3 – sorbent). The temperature was monitored by a thermocouple located next to the reactor. Prior to SE-SMR cycles, the catalyst was reduced at 800 °C in 23% H_2/Ar flow (total flow of 130 STD mL/min) for 1 hour. Figure 4.1 shows the SE-SMR cycles which consist of two stages. The first stage is the reforming reaction which was performed at 600 °C for 119 min. The flow rates of gases were 10 STD mL/min of CH_4, 100 STD mL/min of Ar, and 40 STD mL/min of water vapor. Steam was generated by a heater vaporized feed by a pump (LC20AT - Shimadzu). The exit flow from the reactor was transferred to a condenser to separate water before gas composition analysis, which was performed using a gas chromatograph equipped with a TCD detector and a Carboxen-1010 plot column (Shimadzu GC-2014). The second stage (regeneration) was conducted at 800 °C for 1 hour under the same atmosphere composition of the reduction step. The purpose of the presence of H_2 during regeneration was to maintain the Ni in the metallic state.[23, 24] The total cycle performed was 10. The conversion of methane (X_{CH_4}) and molar fraction in dry basis of species *i* (y_i) were calculated using Equations 4.4 and 4.5.

$$CH_4(\%) = \frac{\left(\left(n_{CH_4}\right)_{in} - \left(n_{CH_4}\right)_{out}\right)x100}{\left(n_{CH_4}\right)_{in}} \qquad \text{Eq. 4.4}$$

$$y_i = \frac{n_i}{\sum_{j=1}^{N} n_j} \qquad \text{Eq. 4.5}$$

where n_i and n_j are the numbers of moles on a dry basis in the gas phase of species *i* and *j* in the output stream of the reactor, being the species: H_2, CO, CH_4, CO_2.

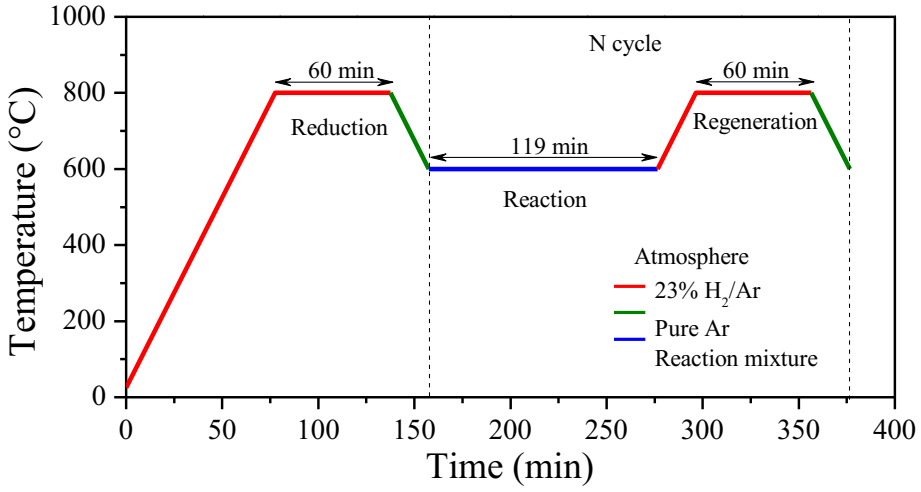

Figure 4.1: Schematic diagram of experimental steps during the SE-SMR cycles.

4.2.3 Characterizations

The surface area was determined by nitrogen adsorption at -196 °C in a Micromeritrics ASAP-2020 analyzer. The sample was degassed at 350 °C for 3 h prior to conducting the measurements. The Brunauer-Emmett-Teller (BET) model was used to calculate the surface area by the results of N_2 isotherms. Total pore volume was estimated from amount of N_2 adsorbed at relative pressure of 0.99. Morphological analyses were carried out using a scanning electron microscopy (SEM, Carl Zeiss, model EVO MA 10) equipped with energy dispersive spectroscopy (EDS, Oxford, model 51-ADD0048).

In-situ X-ray diffraction (XRD) was carried out at the XPD-10B beamline of Brazilian Synchrotron Light Laboratory (LNLS). The samples were placed into a furnace installed into a Huber goniometer operating in Bragg-Brentano geometry (θ - 2θ). The XRD patterns were obtained using a Mythen – 1 K detector (Dectris) located 1 m from the furnace, in a 2θ interval from 26° to 58° using a wavelength of 1.5498 Å. *In-situ* X-ray absorption near edge structure (XANES) analyses was performed at the Ni K-edge (8333 eV) using D06A-DXAS beamline of LNLS. Analyses were performed in scanning operating mode with a silicon monochromator Si (111). The Ni K-edge spectra were recorded in transmission mode from 8320 eV and 8370 eV. Both *in-situ* XRD and *in-situ* XANES analysis were carried out during the reduction process of the mixed material in the proportion of 50:50 (wt.%). The samples, already calcined, were heated in a 5% H_2/He (100 mL/min) flow from room temperature to 800 °C at 10 °C/min, remaining at the final temperature for 1 h. Energy calibration of the obtained XANES spectra, background subtraction, and normalization were all performed with open source PRESTOPRONTO software.

4.2.4 Determination of CO_2 sorption capacities

CO_2 sorption experiments were carried out at atmospheric pressure using a thermogravimetric analyzer (TGA 50/50H - SHIMADZU) for 20 cycles of carbonation/calcination. The amount of fresh sample used was, approximately, 10 mg for each experiment. Before starting the analyses, the samples were preheated at

800 °C for 10 min under pure He flow rate (50 mL/min) to removed impurities such as moisture and sorbates. The conditions adopted for each cycle were 30 min for carbonation at 600 °C (15% CO_2/He flow) and 10 min for calcination at 800 °C (pure He flow). The low partial pressure of CO_2 was selected to simulate the real composition of the reformer exit that does not surpass 15%. The total flow rate was 60 mL/min and the temperature rate up/down for each stage was maintained at 10 °C/min. The molar conversion of CaO was given by the following relationship:

$$\text{Molar conversion of CaO } (\%) = 100\frac{w_t - w_i}{w_i}\frac{1}{nX_t} \qquad \text{Eq. 4.6}$$

where w_t is the weight change of sample at time t, w_i is the initial weight of the sample, X_t is the theoretical mass uptake capacity of CO_2 by CaO (0.786g CO_2/g CaO) and n is the mole fraction of CaO in the sorbent.

4.3 Results and discussion

4.3.1 Sorption-enhanced reforming process

The performance of the synthesized materials for SE-SMR was explored by means of two variables, the methane conversion and the selectivity to hydrogen during 10 cycles. The CH_4 conversions for all cycles of both materials reached values close to 100% for SE-SMR at 600 °C and steam/carbon equals to 4. This can be justified by the high mass of the catalyst used which led the system to operate with large residence time and conversion. The conversion of methane was consistently close to 100%, which shows that the regeneration cycles were effective.

Next, the H_2 selectivity was analyzed to evaluate the efficiency of the Ca-based sorbent over the cycles and to compare the hydrogen purity with the conventional methane reforming process. Initially, we selected only the experimental data of the first cycle of reaction for NiCa catalyst. Thus, Figure 4.2 shows the molar fraction in dry basis of all components in the effluent reactor of the first cycle and thermodynamic equilibrium data (hollow symbols) which was calculated by NASA Chemical Equilibrium with Applications (CEA) software. During the whole cycle, the main products formed were H_2, CO, and CO_2. The initial points correspond to the start-up

of the system, followed by the stabilization. It is possible to observe three distinct periods that occur for methane reform combined with CO_2 capture, which are extensively reported in the literature. The pre-breakthrough (I) is the first period that has the maximum H_2 purity simultaneously with very low CO_2 molar fractions. Furthermore, the methane molar fraction is close to zero due to the high conversion. The next period is the breakthrough (II) when the sorbent starts to saturate with CO_2, losing its efficiency gradually. The last period is called post-breakthrough (III) and, by this time, the sorbent is already totally saturated and the molar fraction values in the effluent are the same as those shown only by the conventional steam reforming reaction.

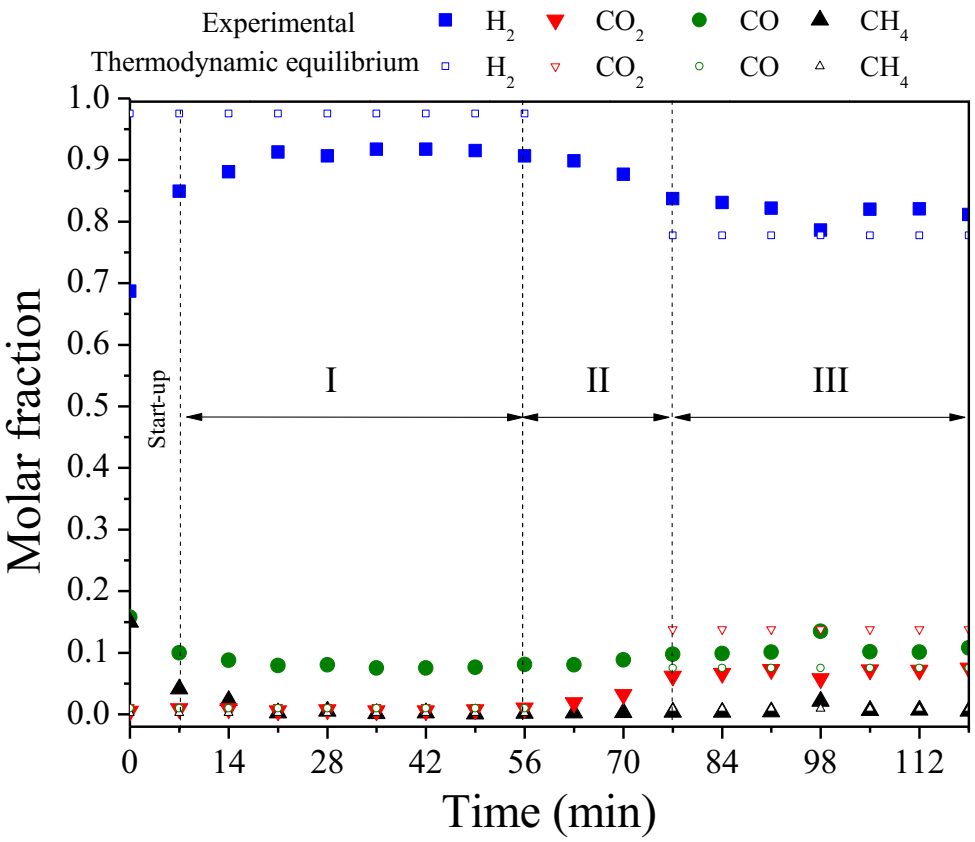

Figure 4.2: Gas effluent concentration in dry basis during the SE-SMR process using NiCa catalyst during the first reaction cycle. Reaction conditions: T = 600 °C, S/C= 4, m_{cat} = (2g Ni/Al_2O_3 + 2g CaO), Ar flow = 100 STD mL/min + CH_4 flow = 10 STD mL/min.

Figure 4.3 exhibits the experimental results obtained during sorption enhanced steam methane reforming (SE-SMR), in terms of the evolution of the H_2 and CO_2

molar fraction (dry basis) in gas composition with time (119 min) in the 1st, 5th and 10th cycle. The H_2 concentration in the effluent gas was 93.5 vol.% for all investigated materials, which is close to thermodynamic equilibrium (dashed line). After 119 minutes of reaction, the yield of H_2 reaches 80 vol.% and 10 vol.% for CO_2 production which is similar to values obtained by conventional steam methane reforming. The difference in the molar fraction of experimental data and thermodynamic values during the post-breakthrough period suggests that the reaction system did not reach the equilibrium state and a possible cause of this could be associated to residual effect of CO_2 capture by the bulk CaO. Furthermore, it can be seen that these values of H_2 and CO_2 yield remained practically constants for both catalysts after 10 cycles. From a practical view, the pre-breakthrough is the most important part of the SE-SMR process due to the high purity of H_2 in the gas effluent. Thereby, the length of the pre-breakthrough can be indicated how stable the absorbent is during the cyclic operation and it could be associated with the efficiency of the material. For NiCa, it was not possible to observe a significant difference in the length of the pre-breakthrough period indicating that this material was stable even submitted to 10 carbonation/calcination cycles. On the other hand, the NiCaNa sample did not exhibit good performance regarding the stability of the absorbent. The length of pre-breakthrough slightly diminished from 56 min to 42 min after 10 cycles. This poor performance presented by the sorbent with sodium doping was not expected since the results presented by the literature about carbonation/calcination process showed improvement by the presence of this alkaline material. Accordingly, to better elucidate why of the low stability in SE-SMR, we carried out characterizations experiments such as BET, MEV, *in situ* XRD, and CO_2 sorption tests of the synthesized sorbents.

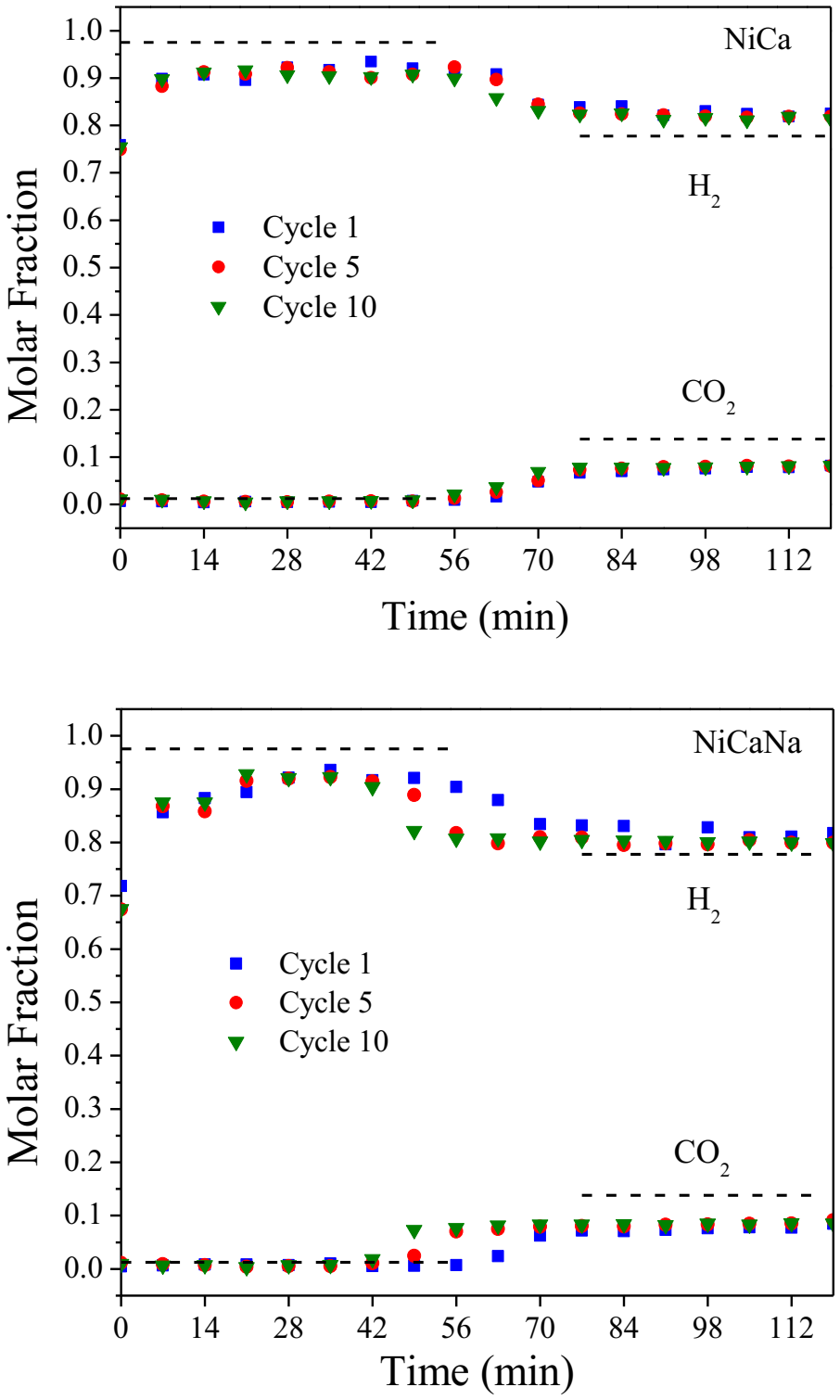

Figure 4.3: Profiles of H_2 and CO molar fraction on dry basis as a function of time during the SE-SMR for 1st, 5th, and 10th cycle. Conditions: T = 600 °C, S/C= 4, m_{cat} = (2g Ni/Al_2O_3 + 2g sorbent), Ar flow = 100 STD mL/min and CH_4 flow = 10 STD mL/min. (Dashed line: thermodynamic equilibrium).

4.3.2 Characterization of samples

The physical characteristics of the calcined fresh and used sorbent after 10 cycles of SE-SMR are summarized in Table 1. In general, the surface area of sorbents was higher than others presented in literature.[16, 17, 25, 26] Comparing the results of only sorbents, the sodium doping increased the BET area as well as the pore volume. Regarding to Ni/Al_2O_3 catalyst, the material presented a high surface area (129 m^2/g) due to presence of the alumina support, which was expected when compared with the literature results.[27, 28] To clarify, the nomination of the samples as fresh catalyst in Table 4.1 is the physical mixture of supported nickel catalyst with synthesized adsorbents. The BET surface areas of these mixtures were between the values presented by the pure materials (Ni/Al_2O_3 and adsorbents), as expected. It can be seen that neither BET surface area or pore volume values were not significantly changed after the 10 reaction/regeneration cycles. Overall, these BET results are not enough to explain the performance of the catalyst in SE-SMR requiring other characterization techniques.

Table 4.1: Textural properties of fresh and used catalysts.

Adsorbents	S_{BET} (m^2/g)	V_{pore} (cm^3/g_{cat})	d_{pore} [a] (nm)
CaO	30	0.075	7.5
Na_2CO_3/CaO	50	0.167	9.1
Ni/Al_2O_3	129	0.348	8.6
Fresh Catalyst			
NiCa	94	0.233	7.6
NiCaNa	98	0.260	8.1
Used Catalyst (after 10 cycles)			
NiCa	83	0.260	12.3
NiCaNa	94	0.264	10.9

[a] BJH pore diameter determined from the adsorption branch.

Thus, the morphology of fresh sorbents and the used catalysts was investigated by scanning electron microscopy (SEM). Figure 4.4a-d displays the fresh sorbent samples and Figure 4.4e-f shows the physical mixture between Ni/Al_2O_3 catalyst and

the sorbent after 10 SE-SMR cycles. Comparing the sorbent, the morphology presented by CaO was a granular and fluffy structure, differently from Na_2CO_3-CaO fresh sorbent which presented a melted-like, solid, and compact structure. The preparation method suggests being the main influence to lead this huge difference between the sorbent since the pure calcium oxide was synthesized by calcination of $CaCO_3$ and the Na-containing sample by precipitation method. The SEM images of the used catalyst (Figure 4.4e-f) showed two distinct phases, one represents the sorbent (fluffy structure) and the other represents Ni/Al_2O_3 phase (rounded particles). Figure 4.5 exhibits the element mapping of Ca, Na, and O for the Na-containing sample. It is possible to observe that the sodium is homogeneously dispersed over the sorbent indicating that it is well distributed and remained retained in the filtered cake, during the preparation step.

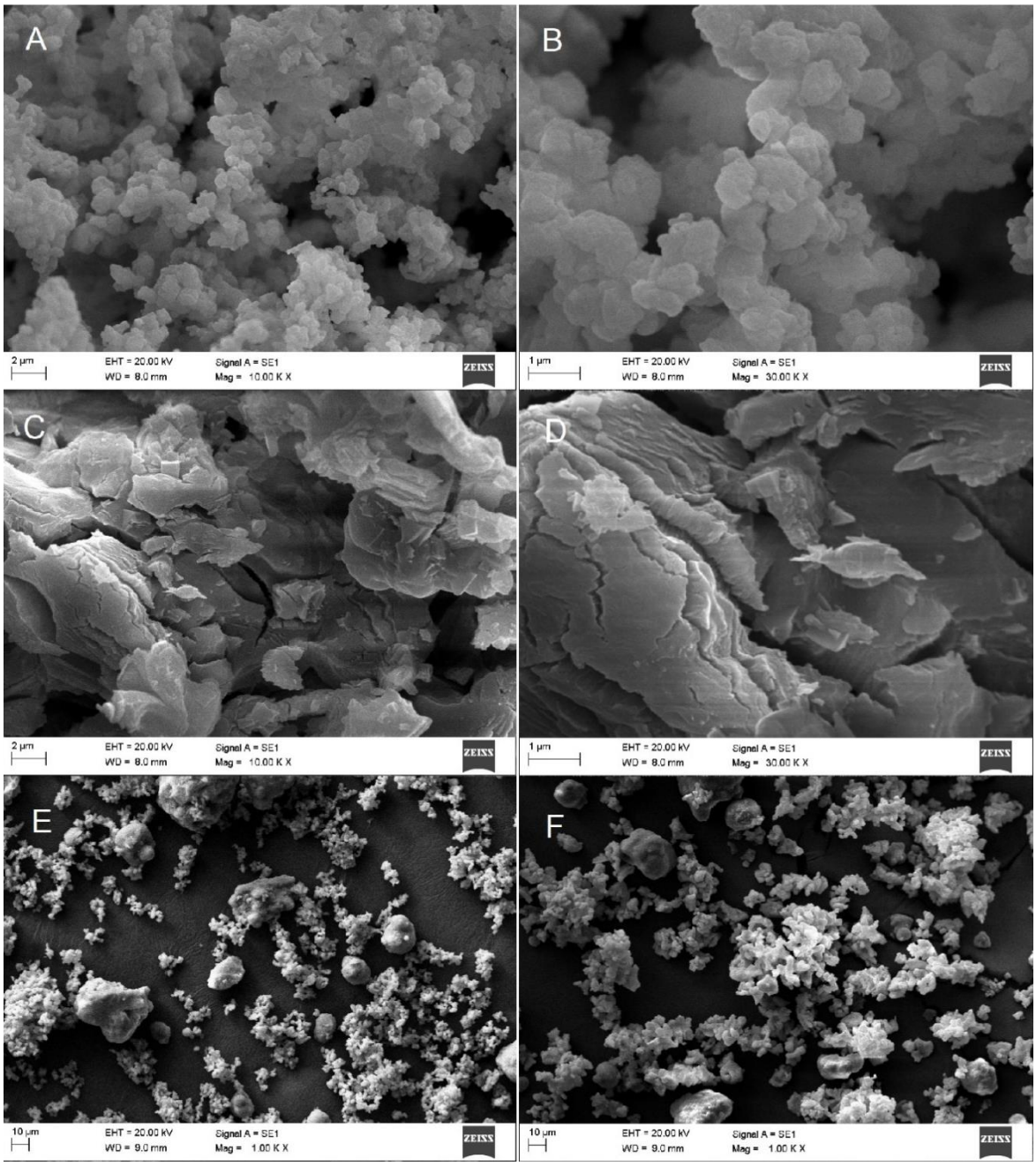

Figure 4.4: SEM images of (A and B) fresh CaO, (C and D) fresh Na_2CO_3-CaO, (E) used NiCa, and (F) used NiNaCa.

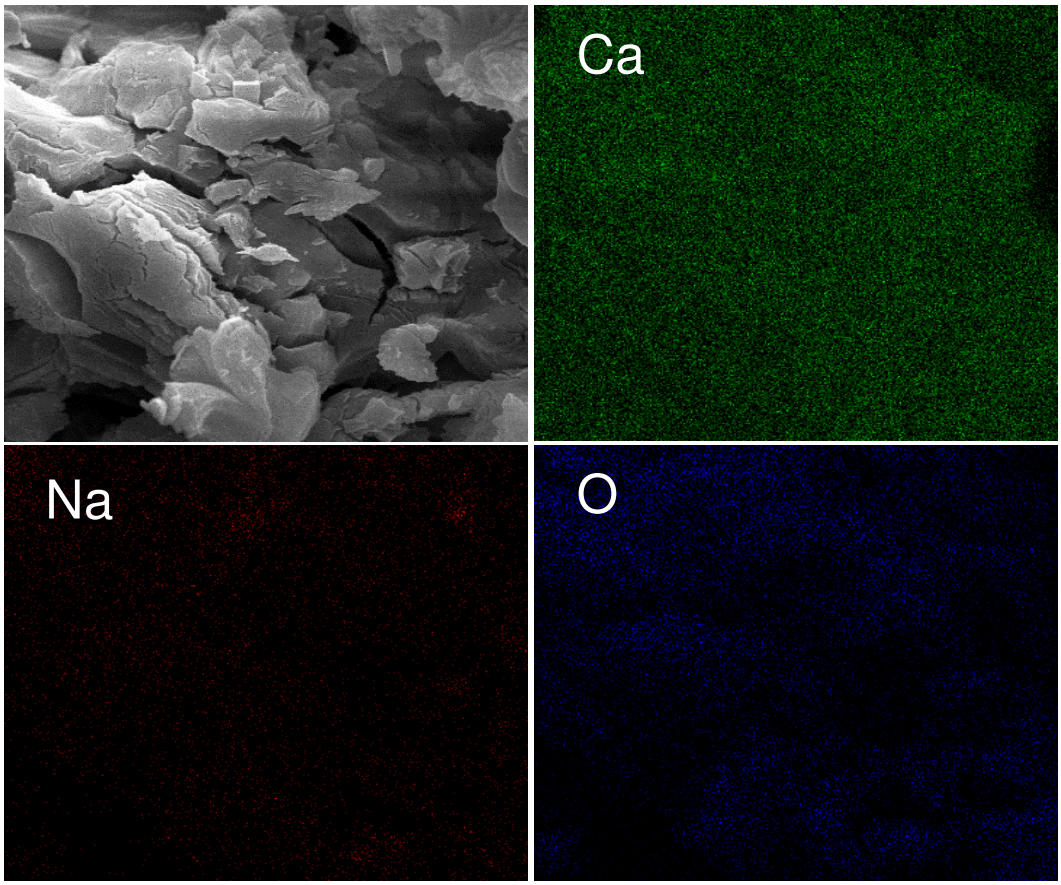

Figure 4.5: EDS mapping of fresh CaNa sample.

The XRD data of the samples at room temperature are presented in Figure 4.6. The diffractograms revealed intense and characteristics peaks at 32.2° [1 1 1], 37.4° [0 2 0] and 53.9° [2 -2 0] that are correlated to calcium oxide according to the ICSD 51409. The diffraction peaks at 28.7° [1 -1 0], 34.2° [1 -1 1], 47.3° [0 1 -2], 51.0° [2 -1 0] and 54.5° [1 1 -1] are associated to $Ca(OH)_2$ and this occurs due to the hygroscopic nature of CaO. At a much lower intensity than CaO, diffraction peaks at 37.3° [1 1 1] and 43.3° [0 2 0] attributed to NiO (ICSD 9866), which represent the active phase of the material.[1, 7, 29] No detectable peaks related to phases of sodium were evidenced by the diffractogram of NiCaNa (Figure 4.6) which can be due to fact that this species is present in small quantity and could be finely dispersed on the surface of the catalyst, as suggested by SEM in Figure 4.5. The average crystallite sizes of calcium oxide estimated by Scherrer equation using 2θ equal to 32.2° were 175 nm for NiCa and 233 nm for NiCaNa. These large values are consistent with SEM results and with the SE-SMR which could be an indication that smaller average crystallite size provided more efficiency during the SE-SMR cycles.

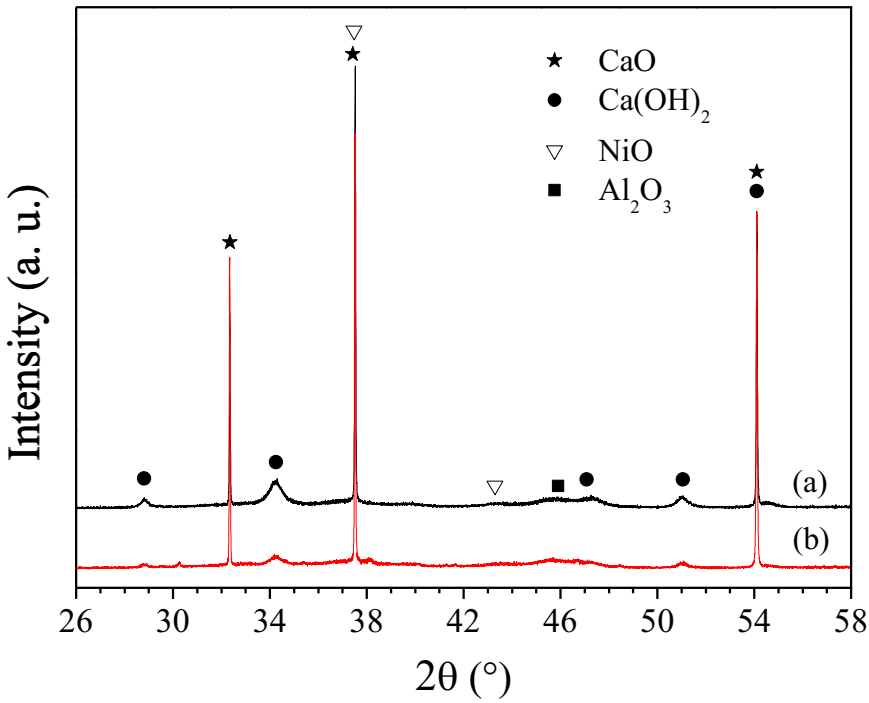

Figure 4.6: X-ray diffraction partners of studied hybrid-materials at room temperature. Legend: (a) NiCa and (b) NiCaNa.

Figure 4.7 shows the diffractograms for NiCa during reduction using a 5% H_2/He mixture at 25 °C, 600 °C, 700 °C, and 800 °C. Figure 4.7 was plotted with a zoom-in the 2θ range from 41 to 53° to monitor the Ni peaks that do not have overlapping with the others. The diffractograms at 25 °C exhibited the peaks at 43.3° [0 2 0] referring to NiO, and 47.3° [0 1 -2] and 51° [2 -1 0] referring to $Ca(OH)_2$ as were previously seen in Figure 4.6. Increasing the temperature, the NiO was reduced to metallic nickel (ICSD 260169) represented by the peaks at 44.5° [1 1 1] and 51.8° [0 2 0]. The peak at 45.9° [0 2 0] associated to γ-Al_2O_3 was also observed at all temperatures (ICSD 30267). The diameter of nickel phase was 5.6 nm which was estimated by the Scherrer equation using the diffractogram at 800 °C and 2θ equal 44.5°. This characteristic low value of particle diameter by metallic nickel species for Ni/Al_2O_3 catalyst is already been reported by the literature.[30] Therefore, it seems plausible to suggest that these particles are well dispersed over the alumina support.

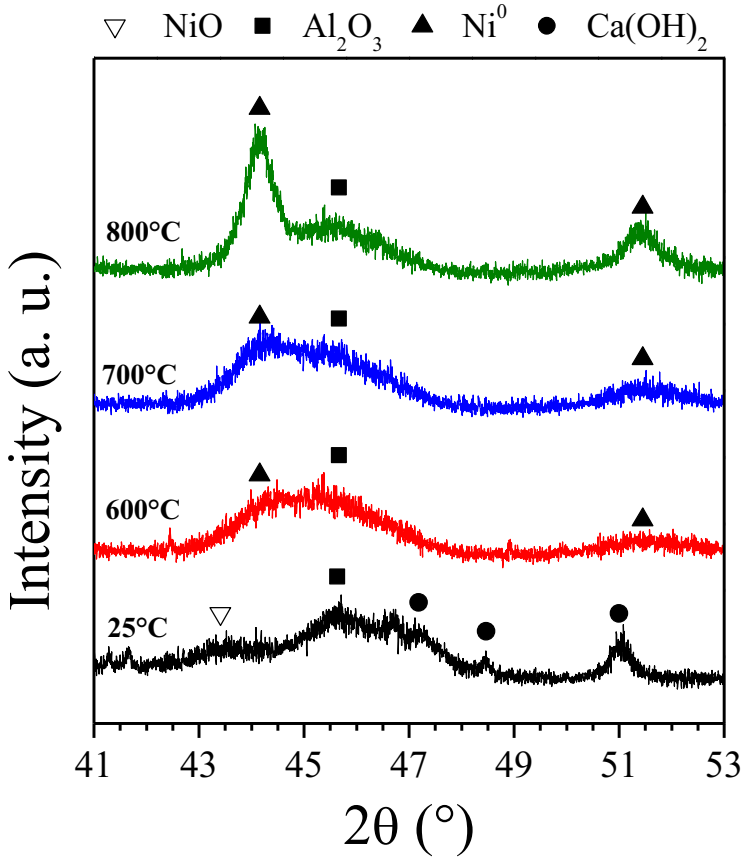

Figure 4.7: *In situ* XRD patterns of NiCa sample during the reduction process under 5% H_2/He flow.

Figure 4.8 shows the X-ray absorption near-edge structure (XANES) Ni K-edge spectra at room temperature (a) and after 1 hour at 800 °C (b). The region of photon energy selected was between 8320 and 8420 eV. At room temperature, all the samples showed one peak at 8352 eV and did not exhibit a pre-edge peak at 8333 eV, which was very similar to the spectrum of NiO foil used as reference.[28, 31] This indicates that the Ni particles were present as Ni^{2+} in the catalysts, which agrees with XRD results. The sample was then heated to 800 °C under a 5% H_2/He mixture causing a progressively decrease in the intensity of the white line at 8352 eV and a detectable pre-edge shoulder, indicating that the Ni^{2+} species were converted into to Ni^0 for all materials. The same observation can be deduced comparing the spectrum obtained at 800 °C of all samples with the metallic nickel reference since both present similar XANES spectrum.[28, 31]

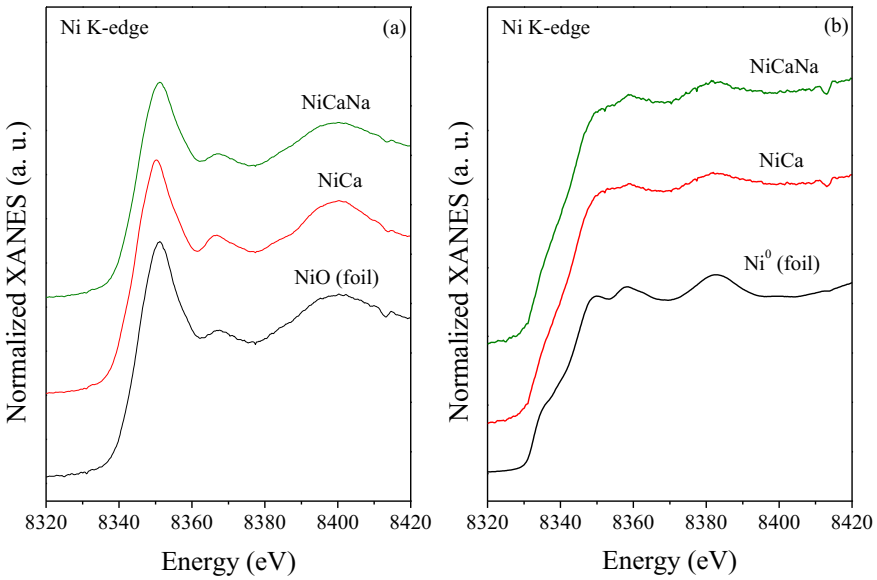

Figure 4.8: Comparison of the snapshots of normalized Ni K-edge XANES spectra (a) at 25 °C and (b) after 1 hour of reduction at 800 °C.

Figure 4.9 exhibits the evolution of XANES spectra as a function of temperature in the left-hand side and the linear combination during the reduction under H_2 atmosphere in the right-hand side. As it can be seen in Figure 4.9, the samples showed a slight difference in the temperature of the initial state of reduction, which in terms of values, it was 382 °C for NiCa and 393 °C for NiCaNa. The linear combination fitting of XANES was done using the NiO and Ni° foil as reference. We can see that all samples were in the oxidized form (NiO) at room temperature. Increasing the temperature up to 800 °C, the fitting data shows that all catalysts changed from the Ni^{2+} species to completely reduced metallic nickel state which remains unchanged after 1 hour under H_2 atmosphere. Another important aspect is about the transition temperature to Ni^{2+} to Ni^0 presented by the catalysts, which was 544 °C for NiCa and 567 °C for NiCaNa. Some studies reported in the literature investigated the influence of sodium promoting Ni/Al_2O_3 catalysts in the reduction process. Zeng and co-workers[27] prepared Ni/Al_2O_3 catalysts promoted by various sodium loading using the solution combustion method. They investigated the role of additives as promoters in the reduction process by the temperature-programmed reduction technique (TPR). Through their results, they showed that Na-modified catalysts exhibited a shift in the reduction peaks of NiO to higher temperatures and associated it with a strong interaction between NiO species and Al_2O_3 support. The same observation was done by Chen and co-workers[32] in their TPR and XPS studies

of Na-Ni/Al_2O_3. They evidenced the reduction peak of NiO was shifted to higher temperature with the increase of Na concentration. According to XPS results obtained by the authors, an accumulation of Na^+ ions on the Ni surface caused a partial coverage of the nickel surface. In our results obtained by XANES Ni K-edge, we observed that the addition of sodium slightly modified the temperature that the reduction process occurs. However, it is not clear the reason and magnitude of the influence of Na in nickel reduction even though it exhibits the same behavior that was reported previously by Zeng and co-workers[27]. The factors that make the results unclear are (i) the sodium is only physical mixed with the metallic phase and (ii) there is not a large difference in the reduction temperature.

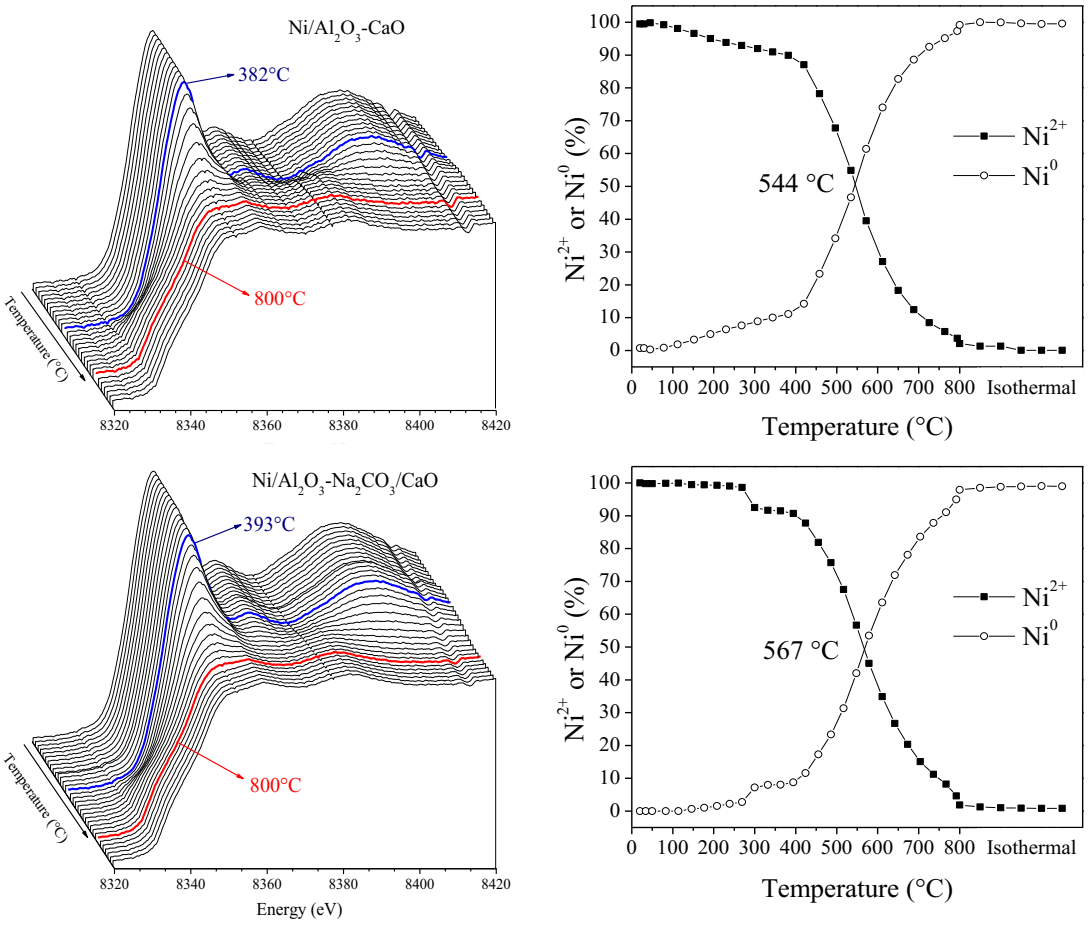

Figure 4.9: Temperature-resolved XANES spectra and linear combination fittings acquired at the Ni K-edge during reduction under a 100 mL/min flow of H_2/He (5 vol.%).

4.3.3 CO_2 sorption capacities

The process of CO_2 sorption in the CaO sorbents was investigated using TGA technique. The carbonatation and calcination/regeneration were carried out at 600 °C and 800 °C under 15% CO_2/He and pure He, respectively. The time adopted for adsorption step was 30 min and 10 min for desorption step. Figure 4.10a and Figure 4.10b show the weight changes of sample (black line) and the temperature change (red line) over 20 cycles.

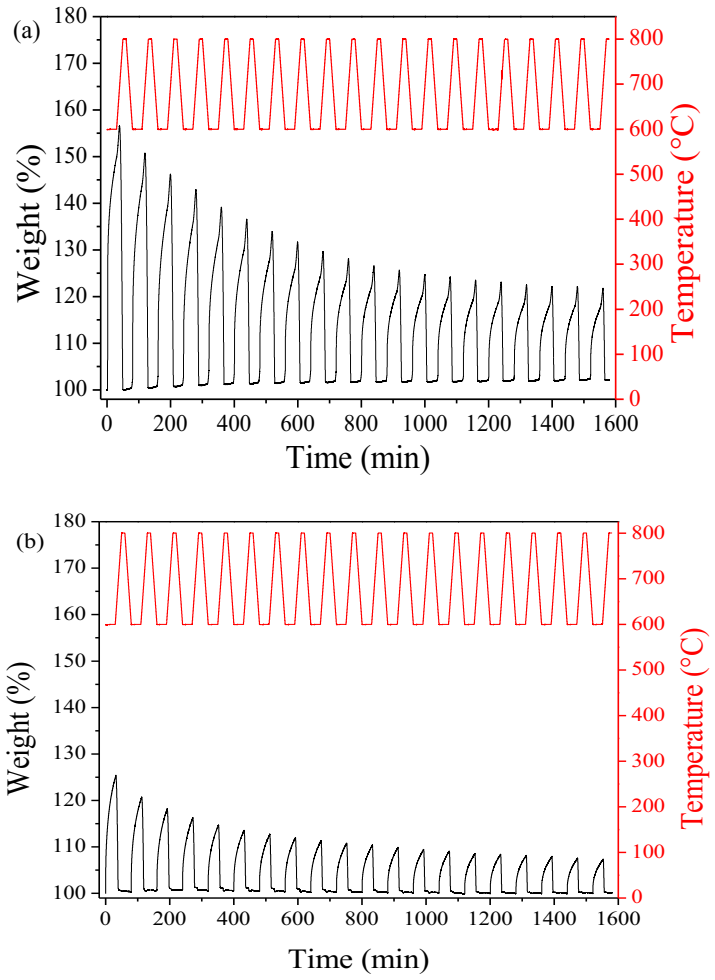

Figure 4.10: Cyclic CO_2 sorption and desorption behavior of (a) CaO sorbent and (b) Na_2CO_3-CaO (sorption at 600 °C under a CO_2 flow for 30 min and desorption at 800 °C under a N_2 flow for 10 min).

The weight variation of CaO was 57 wt.% and 26 wt.% for Na_2CO_3-CaO in the first cycle which represents 14.4 mmol CO_2/g sorbent and 7.2 mmol CO_2/g sorbent, respectively. Both sorbents strongly deactivated during the cycles as we can virtually see in Figure 4.9. To better elucidate sorption capacity and stability, the CO_2 uptake performance of sorbents was plotted in Figure 4.11. The capacity of pure CaO was

0.635 g CO_2/g sorbent which is a bit lower than the theoretical value of CaO (0.785 g CO_2/g CaO). In contrast, the Na promoted-CaO exhibited a very low CO_2 uptake (0.369 g CO_2/g CaO) in the first cycle, which is much lower compared to pure CaO.

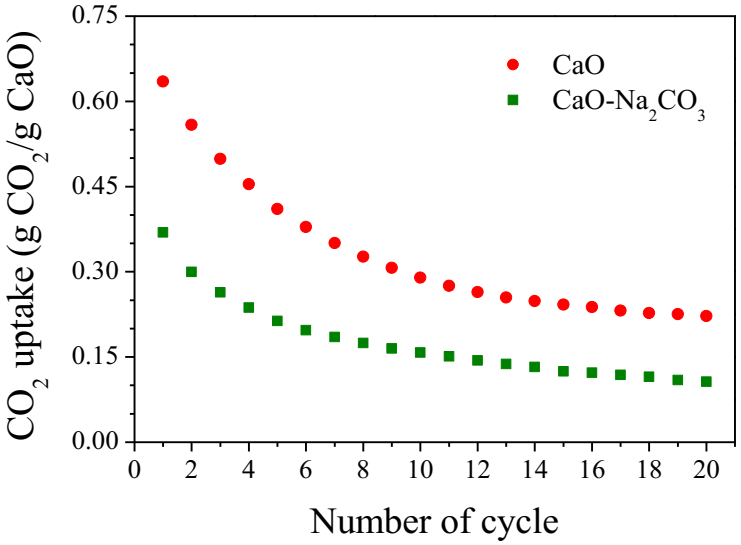

Figure 4.11: Comparison between cyclic CO_2 uptake capacity of CaO and Na_2CO_3-CaO. Conditions: Adsorption under 15 vol.% CO_2 at 600 °C and regeneration under argon at 800 °C.

Many factors can be presented in the sample that led to this poor initial performance and can be correlated to the behavior in SE-SMR. A hypothesis to explain the low CO_2 capacity in the Na-promoted sorbent is based on Biasin et al.[33] work which suggests that there is an inverse relationship between initial/maximum conversion rates and the initial CaO crystallite size. Our XRD results showed that the CaNa sorbent has a higher calcium oxide average crystallite size than pure CaO sorbent. This could be the reason for the low initial CO_2 sorption capacity. Notwithstanding, the SEM analyses showed that the NaCa sample has a "melted" like structure that may have occurred due to a combination of high temperature, a long calcination time (10 hours), and synthesis technique. After 20 cycles, the CO_2 uptake values stabilized in 0.222 g CO_2/g CaO for pure CaO and 0.106 g CO_2/g CaO for CaNa. These values are much lower than initial ones, indicating a strong deactivation over the adsorption cycles for both materials. In the same line to NaCa hypothesis that was previously presented, the large average calcium oxide crystallite sizes of sorbents can be the main

factor that lead to these poor stabilities during the CO_2 sorption experiments. According to Biasin et al.[33], smaller CaO crystallite sizes indicate a larger length of crystallite boundaries per unit of surface area and consequently a larger active specific surface area for the occurring CaO–CO_2 reaction. Thereby, the number of reactive sites is proportional to the length of crystallite boundaries. This would result in an increase in the reaction rate per unit of surface area. Therefore, the larger the average CaO crystallite size is, the higher is the probability of $CaCO_3$ layers to make CaO inactive during the regeneration step. These $CaCO_3$ layers make the access of carbon dioxide to CaO more difficult and thus, the interior of the particle becomes less reactive. Therefore, the limiting step of reaction changes from surface particle reaction to CO_2 diffusion in the $CaCO_3$ layers formed during each cycle of carbonation/regeneration. In our case, the synthesis conditions of the sodium doped material did not provide physical characteristics like small average calcium oxide crystallite size, which could have improved CO_2 capacity performance and the stability of material over calcination/carbonation cycles.

The adsorption kinetics were estimated using the double exponential model which is an important fitting method to extract the rate constants as applied in the work of Yoon et al.[34] and Guo et al.[35]. Figure 4.12 illustrates the TGA experimental data and fitted with the exponential double model for 1st and 20th cycle of both sorbents, and the corresponding fitted kinetic parameters are listed in Table 4.2. The double-exponential model (eq. 4.7) was applied to investigate the CO_2 sorption kinetics of Ca-based sorbents.

$$y = Ae^{-k_1 t} + Be^{-k_2 t} + C \qquad \text{Eq. 4.7}$$

where y represents the weight percentage of CO_2 captured, A, B, and C are the pre-exponential factors, and k_1 and k_2 are the exponential constants and t is the reaction time. Two-step of the CO_2 capture mechanism could be described by the double-exponential model where the chemisorption step and CO_2 diffusion step are represented by k_1 and k_2, respectively. The term C corresponds to the maximum CO_2 capture capacity. The correlation parameters (R^2) were higher than 0.99 which indicated a good correlation regression. At the 1st cycle, k_1 values (0.0310 – 0.0110 s^{-1}) of all samples was orders of magnitude higher than k_2 values (0.0008 – 0.0005 s^{-1}), indicating that the kinetically limiting step is the CO_2 diffusion through of the $CaCO_3$

layer formed by CaO. After twenty cycles, k_2 values (0.0142 – 0.0497 s^{-1}) become higher than k_1 values (0.0004 – 0.0008 s^{-1}) suggesting that the surface reaction controls the reaction rate resulting in a lower adsorption capacity as it can been seen in Figure 4.12. Therefore, if the k_1/k_2 ratio is greater than 1, it indicates that the diffusion of CO_2 is the rate-determining step. On the contrary, if the k_1/k_2 far less than 1, reveals the predominance of the surface reaction in total adsorption process which occurs due to the sintering of CaO particles and, consequently, decreasing in the active calcium sites on the surface.[35]

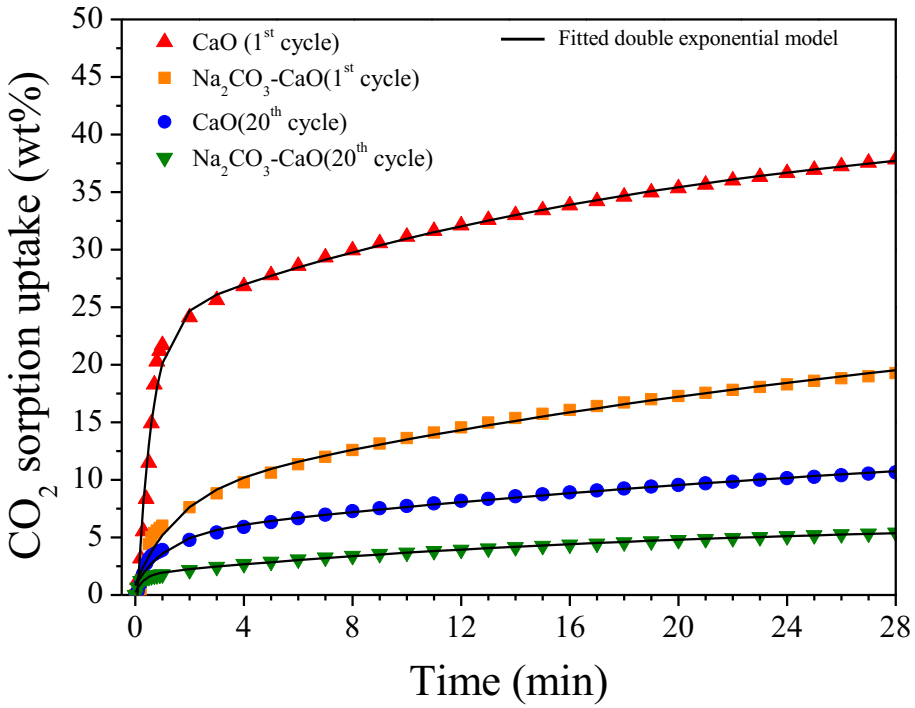

Figure 4.12: Experimental data and model fitting of synthesized sorbents at 600 °C for 1st and 20th cycles of CO_2 adsorption.

Table 4.2: Kinetics parameters of Ca-based sorbents estimated by double-exponential model.

	A	**B**	**C**	**k_1**	**k_2**	**k_1/k_2**	**R^2**
CaO(1st)	-27.68	-18.81	42.42	0.0310	0.0008	38.75	0.9949
Na_2CO_3-CaO (1st)	-7.68	-19.99	28.58	0.0110	0.0005	22	0.9985
CaO (20th)	-10.95	-4.37	16.14	0.0004	0.0142	0.028	0.9977
Na_2CO_3-CaO (20th)	-4.71	-1.57	6.51	0.0008	0.0497	0.016	0.9980

Therefore, the TGA experimental data and the kinetic analyses clearly explained the poor stability and low CO_2 capture uptake for the sodium-containing sample verified during SE-SMR experiments. Also, the SEM images revealed a solid and compact structure which strongly influenced this performance. Thus, these carbonation/calcination results were different that was expected based on literature explanation about the effects of double-salt materials. Recently, the limitation of sorption kinetics of metal oxide-based sorbent (e.g. CaO and MgO) was overcome by the doping of alkali metal components.[17, 36-38] Notably, molten salts were reported to have good oxygen mobility and CO_2 diffusion at above their melting point. These effects lead to a stable sorption uptake and fast sorption kinetics in the sorbents. Based on literature[18, 39, 40], Lee and co-workers[17] reported a theoretical model for CO_2 sorption mechanism concerning double salt formation based on the reaction of metal oxide and alkali-metal carbonate with CO_2. According to the authors, the changes in the carbonation reaction pathway of the sorbent provoked by the addition of Na_2CO_3 (double salt formation – $Na_2Ca(CO_3)_2$) can lead easy regeneration at 800 °C under N_2 flow and consequently good cyclic stability. However, in our work, we did not evidence the benefits of a possible formation of the double-salt $Na_2Ca(CO_3)_2$ in the carbonation step during the SE-SMR. Thus, the difficulty to control the amount of Na_2CO_3 (high solubility in water – 215g/L) retained in the filter cake after the synthesis step and the choice precursor used for double-salt preparation could be limiting factors of this approach requiring more investigation and developing. Therefore, the precipitation method proved to be a sensitive technique that affected directly the morphology of the material and, consequently, the performance in sorption enhanced steam methane reforming.

4.4 Conclusions

The influence of sodium doping in the CaO sorbent and the application in sorption enhanced steam methane reforming (SE-SMR) were evaluated in this work. The sorbent Na_2CO_3-CaO was prepared by precipitation method and compared with CaO. For SE-SMR experiments, the catalyst consisted of a physical mixing of sorbent and Ni/Al_2O_3 prepared by the impregnation method. For these samples, the CH_4 conversion of all cycles was 100% indicating a mass transfer regime and the H_2 molar fraction was approximately 93.5 vol.% during the pre-breakthrough period. Although

the sodium addition proved an increase in the surface area, the sorbent containing sodium presented poor stability and low CO_2 capture capacity compared with pure CaO over the SE-SMR cycles. Furthermore, *in situ* XANES data revealed a slightly increase in the reduction temperature of nickel particles in the Na-containing sample. Also, the large average crystallite size of calcium oxide of both sorbents led to a low CO_2 uptake capture and poor stability as showed in the CO_2 sorption experiments. Therefore, the inverse relationship of average crystallite size and sorbent stability was evidenced for both materials. Specifically, the poorer performance presented by Na_2CO_3-CaO was associated with strong sintering phenomenon caused by the sodium addition and the synthesis conditions such as temperature and calcination time, the use of $Ca(NO_3)_2$ as the precursor, and a difficult control in the sodium amount in the cake filtered in the precipitation method.

4.5 References

1. García-Lario, A. L.; Grasa, G. S.; Murillo, R., Performance of a combined CaO-based sorbent and catalyst on H_2 production, via sorption enhanced methane steam reforming. *Chemical Engineering Journal* **2015,** *264*, 697-705. https://doi.org/10.1016/j.cej.2014.11.116
2. Lee, C. H.; Lee, K. B., Sorption-enhanced water gas shift reaction for high-purity hydrogen production: Application of a Na-Mg double salt-based sorbent and the divided section packing concept. *Applied Energy* **2017,** *205*, 316-322. https://doi.org/10.1016/j.apenergy.2017.07.119
3. Chanburanasiri, N.; Ribeiro, A. M.; Rodrigues, A. E.; Arpornwichanop, A.; Laosiripojana, N.; Praserthdam, P.; Assabumrungrat, S., Hydrogen production via sorption enhanced steam methane reforming process using Ni/CaO multifunctional catalyst. *Industrial & Engineering Chemistry Research* **2011,** *50* (24), 13662-13671. https://doi.org/10.1021/ie201226j
4. Feng, H. Z.; Lan, P. Q.; Wu, S. F., A study on the stability of a NiO–CaO/Al_2O_3 complex catalyst by La_2O_3 modification for hydrogen production. *International Journal of Hydrogen Energy* **2012,** *37* (19), 14161-14166. https://doi.org/10.1016/j.ijhydene.2012.06.099
5. Harrison, D. P., Sorption-enhanced hydrogen production: a review. *Industrial & Engineering Chemistry Research* **2008,** *47* (17), 6486-6501. https://doi.org/10.1021/ie800298z
6. Hu, R.; Li, D.; Xue, H.; Zhang, N.; Liu, Z.; Liu, Z., Hydrogen production by sorption-enhanced steam reforming of acetic acid over Ni/$Ce_xZr_{1-x}O_2$-CaO catalysts. *International Journal of Hydrogen Energy* **2017,** *42* (12), 7786-7797. https://doi.org/10.1016/j.ijhydene.2017.01.167
7. Rostrup-Nielsen, J. R.; Sehested, J.; Nørskov, J. K., Hydrogen and synthesis gas by steam- and CO_2 reforming. In *Advances in Catalysis*, Academic Press: 2002; Vol. 47, pp 65-139.
8. Carvill, B. T.; Hufton, J. R.; Anand, M.; Sircar, S., Sorption-enhanced reaction process. *AIChE Journal* **1996,** *42* (10), 2765-2772. https://doi.org/10.1002/aic.690421008

9. Barelli, L.; Bidini, G.; Gallorini, F.; Servili, S., Hydrogen production through sorption-enhanced steam methane reforming and membrane technology: a review. *Energy* **2008,** *33* (4), 554-570. https://doi.org/10.1016/j.energy.2007.10.018
10. Radfarnia, H. R.; Sayari, A., A highly efficient CaO-based CO_2 sorbent prepared by a citrate-assisted sol–gel technique. *Chemical Engineering Journal* **2015,** *262*, 913-920. https://doi.org/10.1016/j.cej.2014.09.074
11. Shokrollahi Yancheshmeh, M.; Radfarnia, H. R.; Iliuta, M. C., High temperature CO_2 sorbents and their application for hydrogen production by sorption enhanced steam reforming process. *Chemical Engineering Journal* **2016,** *283*, 420-444. https://doi.org/10.1016/j.cej.2015.06.060
12. Radfarnia, H. R.; Iliuta, M. C., Hydrogen production by sorption-enhanced steam methane reforming process using CaO-Zr/Ni bifunctional sorbent–catalyst. *Chemical Engineering and Processing: Process Intensification* **2014,** *86*, 96-103. https://doi.org/10.1016/j.cep.2014.10.014
13. Choi, S.; Drese, J. H.; Jones, C. W., Adsorbent materials for carbon dioxide capture from large anthropogenic point sources. *ChemSusChem* **2009,** *2* (9), 796-854. https://doi.org/10.1002/cssc.200900036
14. Shokrollahi Yancheshmeh, M.; Radfarnia, H. R.; Iliuta, M. C., Sustainable production of high-purity hydrogen by sorption enhanced steam reforming of glycerol over CeO_2-promoted $Ca_9Al_6O_{18}$–CaO/NiO bifunctional material. *ACS Sustainable Chemistry & Engineering* **2017,** *5* (11), 9774-9786. https://doi.org/10.1021/acssuschemeng.7b01627
15. Naeem, M. A.; Armutlulu, A.; Imtiaz, Q.; Donat, F.; Schaublin, R.; Kierzkowska, A.; Muller, C. R., Optimization of the structural characteristics of CaO and its effective stabilization yield high-capacity CO_2 sorbents. *Nat Commun* **2018,** *9* (1), 2408. https://doi.org/10.1038/s41467-018-04794-5
16. Al-Mamoori, A.; Thakkar, H.; Li, X.; Rownaghi, A. A.; Rezaei, F., Development of potassium- and sodium-promoted CaO adsorbents for CO_2 capture at high temperatures. *Industrial & Engineering Chemistry Research* **2017,** *56* (29), 8292-8300. https://doi.org/10.1021/acs.iecr.7b01587
17. Lee, C. H.; Choi, S. W.; Yoon, H. J.; Kwon, H. J.; Lee, H. C.; Jeon, S. G.; Lee, K. B., Na_2CO_3-doped CaO-based high-temperature CO_2 sorbent and its sorption kinetics. *Chemical Engineering Journal* **2018,** *352*, 103-109. https://doi.org/10.1016/j.cej.2018.06.141
18. Lee, C. H.; Mun, S.; Lee, K. B., Characteristics of Na–Mg double salt for high-temperature CO_2 sorption. *Chemical Engineering Journal* **2014,** *258*, 367-373. https://doi.org/10.1016/j.cej.2014.07.082
19. Zhang, K.; Li, X. S.; Duan, Y.; King, D. L.; Singh, P.; Li, L., Roles of double salt formation and $NaNO_3$ in Na_2CO_3-promoted MgO absorbent for intermediate temperature CO_2 removal. *International Journal of Greenhouse Gas Control* **2013,** *12*, 351-358. https://doi.org/10.1016/j.ijggc.2012.11.013
20. Liu, L.; Hong, D.; Guo, X., A study of metals promoted CaO-based CO_2 sorbents for high temperature application by combining experimental and DFT calculations. *Journal of CO_2 Utilization* **2017,** *22*, 155-163. https://doi.org/10.1016/j.jcou.2017.09.022
21. Salaudeen, S. A.; Acharya, B.; Dutta, A., CaO-based CO_2 sorbents: a review on screening, enhancement, cyclic stability, regeneration and kinetics modelling. *Journal of CO_2 Utilization* **2018,** *23*, 179-199. https://doi.org/10.1016/j.jcou.2017.11.012
22. Dong, J.; Tang, Y.; Nzihou, A.; Weiss-Hortala, E., Effect of steam addition during carbonation, calcination or hydration on re-activation of CaO sorbent for CO_2 capture. *Journal of CO_2 Utilization* **2020,** *39*, 101167. https://doi.org/10.1016/j.jcou.2020.101167
23. Xie, M.; Zhou, Z.; Qi, Y.; Cheng, Z.; Yuan, W., Sorption-enhanced steam methane reforming by *in situ* CO_2 capture on a CaO–$Ca_9Al_6O_{18}$ sorbent. *Chemical Engineering Journal* **2012,** *207-208*, 142-150. https://doi.org/10.1016/j.cej.2012.06.032
24. Sultana, K. S.; Chen, D., Enhanced hydrogen production by *in situ* CO_2 removal on $CaCeZrO_x$ nanocrystals. *Catalysis Today* **2011,** *171* (1), 43-51. https://doi.org/10.1016/j.cattod.2011.04.019

25. Radfarnia, H. R.; Iliuta, M. C., Development of zirconium-stabilized calcium oxide absorbent for cyclic high-temperature CO_2 capture. *Industrial & Engineering Chemistry Research* **2012,** *51* (31), 10390-10398. https://doi.org/10.1021/ie301287k
26. López, J. M.; Grasa, G.; Murillo, R., Evaluation of the effect of inert support on the carbonation reaction of synthetic CaO-based CO_2 sorbents. *Chemical Engineering Journal* **2018,** *350*, 559-572. https://doi.org/10.1016/j.cej.2018.05.014
27. Zeng, Y.; Ma, H.; Zhang, H.; Ying, W., Na promoted Ni/γ-Al_2O_3 catalysts prepared by solution combustion method for syngas methanation. *International Journal of Chemical and Molecular Engineering* **2014,** *8* (7), 649-653. https://doi.org/10.5281/zenodo.1093736
28. Andonova, S.; de Ávila, C. N.; Arishtirova, K.; Bueno, J. M. C.; Damyanova, S., Structure and redox properties of Co promoted Ni/Al_2O_3 catalysts for oxidative steam reforming of ethanol. *Applied Catalysis B: Environmental* **2011,** *105* (3-4), 346-360. https://doi.org/10.1016/j.apcatb.2011.04.029
29. Sehested, J.; Gelten, J. A. P.; Helveg, S., Sintering of nickel catalysts: effects of time, atmosphere, temperature, nickel-carrier interactions, and dopants. *Applied Catalysis A: General* **2006,** *309* (2), 237-246. https://doi.org/10.1016/j.apcata.2006.05.017
30. Zhang, J.; Xu, H.; Jin, X.; Ge, Q.; Li, W., Characterizations and activities of the nano-sized Ni/Al_2O_3 and Ni/La–Al_2O_3 catalysts for NH_3 decomposition. *Applied Catalysis A: General* **2005,** *290* (1-2), 87-96. https://doi.org/10.1016/j.apcata.2005.05.020
31. Anjaneyulu, C.; Costa, L. O. O. d.; Ribeiro, M. C.; Rabelo-Neto, R. C.; Mattos, L. V.; Venugopal, A.; Noronha, F. B., Effect of Zn addition on the performance of Ni/Al_2O_3 catalyst for steam reforming of ethanol. *Applied Catalysis A: General* **2016,** *519*, 85-98. https://doi.org/10.1016/j.apcata.2016.03.008
32. Chen, C. S.; You, J. H.; Lin, C. C., Carbon nanofibers synthesized from carbon dioxide by catalytic hydrogenation on Ni−Na/Al_2O_3 catalysts. *The Journal of Physical Chemistry C* **2011,** *115* (5), 1464-1473. https://doi.org/10.1021/jp107730r
33. Biasin, A.; Segre, C. U.; Salviulo, G.; Zorzi, F.; Strumendo, M., Investigation of CaO–CO_2 reaction kinetics by in-situ XRD using synchrotron radiation. *Chemical Engineering Science* **2015,** *127*, 13-24. https://doi.org/10.1016/j.ces.2014.12.058
34. Yoon, H. J.; Lee, K. B., Introduction of chemically bonded zirconium oxide in CaO-based high-temperature CO_2 sorbents for enhanced cyclic sorption. *Chemical Engineering Journal* **2019,** *355*, 850-857. https://doi.org/10.1016/j.cej.2018.08.148
35. Guo, H.; Feng, J.; Zhao, Y.; Wang, S.; Ma, X., Effect of micro-structure and oxygen vacancy on the stability of (Zr-Ce)-additive CaO-based sorbent in CO_2 adsorption. *Journal of CO_2 Utilization* **2017,** *19*, 165-176. https://doi.org/10.1016/j.jcou.2017.03.015
36. Jin, S.; Ho, K.; Lee, C.-H., Facile synthesis of hierarchically porous MgO sorbent doped with $CaCO_3$ for fast CO_2 capture in rapid intermediate temperature swing sorption. *Chemical Engineering Journal* **2018,** *334*, 1605-1613. https://doi.org/10.1016/j.cej.2017.11.095
37. Huang, L.; Zhang, Y.; Gao, W.; Harada, T.; Qin, Q.; Zheng, Q.; Hatton, T. A.; Wang, Q., Alkali carbonate molten salt coated calcium oxide with highly improved carbon dioxide capture capacity. *Energy Technology* **2017,** *5* (8), 1328-1336. https://doi.org/10.1002/ente.201600628
38. Zhang, K.; Li, X. S.; Chen, H.; Singh, P.; King, D. L., Molten salt promoting effect in double salt CO_2 absorbents. *The Journal of Physical Chemistry C* **2015,** *120* (2), 1089-1096. https://doi.org/10.1021/acs.jpcc.5b10729
39. Bhatia, S.; Perlmutter, D., Effect of the product layer on the kinetics of the CO_2-lime reaction. *AIChE Journal* **1983,** *29* (1), 79-86. https://doi.org/10.1002/aic.690290111
40. Wu, S. F.; Lan, P. Q., A kinetic model of nano-CaO reactions with CO_2 in a sorption complex catalyst. *AIChE Journal* **2012,** *58* (5), 1570-1577. https://doi.org/10.1002/aic.12675

Chapter 5 - Understanding the high CO selectivity of intermetallic alloy Ni-In/SiO_2 for the reverse water gas shift reaction

5.1 Introduction

The concern about the anthropogenic CO_2 emissions has been increasing and worsening in such way that forceful actions will be necessary. Climate changes and ocean acidification are some consequences of the increase in CO_2 emission that can cause catastrophic damages.[1, 2] Hence, researchers have made efforts to develop technologies to capture and use CO_2 as a raw material to synthesize value-added chemicals containing two or more carbons, including dimethyl ether, olefins, liquid fuels, and higher alcohols.[3]

In this scenario, the large-scale conversion of CO_2 to CO, also known as reverse water gas shift reaction (rWGS), has attracted particular attention as a process for CO_2 utilization.[4] The rWGS reaction is an endothermic process, which requires a high temperature and a high CO selectivity catalyst. The produced CO is an important precursor molecule that can be used in the methanol synthesis and downstream Fisher-Tropsch, which brings advantages such as high flexibility and feasibility to the rWGS reaction. However, a highly selective catalyst to CO has be used to avoid side reactions such as the methanation reaction. Indeed, some common catalysts used in this reaction are Cu-based, Ni-based, noble metals, and these metals supported on ceria.[5] Nevertheless, Ni is well known as a good catalyst for methanation and Cu suffers from the sintering which makes them as drawbacks for the CO formation and catalytic activity/stability, respectively. As a consequence, some strategies have been investigated to enhance both CO_2 conversion and the selectivity towards CO, including varying the support, adding alkali metals and/or reducible promoters, optimizing metal/oxide interface, and forming bimetallic alloys.[6, 7]

Specifically, these bimetallic catalysts have been shown as excellent candidates for many applications since they may exhibit unique structure/electronic features that can enhance molecular transformations. These characteristics result from the addition of a second metal that provides a specific atomic random arrangement, which could be a disordered (solid solutions) or an ordered structure known as intermetallic compounds.

For instance, the addition of indium to Ni/SiO_2 catalyst was investigated for dry reforming of methane. Suppression of the formation of multiple bonded carbon species and decrease of the CO adsorption on nickel were observed in the $Ni-In/SiO_2$ catalyst due to the dilution of the nickel surface provided by indium atoms.[8] In this way, the bimetallic catalyst hindered the coke formation during the dry reforming of methane (DRM), which was a result of the new intermetallic structure formed with different geometric and electronic features compared to the parent metals. Studt et al.[9] also reported some benefits of using a new intermetallic Ni-Ga catalyst for CO_2 hydrogenation to methanol. The Ni-Ga catalyst exhibited higher activity than the commercial $Cu/ZnO/Al_2O_3$ catalyst at atmospheric pressure. The presence of Ga rich-sites in the intermetallic catalyst allowed the formation of CH_3OH, turning the Ni catalysts, known as a CO_2 methanation catalyst, into an excellent candidate for methanol synthesis.

In another study, Liu et al.[10] investigated the chemical and electronic specifications of Pt-Ni bimetallic catalysts and their interaction with the mesoporous silica support, providing a quantitative characterization during the rWGS reaction. The high activity and selectivity of the intermetallic nanoparticles were attributed to the structural impact of the strong metal-silica bonding interactions that mitigates the formation of alloy phases containing Ni-Ni ensembles. According to them, only heterometallic Pt-Ni interactions are present in the surface, displaying an atomic arrangement that led to an exceptional activity and selectivity towards CO. Recently, Snider et al.[11] investigated Pd-In and Ni-In supported on SiO_2 for CO_2 hydrogenation to methanol. Their results revealed that the In_2O_3 phase and the Pd-In intermetallic compound have a synergetic effect that enhanced the activity and selectivity to methanol. All Pd-In catalysts showed a better methanol formation activity compared to monometallic Pd and indium oxide, with the $Pd:In(1:2)/SiO_2$ as the best catalyst. Similar effects were also observed for the Ni-In catalyst, this being an alternative to the $Pd-In/SiO_2$ as a precious metal-free catalyst. Moreover, the CH_4 selectivity was less than 1%, which evidences a suppression of the methanation reaction in both Ni-In and Pd-In compounds. Although Ni-In catalyst has shown good activity in the methanol production, it is not clear how the intermetallic Ni-In catalysts work. In addition, the catalytic performance of a Ni-In catalyst for the rWGS, which is a key intermediate step for CO_2 hydrogenation processes, was not investigated.

Here, we synthesized Ni-In/SiO_2 catalysts by hydrothermal synthesis and tested for the rWGS reaction for different feed compositions. Different ordered and disordered alloy phases were obtained and identified by *in situ* XRD. Additionally, the catalytic performance of the bimetallic Ni-In catalyst was compared with pure Ni/SiO_2. A high selectivity towards CO was achieved by allowing both metals, although the activity decreased with higher In content. Combined *in situ* XAS-XRD and CO-DRIFTS allowed us to understand the structural changes and the electronic effects caused by the indium addition and how they influence the activity and CO/CH_4 selectivity of the rWGS reaction.

5.2 Experimental section

5.2.1 Materials

$Ni(NO_3)_2.6H_2O$ (99.9%, Sigma-Aldrich), $In(NO_3)_3$*$3.7H_2O$ (99.9%, Sigma-Aldrich), urea (99.5%), and LUDOX® TM-50 colloidal silica (50 wt.% suspension in H_2O) were purchased from Sigma-Aldrich.

5.2.2 Catalyst synthesis

The monometallic Ni/SiO_2 and bimetallic Ni-In/SiO_2 catalyst were synthesized by modified hydrothermal approach.[12] 2 g of urea and the appropriate amount of $Ni(NO_3)_2.6H_2O$ and $In(NO_3)_3$*$3.7H_2O$ were dissolved completely in 40 mL of distilled water at room temperature. Subsequently, the homogenous solution was mixed with 1 g of colloidal SiO_2 stirring well and transferred to a Teflon-lined stainless-steel autoclave. The autoclave was kept in an oven at 100 °C for 12h. After cooling down to room temperature, the resulting slurry was transferred to a falcon tube, washed thoroughly with distilled water, and centrifuged for 5 min using 6000 rpm. The washing process was performed three times. The materials were dried in an oven at 120 °C for 12h. Thereafter, the catalysts were sifted using the sieve of 80 mesh and reduced at 800 °C for 4 hours under 10% H_2/N_2 (total flow = 100 mL/min). The synthesized catalysts were Ni/SiO_2, $Ni_{0.85}In_{0.15}/SiO_2$, $Ni_{0.50}In_{0.50}/SiO_2$. Furthermore,

5wt.% In_2O_3/SiO_2 catalyst was also synthesized and calcined at 600 °C for 1 h to be used as reference.

5.2.3 Materials characterization

The elemental analysis of the catalysts was performed by Inductively Coupled Plasma - Optical Emission Spectroscopic (ICP-OES - Agilent 5100 VDV).

Combined *in situ* XAS and XRD measurements were performed at the Swiss-Norwegian beamlines (SNBL, BM31) at the European Synchrotron Radiation Facility (ESRF), Grenoble, France. XAS spectra were collected at the Ni K-edge and In K-edge using a Si (111) double crystal monochromator in transmission mode with a step size of 0.5 eV in a continuous scanning between 8200 – 8960 eV and 27800 – 28700 eV, respectively. XRD data were collected with a 2D DEXELA detector using a Si (111) channel-cut monochromator, set at a wavelength of 0.337 Å. 6 mg of catalyst was placed between two plugs of quartz wool resulting in 1 cm bed length in a quartz capillary reactor cell of 1.5 mm outer diameter and 0.02 mm wall thickness. Averaging procedures and azimuthal integration were performed with the pyFAI software using NIST LaB_6 powder as a standard. Schematics of the experimental methodology is plotted in Figure 5.1.

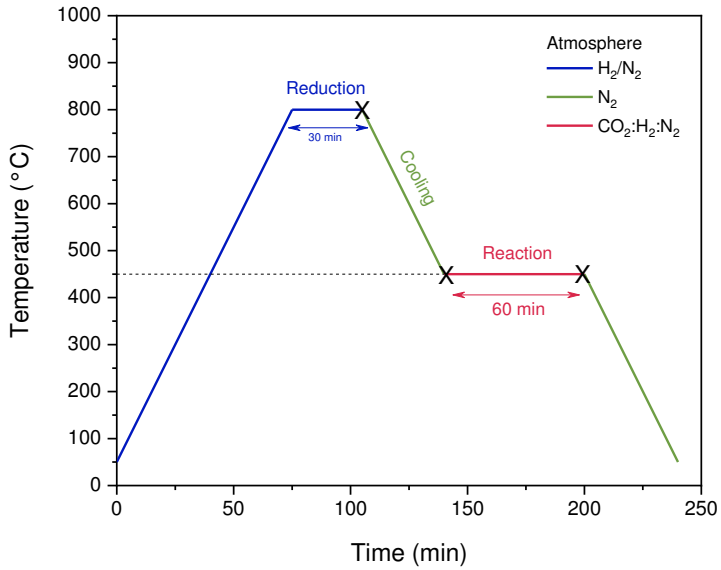

Figure 5.1: Schematic of the *in situ* XRD-XAS experiments. The crosses indicated the selected data plotted in the XRD-XAS results.

The alternating XAS-XRD cycles utilized the following steps: (i) activation of the catalyst by heating to 800 °C using an air blower (previously calibrated) in 5% H_2/He (1 bar, 10 mL/min) and holding for 30 min at 800 °C, (ii) cooling down to 450 °C (rate of 10 °C/min) under pure He (iii) switching to rWGS reaction conditions (450 °C, 1 bar, 3 mL/min of CO_2, 6 mL/min of H_2, and 3 mL/min of N_2, GHSV = 120000 mL g^{-1}_{cat} h^{-1}) for 1 hour, and then (iv) cooling down to room temperature under N_2 (CO_2 valve closed to avoid any leaking and, consequently oxidation of the catalyst).

The spectra of pellets of NiO, Ni^0, and synthetized In_2O_3/SiO_2 were collected at room temperature, to be used as a reference for Ni^{2+}, Ni^0, and In^{3+}, respectively. The processing of the XAS data was normalized using the Athena software of the Demeter package (version 0.9.26).[13] XRD patterns of the catalysts were refined by the Rietveld method using the FullProf software package. The refinements were carried out using a wavelength of 0.337 Å and atomic positions following previously published crystal structures. In order to correct instrumental line broadening, an instrumental resolution file was created by profile fitting of a LaB_6 standard (NIST).[14, 15] The background was defined by linear interpolation between the background point with the heights that will be refined.

Scanning Transmission Electron Microscopy (STEM) measurements were performed using a FEI Talos F200X transmission electron microscope equipped with four SDD detectors and operated at 200 kV. The energy-dispersive X-ray spectroscopy (EDX) was obtained with a Super-X EDS system (windowless, shutter protected)

Diffuse Reflectance Infrared Fourier Transform Spectroscopy of adsorbed CO (CO-DRIFTS) was performed on a Nicolet 6700 FT-IR spectrometer (ThermoFisher Scientific) equipped with a high-temperature cell (Harrick) and liquid-nitrogen-cooled MCT detector. Before the CO adsorption, the samples were pretreated in a 5% H_2/N_2 mixture at 800 °C for 1 hour, followed by purging with nitrogen at the same temperature to remove the residual H_2. Thus, the background spectra were collected after cooling down to room temperature. Spectra were acquired at room temperature under 1.7% CO/He flow (total flow = 30 mL/min) using 128 scans at optical resolution of 4 cm^{-1}.

5.2.4 Catalyst test

The reverse water gas shift reaction (rWGS) was carried out in a fixed-bed quartz reactor (400 mm length, 12.6 mm internal diameter) at 450 °C and 1 bar. Approximately, 20 mg of the pre-reduced catalyst was mixed with 400 mg of SiC to guarantee the isothermal zone of the catalytic bed. The material was loaded into the reactor and, prior to the catalytic tests, was pre-reduced at 800 °C for 1 h using 10% of H_2/N_2 mixture. After that, the reactor was cooled down to the reaction temperature under N_2. Then, the feed gas was introduced in a total flow of 40 mL/min (GHSV = 120000 mL g^{-1}_{cat} h^{-1}). Several gas compositions were tested varying from CO_2:H_2:N_2 = 1:2:1 to CO_2:H_2:N_2 = 1:5:1. The composition of the effluent gas was analyzed using a GC (PerkinElmer Clarus 580) equipped with thermal conductivity and flame ionization detectors . The selectivity (S_i), and formation/consumption rate (r_i) were determined using the following equations:

$$S_i(\%) = \frac{F_{i,out}}{F_{i,out}+F_{j,out}} \times 100 \qquad \text{Eq. 5.1}$$

$$r_{CO_2} = \frac{F_{CO2,in}(mL\ min^{-1}) - F_{CO2,out}\ (mL\ min^{-1})}{24465\ (mL\ mol^{-1}) \times w_{cat}(g)} \qquad \text{Eq. 5.2}$$

$$r_{CO} = \frac{F_{out}(mL\ min^{-1}) \times y_{co}}{24465\ (mL\ mol^{-1}) \times w_{cat}(g)} \qquad \text{Eq. 5.3}$$

where F_i and F_j are the flow in the reactor outlet of products i and j, respectively. F_{out} represents the total flow in the reactor outlet, w_{cat} is the amount of catalyst, and y_{CO} corresponds to the mole fraction of CO in the products. The parameter used is the molar volume of a gas at room temperature and atmospheric pressure (24450 mL mol^{-1}). For each condition, 7 measurements were performed. The data reported correspond to the average of 5 points, since the first and last measurement of each condition were discarded.

5.3 Results and discussion

5.3.1 Characterization of the morphology and composition of the catalyst

The metal loading of the synthesized materials was measured by ICP-OES to confirm the Ni:In molar ratio supported on silica in the fresh and reduced catalyst as shown in Table 5.1.

Table 5.1: Elemental composition of the fresh and reduced catalysts measured by ICP-OES.

Sample		Nominal weight (wt.%)	Metal loading (ICP, wt.%)		In/(Ni+In)		
					Nominal	Measured	
			Fresh	Reduced		Fresh	Reduced
Ni/SiO_2	Ni	5	4.62	5.15	-	-	-
	In	0	0	0			
$Ni_{0.85}In_{0.15}/SiO_2$	Ni	3.71	3.57	3.83	0.15	0.16	0.16
	In	1.29	1.34	1.51			
$Ni_{0.50}In_{0.50}/SiO_2$	Ni	1.7	1.82	1.61	0.50	0.49	0.41
	In	3.3	3.50	2.19			

All the fresh catalysts showed a small deviation after the synthesis that could be related to the washing step, in which some metal could be drawn with the water. Nevertheless, the hydrothermal technique has been shown feasible to produce compounds with a minimum loss of materials.[16] After the reduction step at 800 °C, the $Ni_{0.50}In_{0.50}/SiO_2$ catalyst exhibited a slight deficit in the indium content, indicating that part of the metal may have volatilized with the increase of the temperature since its melting point is low (156.6 °C).[17] This means that the phase composition was altered and, consequently, a different phase was produced as can be observed in Figure 5.2. However, in this work, the nominal loading will be adopted as nomenclature to reference the catalysts.

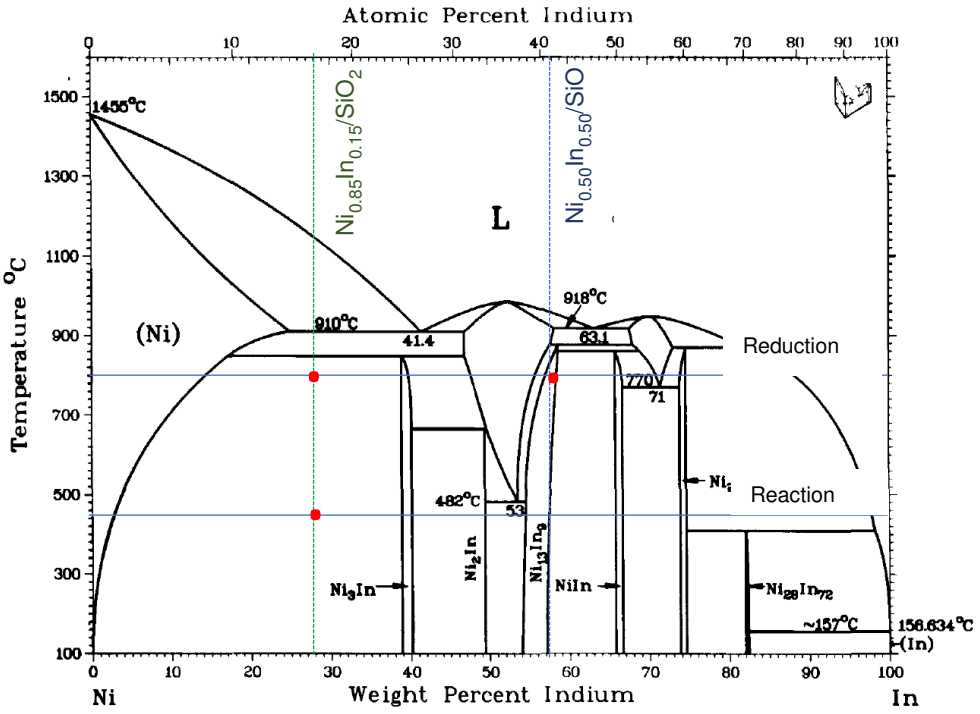

Figure 5.2: Diagram phase of Ni-In. Red dots indicate the position of each catalyst in the diagram phase according to the ICP-OES results. (Reprinted from Durussel, P.; Burri, G.; Feschotte, P., The binary system Ni-In. Journal of Alloys and Compounds 1997, 257 (1), 253-258. Copyright 1997 with permission from Elsevier.)

The morphology and the distribution of the metals were investigated by ex-situ STEM/EDS after the reduction as shown in Figure 5.3. The metals are homogeneously dispersed in the silica support with the formation of nanoparticles in all samples. Moreover, the particle size distribution was quantified for all catalysts by measuring the number frequency of particles from the TEM images (Figure 5.4). The average particle diameter for Ni/SiO_2 and $Ni\text{-}In/SiO_2$ catalysts is ~5 nm with a standard deviation of 0.08-0.31 nm. The formation of the phyllosilicate phase during the hydrothermal synthesis could be the reason of the small Ni particle size. The phyllosilicate phase (PS) is the catalyst precursor with sheets of silicate tetrahedrons that consist of a central silicon atom surrounded by four oxygen atoms at the corners of a tetrahedron.[18] After the H_2 reduction, this phase can provide a strong metal-support integration and high dispersion of the metals.[16] Moreover, it is not possible to observe any strong segregation of the metals or agglomeration of the particles caused by the addition of the second metal.

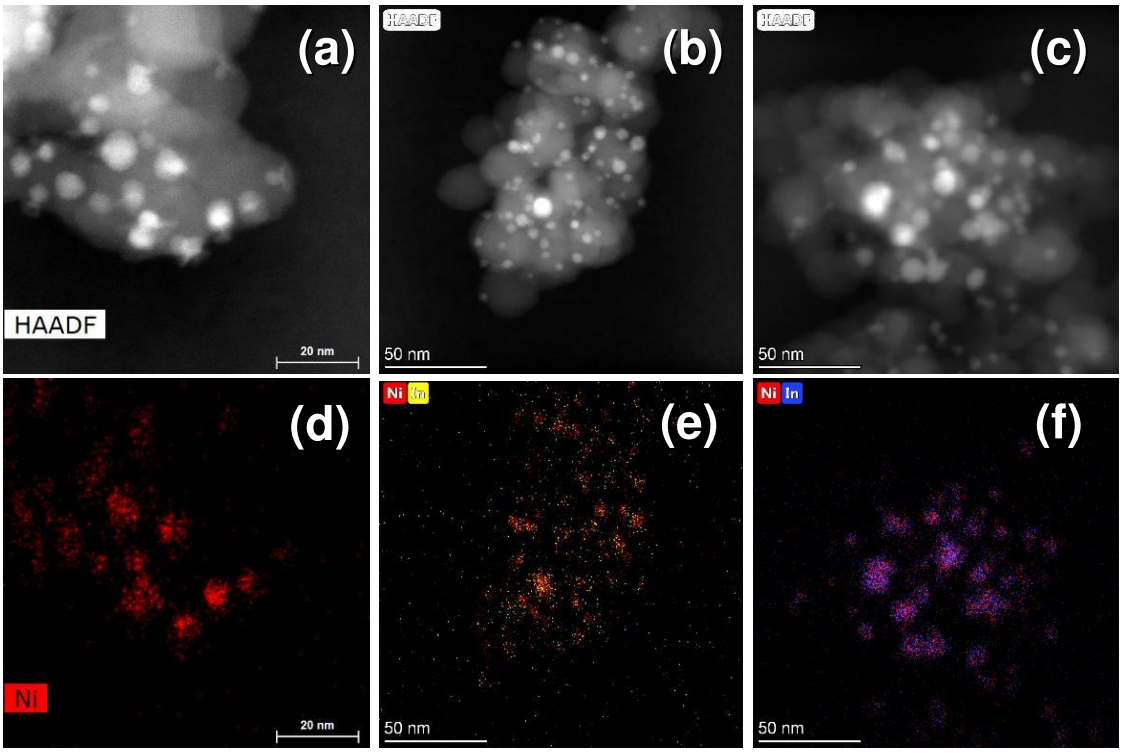

Figure 5.3: STEM-EDX mapping of the reduced Ni/SiO_2 (a,d), $Ni_{0.85}In_{0.15}/SiO_2$ (b,e), and (c,f) $Ni_{0.50}In_{0.50}/SiO_2$ catalysts.

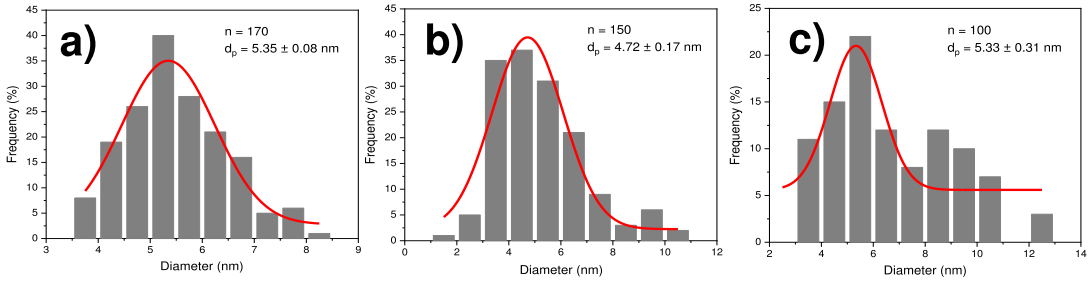

Figure 5.4: Histogram of particle size distribution for (a) Ni/SiO_2, (b) $Ni_{0.85}In_{0.15}/SiO_2$, and (c) $Ni_{0.50}In_{0.50}/SiO_2$ catalysts.

5.3.2 *In-situ* XRD-XAS characterizations during the rWGS reaction

5.3.2.1 *In-situ* XRD

To gain insights into the structure and oxidation state of the catalyst, we performed *in-situ* XRD combined with XAS of the pre-reduced catalysts. The data were collected following the steps shown in Figure 5.1. In addition, the diffractograms of the In_2O_3/SiO_2 used as reference is plotted in the Figure 5.5.

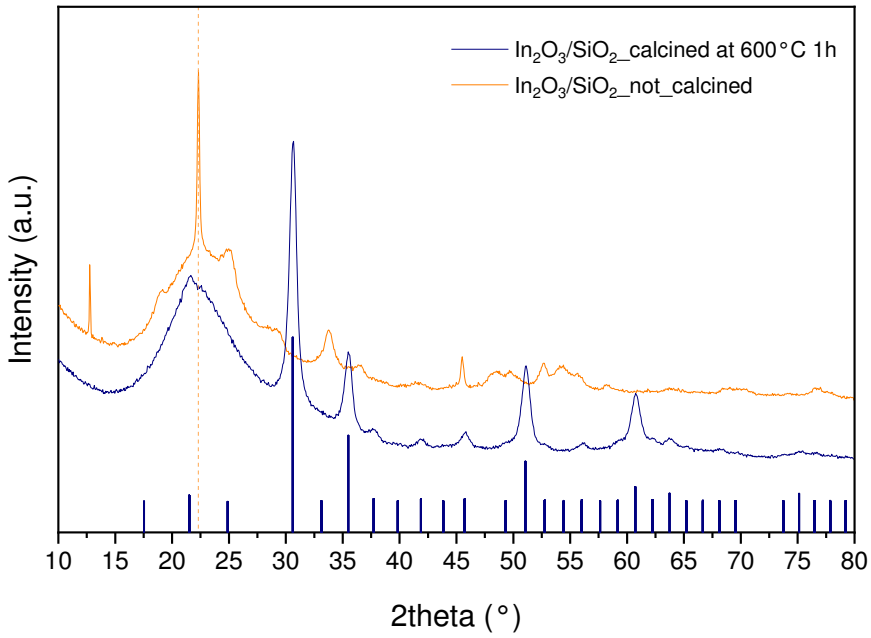

Figure 5.5: *Ex-situ* XRD profile of fresh and calcined In_2O_3/SiO_2 used as a reference of In^{3+}. The measurement was performed on Bruker AXS D8 advance. The X-ray diffractometer was equipped with a Lynxeye super speed detector using Cu K_α radiation (40 mA and 40 kV).

The XRD data are reported in Figure 5.6 that shows the last diffractogram collected after (i) 1 hour under H_2 reduction at 800 °C (final_reduction), (ii) cooling down step to 450 °C under N_2 (final_cooling), and (iii) after 1 hour under the reaction conditions (450 °C, 1 bar, CO_2:H_2:N_2 = 1:2:1, and GHSV = 120000 mL g^{-1}_{cat} h^{-1}) (final_reaction). Furthermore, the Rietveld refinement was performed using the data of the last diffractogram collected after the cooling step to provide more information about the crystal structure and unit cell parameters before the reaction (Table 5.2).

The XRD pattern for the Ni/SiO_2 shows (111), (200), and (220) reflections in all the three steps, which are associated with the metallic Ni with fcc type structure and space group F m -3 m according to ICSD 260169 (Figure 5.6a). The average crystallite size of nickel particles was determined through the Scherrer equation using $2\theta = 44.12°$. The obtained value is 5.2 nm, which is consistent with the particle size measured by STEM. Moreover, the lattice constants calculated by Rietveld refinement are a=b=c= 3.536 Å with a volume cell of 44.215 $Å^3$, which resulted in the following R- factors: R_p = 1.04%, R_{wp} = 1.73%, R_{exp} = 0.47%, and R_{Bragg} = 11.7%. The peaks kept in the same 2θ values in all steps except in the diffractogram after reduction

treatment that has a peak displacement to lower values of 2θ due to the thermal-induced lattice expansion.

Interestingly, it is possible to identify the formation of two phases in the $Ni_{0.85}In_{0.15}/SiO_2$ catalyst in Figure 5.6b. The first one is the Ni:In alloy phase (disordered structure), which remains in all treatments. The formation of the alloy phase could be confirmed by the shifting of the (111), (200), and (220) diffraction peaks to lower positions due to the insertion of the indium atom (ionic radius = 0.62 Å) in the cell structure causing a lattice expansion. This expansion caused an increase in the lattice parameters (a=b=c= 3.555 Å) as can be observed in the Rietveld refinement. The second one is the intermetallic Ni_3In phase (ordered structure) with $AuCu_3$ type structure and space group P m -3 m according to ICSD 59439. This intermetallic phase is characterized by the (111) and (200) diffraction peaks at lower values of 2θ (2θ = 41.45° and 47.99°, respectively) with lattice parameters equals a=b=c=3.778 Å.

Cherevotan et al.[19] observed the same phase transformation in their *operando* studies of N_7In_3/SBA-15 in CO_2 hydrogenation to methanol. They observed a phase transition of Ni_7In_3 (SG: P-1) to Ni3In (SG: P m -3 m) with an increase of pressure to 20 bar at 300 °C under reaction conditions. To confirm the origin of the Ni_3In phase, they performed the CO_2 hydrogenation using $NiO\text{-}In_2O_3$ without any pre-activation to avoid the intermetallic formation. In their controlled study, they conclude that both metals, derived from the oxide phases and reduced under reactant hydrogen at high temperature and pressure, diffuse to form the Ni_3In phase, which is catalytically stable in the CO_2 hydrogenation. Controversially, in our study, the new reflections related to Ni_3In phase appeared during the cooling of the sample (conditions: 450 °C, 1 bar, and N_2 flow) and remained constant during the reaction step. Thus, the variation of the temperature was enough to induce the diffusion of the atoms in the alloy structure forming the intermetallic Ni_3In phase. As can be seen in Figure 5.6b, this structure has fewer Ni-Ni neighbors due to the addition of indium in the corners of a cubic structure resulting in small Ni ensembles, and/or it can result in isolated Ni atoms. According to the Rietveld refinement, the estimated phase composition of the catalyst is 13.94% for Ni_3In intermetallic phase and 86.06% for the $Ni_{0.85}In_{0.15}$ alloy phase.

The identification of the peaks in the $Ni_{0.50}In_{0.50}/SiO_2$ is less straightforward, as it can be seen in Figure 5.6c. The major phase is the intermetallic $Ni_{13}In_9$ phase (ICSD 154798) that has In_9Pt_{13} structure type and C 1 2/m 1 as space group. According

to the Rietveld refinement, the lattice parameters are a = 14.787 Å, b = 8.397 Å, and c = 9.060 Å. However, there is a chance that this sample presents a second minor phase. Norén et al.[20] described the $Ni_{13}In_9$ structure as the formation of two kinds of layers (A-layer and B-layer) that stack alternately among the original parent c-direction. Besides a detailed description, the authors reinforce that the A-layer above a B-Layer is necessarily displaced ½ a (≡ ½ b) compared to the A-layer below that resulting in a slightly distorted F-centred orthorhombic cell. The stacking sequence along an axis is arranged almost perpendicular to the ab-plane which can be observed in Figure 5.7. Details of the refinement are plotted in Figure 5.8 and summarized in Table 5.2.

Table 5.2: Rietveld analysis parameters for Ni/SiO_2 and $Ni\text{-}In/SiO_2$**.**

	Ni/SiO_2	**$Ni_{0.85}In_{0.15}/SiO_2$**		**$Ni_{0.50}In_{0.50}/SiO_2$**
Phase		$Ni_{0.85}In_{0.15}$	Ni_3In	$Ni_{13}In_9$
Space Group	F m -3 m	F m -3 m	P m -3 m	C 1 2/m 1
Unit cell parameters				
a (Å)	3.5361 (0.00023)	3.55516 (0.00035)	3.77812 (0.00063)	14.78725 (0.00327)
b (Å)	3.5361 (0.00023)	3.55516 (0.00035)	3.77812 (0.00063)	8.39723 (0.00048)
c (Å)	3.5361 (0.00023)	3.55516 (0.00035)	3.77812 (0.00063)	9.06060 (0.00165)
V ($Å^3$)	44.215 (0.005)	44.934 (0.008)	53.929 (0.0016)	665.768 (0.194)
R_p/R_{wp}	1.04/1.73	1.60/1.90		1.66/2.72
R_{exp}	0.47	0.43		0.45
R_{Bragg}	11.7	25.8	33.6	32.1
Chi_2	13.7	19.5		36.4

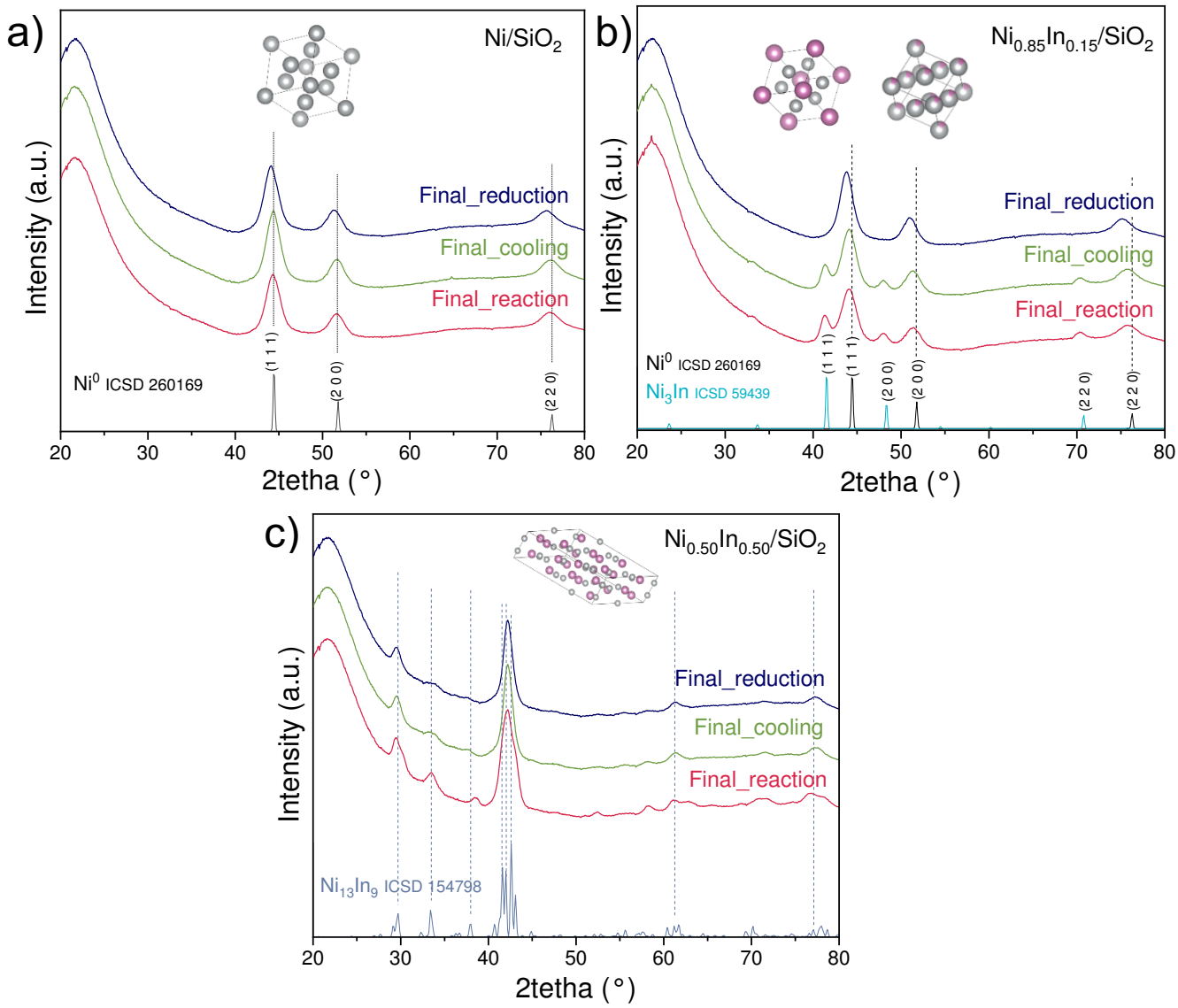

Figure 5.6: Selected *in situ* XRD patterns of the (a) Ni/SiO_2, (b) $Ni_{0.85}In_{0.15}/SiO_2$, and (c) $Ni_{0.50}In_{0.50}/SiO_2$ catalysts recorded during the reduction, cooling, and reaction stages ($\lambda = 1.5408$ Å). The Ni and In atoms are represented by the gray and pink colors, respectively.

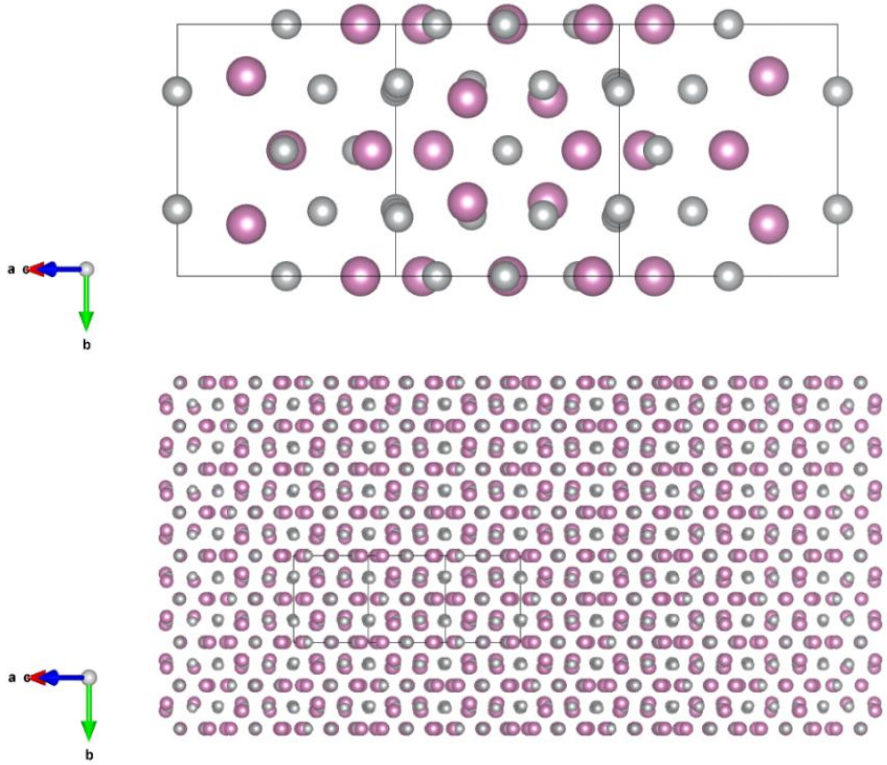

Figure 5.7: Crystal structure scheme representing the stacked layers of the $Ni_{13}In_9$.

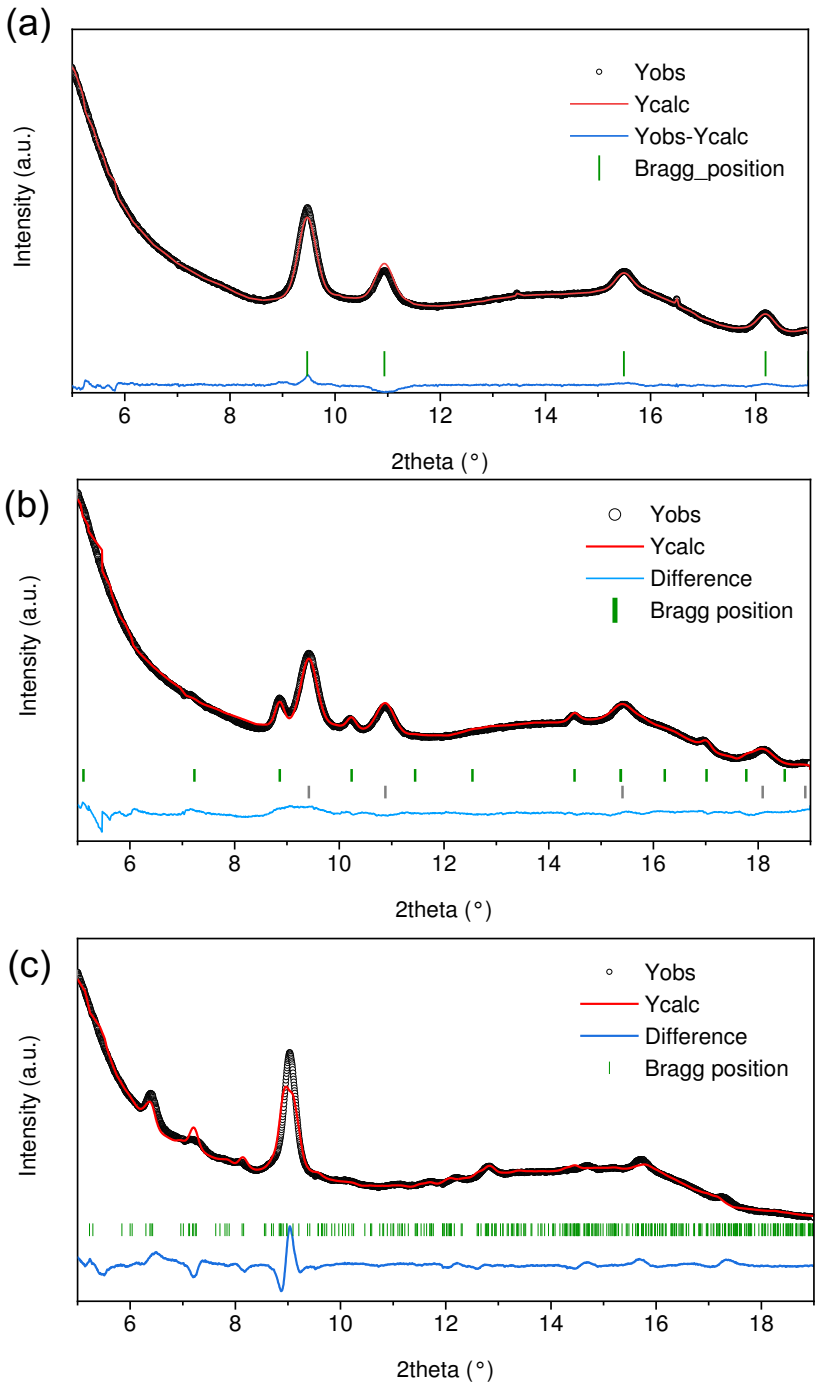

Figure 5.8: Last XRD diffractogram (λ =0.337 Å) of the cooling down and the fits from the Rietveld refinement for (a) Ni/SiO_2, (b) $Ni_{0.85}In_{0.15}/SiO_2$, and (c) $Ni_{0.50}In_{0.50}/SiO_2$ catalysts.

5.3.2.2 *In-situ* XAS

The local structure and oxidation state of the metals were investigated by *in situ* X-ray absorption spectra for all the pre-reduced catalysts. The normalized Ni K-

edge and In K-edge X-ray absorption near-edge (XANES) at room temperature as well as the reference are shown in Figure 5.9. At In K-edge, Ni-In samples spectra have similar In_2O_3 features indicating that the indium is fully oxidized in the $Ni_{0.85}In_{0.15}/SiO_2$ sample and partially oxidized in the $Ni_{0.50}In_{0.50}/SiO_2$. The same occurs at Ni K-edge, whereby the Ni is partially oxidized due to the exposure of all samples to air. Plotting in the same sequence of XRD data, Figure 5.10 shows the last spectra of each catalyst under *in situ* conditions of reduction, cooling, and reaction. After the reduction at 800 °C under 10% H_2/N_2, all the samples have similar features of the Ni foil spectrum, indicating a complete reduction of NiO phase.

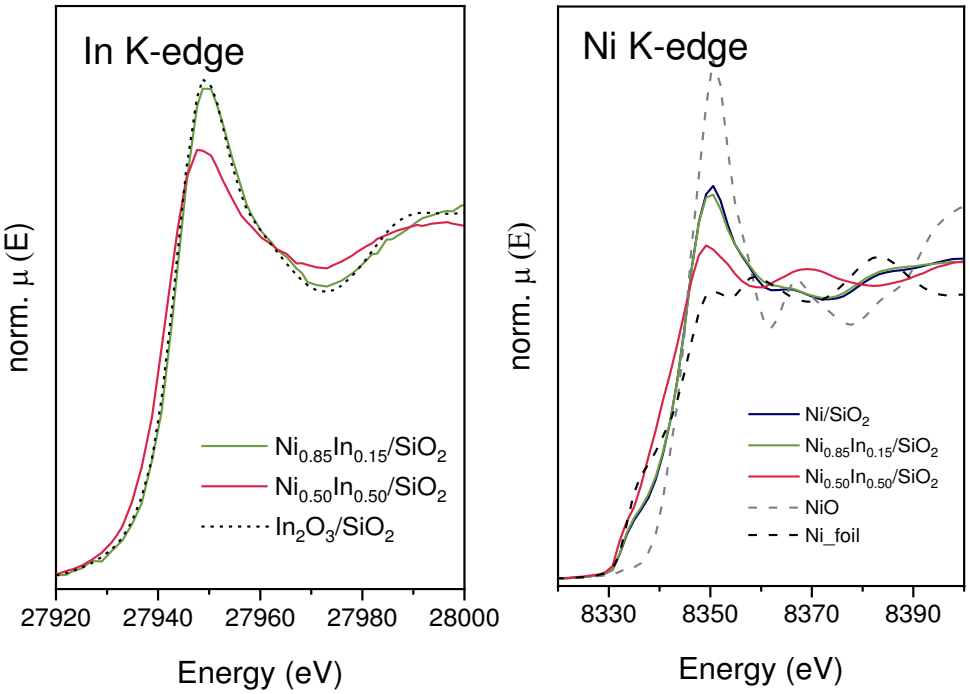

Figure 5.9: *In situ* In K-edge and Ni K-edge XANES spectra of the pre-reduced catalysts of Ni/SiO_2 (blue), $Ni_{0.85}In_{0.15}/SiO_2$ (green), and $Ni0_{.50}In_{0.50}/SiO_2$ (red) after the exposure to air. Experimental spectra are compared against a measured In_2O_3/SiO_2, Ni^0, and NiO standard (dashed lines).

Comparing the catalysts after 1h of reduction, Ni/SiO_2 and $Ni_{0.85}In_{0.15}/SiO_2$ have the same white line intensity with an E_0 equal to 8335.3 eV and features with small differences in the XANES shape. After the cooling down under N_2, it is possible to observe a small shift of E_0 towards lower positions for the $Ni_{0.85}In_{0.15}/SiO_2$, which could be related to the formation of the Ni_3In intermetallic phase as observed by XRD data. In addition, the higher content of In in $Ni_{0.50}In_{0.50}/SiO_2$ caused a shift in the

absorption edge to low photon energy (E0 = 8333.9 eV) and decreased the white line intensity. The intermetallic Ni-In compound exhibits distinct features compared to the Ni foil spectrum, which indicates that the formed intermetallic phase has a different coordination environment and chemical bonds. These changes observed in XANES could be a result of the enrichment of electrons on the Ni atom caused by the alloying of the nickel and indium.[19, 21-23]

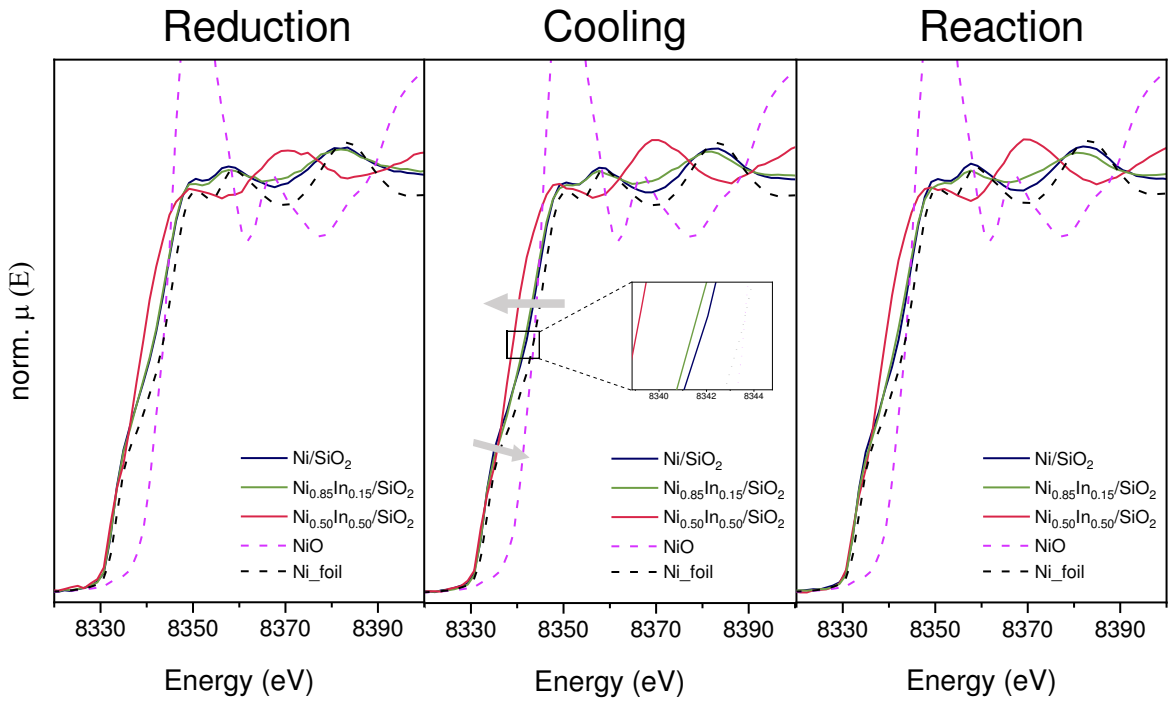

Figure 5.10: *In situ* Ni K-egde XANES collected under the (a) reduction (800 °C, 1 bar, 10% H_2/N_2), (b) cooling to 450 °C, and (c) rWGS reaction (450 °C, 1 bar, $CO_2:H_2:N_2$ = 1:2:1) for Ni/SiO_2 (blue), $Ni_{0.85}In_{0.15}/SiO_2$ (green), and $Ni0.50In_{0.50}/SiO_2$ (red). Experimental spectra are compared against a measured Ni and NiO standard (dashed lines).

Chen et al.[23] evaluated the effect of the In species on the electronic structure of Ni using XPS measurements. The results showed that Ni $2p_{3/2}$ peak slightly shifted to lower energies with the increasing of the indium contents in the intermetallic compound. Furthermore, the In 3d XPS spectra also exhibited a shift to higher electron binding energy of both In $3d_{5/2}$ and In $3_{d3/2}$ peaks. According to the authors, these results indicate the charge transfer from In to Ni, which increases the effect with higher indium contents. Similar observations were observed by Li et al.[21], Wang et al.[24], Wang et al.[22], and Cherevotan et al[19]. Furthermore, electronic effects are also observed

by other bi-metallic systems such as Ni-Zn[25], Ni-Sn[26], Pt-Cu[27], Sn-Co[28], Pd-In[11, 29, 30], Pd-Ga[31, 32], and Pd-Cu[33]. Upon switching to the reaction conditions (450 °C, 1 bar, CO_2:H_2:N_2 = 1:2:1), no remarkable changes were evidenced in XANES spectra at Ni K-edge, which indicates that the Ni remained unchanged during the first hour of the rWGS reaction.

The k^2-weighted magnitudes of the Fourier transform of Ni K-edge EXAFS oscillations in R-space are shown in Figure 5.11. Comparing the Ni/SiO_2 and $Ni_{0.85}In_{0.15}/SiO_2$, it is possible to observe similar shapes with the largest scatterings at 2.11 Å and smallest at 3.20 Å, although there are some differences in the amplitude. On the other hand, the $Ni_{0.50}In_{0.50}/SiO_2$ catalyst exhibited completely three different peaks at 1.29 Å, 1.84 Å, and 2.36 Å. As observed in the XRD data, the complex structure of $Ni_{13}In_9$ existent in this catalyst led to these distinct features. Hsu et al.[34] obtained similar EXAFS shape data from which the authors reported pioneer theoretical and experimental XANES and EXAFS of the $Ni_{13}In_9$ system.

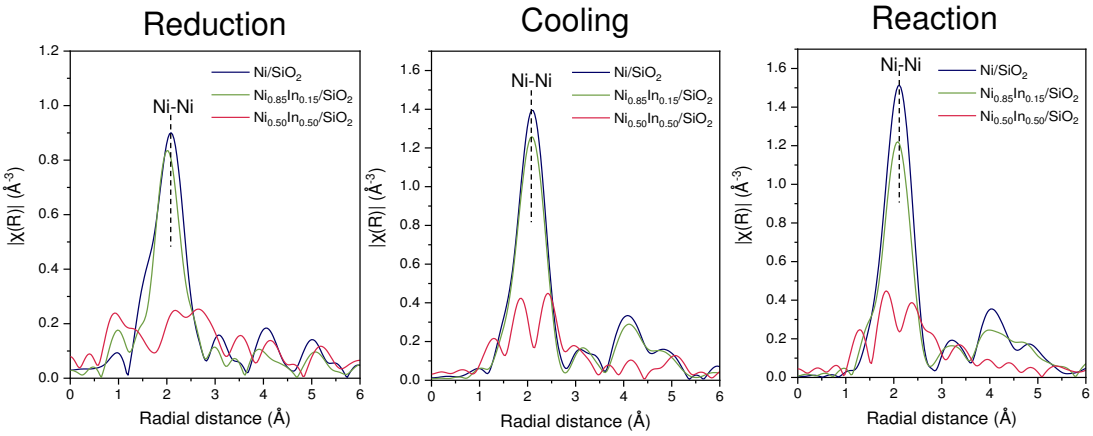

Figure 5.11: *In situ* Ni K-edge EXAFS collected on the Ni/SiO_2 and bimetallic Ni-In/SiO_2 samples under the (a) reduction conditions (800 °C, 1 bar, 10% H_2/N_2), (b) cooling down step at 450 °C, and (c) rWGS reaction conditions (450 °C, 1 bar, CO_2:H_2:N_2 = 1:2:1).

5.3.3 Catalytic tests

The Ni-In catalysts were screened for the rWGS reaction at 450 °C, 1 bar, and different reaction mixture as shown in Figure 5.12 and Table 5.3. We analyzed the effect of the Ni:In molar ratio and the feed composition in terms of CO_2 consumption rate, CO selectivity, and CO formation rate. CO and CH_4 were the only products

detected, although a possible formation of traces of alcohols or other oxygenated compounds cannot be discarded due to detection limit or no favorable reaction conditions. In comparison, the addition of indium promotes the selectivity towards CO, reaching 100% in the $Ni_{0.50}In_{0.50}/SiO_2$ catalyst in the same feed composition. Noteworthy mentioning is that alloying Ni with a small amount of In (In/Ni+In = 0.15) promotes the CO selectivity to almost 100%, with a good CO formation rate. According to XRD, the $Ni_{0.85}In_{0.15}/SiO_2$ formed two phases: the disordered alloy as a major phase and the intermetallic Ni_3In phase as a minor phase. However, it is still unclear the role of each phase in terms of promotion of selectivity. Based on our results, a minimum In content is desirable since the catalyst with higher indium content presented approximately half of the values for CO_2 consumption and CO formation rates observed for the pure Ni/SiO_2 catalyst.

To evaluate the effect of feed composition, the H_2:CO_2 ratio was increased from 2 to 5 keeping the same gas hour space velocity (120000 mL g^{-1}_{cat} h^{-1}). This range involves the favored condition to the methanation pathway that is H_2:CO_2 equal to 4 in which sufficient H* is available to fully hydrogenate the *CO species to form CH_4.[35] Accordingly, the increase in the H_2 partial pressure led to an increase in the CH_4 selectivity and CO_2 rate consumption followed by a decrease in the CO formation for the Ni/SiO_2 and, to a lesser extent, for the bimetallic $Ni_{0.85}In_{0.15}/SiO_2$. However, the CO selectivity (100%) and the CO_2 rate consumption of the intermetallic $Ni_{0.50}In_{0.50}/SiO_2$ catalyst remained unchanged with increasing the hydrogen concentration in the reaction mixture. Conversely, the intermetallic catalyst had the lowest CO formation rate which decreased with the increase of H_2:CO_2 ratio, resulting in the same trend as the other catalysts. Thus, the CO could be formed by the direct dissociation of the *CO_2 species to *CO and O* or the hydrogenation of the *CO_2 species forming the carboxylate (*HOCO) intermediate that dissociates to *CO and *OH.[35, 36] Thereby, in order to explain the CO formation rate drop, two hypotheses could be considered. Firstly, if the CO production occurs via the direct CO_2 dissociation, the decrease in the partial pressure of CO_2 negatively and directly impacts the CO formation rate on the Ni-In bimetallic catalysts. Secondly, the lack of sufficient active sites for the hydrogenation reaction to occur, that causes a possible competition between the dissociation of the CO_2 and H_2 in the surface Ni sites.

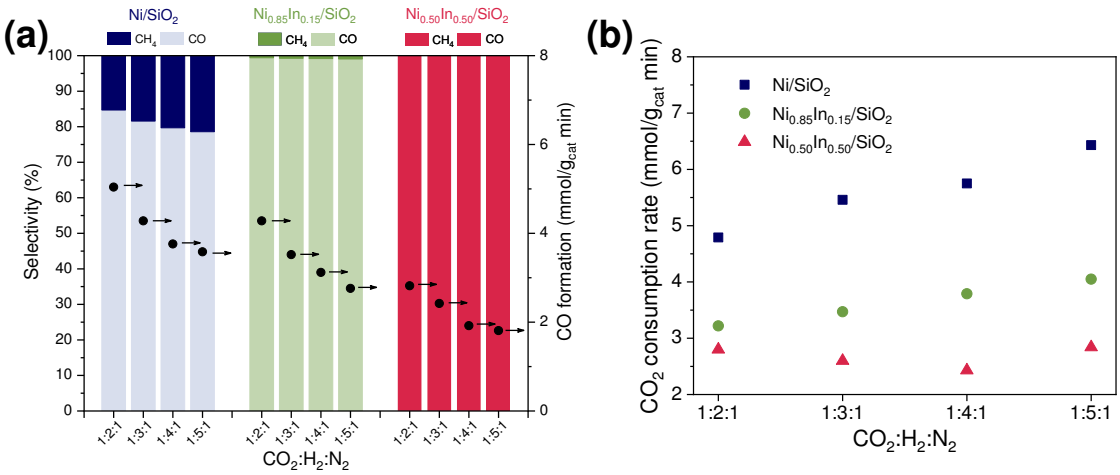

Figure 5.12: (a) Product selectivity and CO formation rate and (b) CO_2 consumption rate under different reaction mixture of rWGS reaction (450 °C,1 bar, and GHSV = 120000 mL g^{-1}_{cat} h^{-1}).

Table 5.3: Summary of the catalytic data in terms of consumption/formation rate and selectivity for the rWGS at 450 °C, 1 bar, and GHSV = 120000 mL g^{-1}_{cat} h^{-1}).

	$CO_2:H_2:N_2$	CO_2 consumption rate	CO formation rate	S_{CO}	S_{CH4}
		($mmol/g_{cat}$ min)	($mmol/g_{cat}$ min)	(%)	(%)
Ni/SiO_2	1:2:1	4.79	5.04	84.7	15.2
	1:3:1	5.46	4.28	81.6	18.4
	1:4:1	5.75	3.76	79.7	20.2
	1:5:1	6.43	3.58	78.6	21.3
$Ni_{0.85}In_{0.15}/SiO_2$	1:2:1	3.22	4.28	99.4	0.6
	1:3:1	3.47	3.52	99.3	0.7
	1:4:1	3.79	3.12	99.2	0.8
	1:5:1	4.05	2.76	99.1	0.9
$Ni_{0.50}In_{0.50}/SiO_2$	1:2:1	2.80	2.82	100	0
	1:3:1	2.60	2.42	100	0
	1:4:1	2.43	1.92	100	0
	1:5:1	2.84	1.81	100	0

5.3.4 CO-DRIFTS

The CO-DRIFTS experiments were performed in two different conditions: under 20 mL/min of 1.7% CO/N_2 at room temperature for 30 min assuming the saturation coverages for each sample. At the same temperature, the N_2 flow was used to flush the CO gas-phase off remaining only the signal of the adsorbed species on the

surface of the particles. The DRIFTS spectra for Ni and Ni-In samples were recorded for both conditions in a region between 2300 – 1800 cm^{-1}, as shown Figure 5.13. For all samples, under CO/N_2 flow, the symmetrical broad peaks appearing at 2170 and 2117 cm^{-1} correspond to characteristic bands for CO present in the gas phase[37].

The Ni/SiO_2 catalyst presents a peak at 2088 cm^{-1}, which is assigned to linear CO adsorbed at Ni species forming subcarbonyls ($Ni(CO)_n$, where n = 2-3).[38, 39] The band at 2054 cm^{-1} could be associated with chemisorbed monocarbonyls and physically adsorbed tetracarbonyls species. Both species coincide the band position and the stability on the surface is the main parameter to distinguish them.[40, 41] It is known that $Ni(CO)_4$ are weakly bonded and its desorption could be observed at room temperature or higher temperatures[37]. Thereby, in the first minutes of CO flow, the intensity of the 2054 cm^{-1} band decreases which could be the indication of the desorption of the physically adsorbed $Ni(CO)_4$ on the surface.[39] After that, the intensity of this band remains unchanged representing the monocarbonyls linearly bounded to metallic Ni sites. The broad band at 1930 cm^{-1} is ascribed to the bridge-bonded CO, specifically to CO species bound to three neighboring Ni atoms.[38, 41] After the N_2 flush, the band related to the linear bonded CO on the Ni species slightly shifted to lower values of wavelength, remaining stable in terms of intensity and band position. Besides the linear bounded CO, the CO adsorbed in a tri-fold bridge position represented by the band at 1930 cm^{-1} kept stable during the flushing with nitrogen at room temperature.[38]

As it can be seen in Figure 5.13b (left-hand side), under CO/N_2 flow, the $Ni_{0.85}In_{0.15}/SiO_2$ catalyst also exhibited bands at 2080 and 2058 cm^{-1}, which are assigned to CO linearly adsorbed on the surface Ni sites[37, 38, 42]. Only one broad band at 2050 cm^{-1} remains after the flush (Figure 5.13b – right-hand side). According to Németh et al.[43], the CO peak can shift to lower frequencies due to geometric and electronic effects. As reported by de Mérnoval et al.[44], the presence of a metal modifier, that acts as an electron donor, causes an increase in the electron density of surrounding Ni sites and, hence, an increase in the back-donation of electrons from d-orbitals of the "parent" metal to the antibonding orbital of CO. However, the authors highlighted that this type of interaction is only relevant if the electronegativity of the modifier metal is significantly lower. In our case, the difference of electronegativity between Ni and In is 0.13, indicating that not only the electronic effect but also the

geometric effect could be responsible for this shift of the vibration frequency of linear CO molecules.[43]

Interestingly, for the intermetallic $Ni_{0.50}In_{0.50}/SiO_2$, only peaks related to the gas phase were observed, indicating that the CO adsorbs and quickly desorbs on the surface, remaining in the gas phase. Therefore, the lack of bridge carbonyl band indicates that the addition of indium decreased the number of adjacent Ni sites mitigating a more stable bound configuration. Similar results were obtained by Wu et al.[30] and Furukawa et al.[45] using the PdIn intermetallic compound. The authors reported that the formation of the intermetallic compound lead to the disappearance of the bridged and threefold hollow bonded CO, as well as, a shift of 10-25 cm^{-1} in the linearly adsorbed CO. Furthermore, Furukawa et al.[45] suggested that the lower energy of the peak of linear adsorbed CO on $PdIn/SiO_2$ compared to Pd/SiO_2 is indicative of negatively charged Pd atoms in the PdIn catalysts. In our scenario, partial electronic influence in the Ni atoms could be indicated by a small shift to lower energy (2050 cm^{-1}) for $Ni_{0.85}In_{0.15}/SiO_2$ and by the no existence of linear CO bonding peaks after the N_2 flushing for $Ni_{0.50}In_{0.50}/SiO_2$ which agree with the XANES results. These results reveal that the strength of the CO intermediate has an important role to control the product selectivity in the CO_2 hydrogenation. Thereby, the formation of CH_4/CH_3OH/hydrocarbons occurs whether the catalyst has a moderate CO binding strength to keep the CO species available to be hydrogenated by H_{ads} adsorbed in the adjacent sites. Hence, the high CO selectivity for the Ni-In bimetallic catalyst could be explained by the geometric and electronic effects caused by the presence of the indium.

As mentioned in the CO-DRIFTS results, the isolation of the surface Ni atoms due to the insertion of the In atoms in the structure diminish the formation of Ni ensembles, which allows a more strong CO adsorption for subsequently hydrogenation to CH_4.[35, 46] The indium atoms act as an inert component for the CO_2 hydrogenation and their presence could decrease the availability of the active Ni sites on the surface of the catalyst.[21, 30] Moreover, the decrease in the catalytic activity and the low CO adsorption strength are also associated with an electronic effect caused by the interaction of the In atoms and the metallic Ni in the formation of the bi-metallic bond. In addition, further characterizations are needed to investigate the arrangement of atoms on the surface of the catalysts, as well as to conduct an extensive study involving

molecular simulations and DFT to understand in depth the electronic effect and its extent.

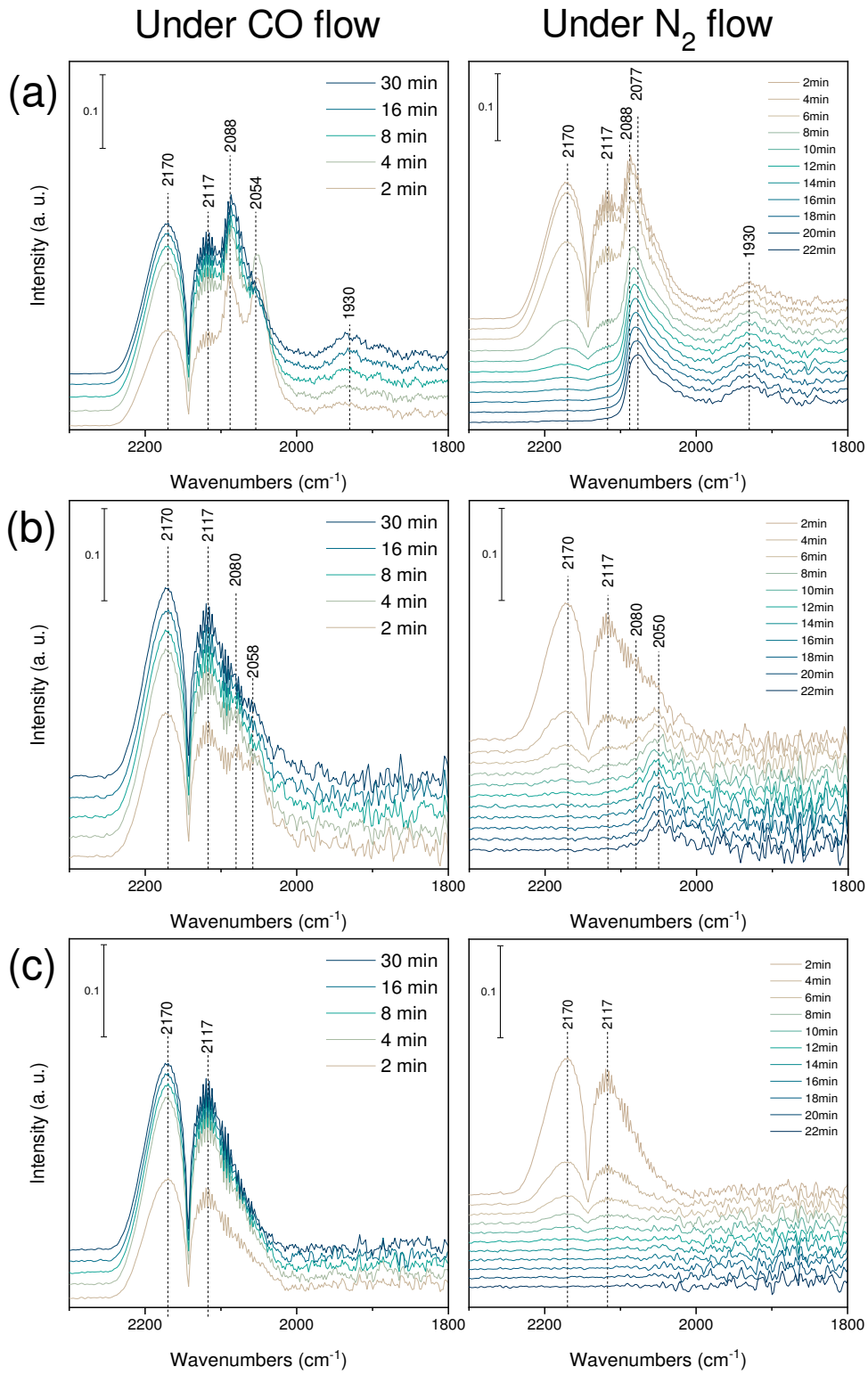

Figure 5.13: DRIFTS spectra of CO adsorption in the region of 2300-1800 cm^{-1} on (a) Ni/SiO_2, (b) $Ni_{0.85}In_{0.15}/SiO_2$, and (c) $Ni_{0.50}In_{0.50}/SiO_2$ at room temperature for 30 min and after purged for 22 min by N_2.

5.4 Conclusions

Monometallic Ni and bimetallic Ni-In supported on silica were synthesized by hydrothermal method, characterized and tested in the rWGS reaction at 450 °C and 1 bar. This method produced nanoparticles with 5 nm of particle diameter and homogeneously dispersed metals on the support surface. Interestingly, XRD data evidenced the formation of an intermetallic N_3In phase in the $Ni_{0.85}In_{0.15}/SiO_2$ alloy during cooling down to the reaction temperature. Furthermore, the loss of indium during the reduction caused the formation of a complex intermetallic phase $Ni_{13}In_9$ in the $Ni_{0.50}In_{0.50}/SiO_2$ catalyst. The XAS results revealed that the formation of these phases caused a shift to lower photon energy of Ni-In catalysts during the cooling step, which could be associated with an electronic influence of In species. In addition, a different coordination environment and chemical bond were exhibited by $Ni_{0.50}In_{0.50}/SiO_2$ due to the formation of the complex $Ni_{13}In_9$ phase.

In the catalytic tests, the Ni-In catalysts showed high CO selectivity, reaching 100% for the $Ni_{0.50}In_{0.50}/SiO_2$. A small addition of indium was enough to reach above 99% even in a higher CO_2:H_2 feed ratio. Overall, an optimal Ni:In ratio might be selected to reach high selectivity towards CO with a good CO_2 consumption rate, since higher In content decreased the CO formation rate. The CO-DRIFTS results revealed that the adsorption strength of the CO is the key factor to understanding this excellent selectivity. The weak CO bond on the Ni surface sites is likely due to an electronic influence and a geometric effect provided by the presence of inert In atoms that mitigate the formation of Ni ensembles. These ensembles are necessary for the bridged bounded CO species, resulting in a more stable configuration that allows the hydrogenation of these species to form methane.

5.5 References

1. Taylor, L. L.; Quirk, J.; Thorley, R. M. S.; Kharecha, P. A.; Hansen, J.; Ridgwell, A.; Lomas, M. R.; Banwart, S. A.; Beerling, D. J., Enhanced weathering strategies for stabilizing climate and averting ocean acidification. *Nature Climate Change* **2015,** *6* (4), 402-406. https://doi.org/10.1038/nclimate2882

2. Hoegh-Guldberg, O.; Mumby, P. J.; Hooten, A. J.; Steneck, R. S.; Greenfield, P.; Gomez, E.; Harvell, C. D.; Sale, P. F.; Edwards, A. J.; Caldeira, K.; Knowlton, N.; Eakin, C. M.; Iglesias-Prieto, R.; Muthiga, N.; Bradbury, R. H.; Dubi, A.; Hatziolos, M. E., Coral reefs under rapid climate change and ocean acidification. *Science* **2007,** *318* (5857), 1737-1742. https://doi.org/10.1126/science.1152509

3. Ye, R. P.; Ding, J.; Gong, W.; Argyle, M. D.; Zhong, Q.; Wang, Y.; Russell, C. K.; Xu, Z.; Russell, A. G.; Li, Q.; Fan, M.; Yao, Y. G., CO_2 hydrogenation to high-value products via heterogeneous catalysis. *Nat Commun* **2019,** *10* (1), 5698. https://doi.org/10.1038/s41467-019-13638-9
4. Chen, X.; Su, X.; Su, H.-Y.; Liu, X.; Miao, S.; Zhao, Y.; Sun, K.; Huang, Y.; Zhang, T., Theoretical insights and the corresponding construction of supported metal catalysts for highly selective CO_2 to CO Conversion. *ACS Catalysis* **2017,** *7* (7), 4613-4620. https://doi.org/10.1021/acscatal.7b00903
5. Porosoff, M. D.; Yan, B.; Chen, J. G., Catalytic reduction of CO_2 by H_2 for synthesis of CO, methanol and hydrocarbons: challenges and opportunities. *Energy & Environmental Science* **2016,** *9* (1), 62-73. https://doi.org/10.1039/c5ee02657a
6. Kattel, S.; Liu, P.; Chen, J. G., Tuning selectivity of CO_2 hydrogenation reactions at the metal/oxide interface. *J Am Chem Soc* **2017,** *139* (29), 9739-9754. https://doi.org/10.1021/jacs.7b05362
7. Zhu, M.; Ge, Q.; Zhu, X., Catalytic reduction of CO_2 to CO via reverse water gas shift reaction: recent advances in the design of active and selective supported metal catalysts. *Transactions of Tianjin University* **2020,** *26* (3), 172-187. https://doi.org/10.1007/s12209-020-00246-8
8. Károlyi, J.; Németh, M.; Evangelisti, C.; Sáfrán, G.; Schay, Z.; Horváth, A.; Somodi, F., Carbon dioxide reforming of methane over Ni–In/SiO_2 catalyst without coke formation. *Journal of Industrial and Engineering Chemistry* **2018,** *58*, 189-201. https://doi.org/10.1016/j.jiec.2017.09.024
9. Studt, F.; Sharafutdinov, I.; Abild-Pedersen, F.; Elkjaer, C. F.; Hummelshoj, J. S.; Dahl, S.; Chorkendorff, I.; Norskov, J. K., Discovery of a Ni-Ga catalyst for carbon dioxide reduction to methanol. *Nat Chem* **2014,** *6* (4), 320-4. https://doi.org/10.1038/nchem.1873
10. Liu, D.; Li, Y.; Kottwitz, M.; Yan, B.; Yao, S.; Gamalski, A.; Grolimund, D.; Safonova, O. V.; Nachtegaal, M.; Chen, J. G.; Stach, E. A.; Nuzzo, R. G.; Frenkel, A. I., Identifying dynamic structural changes of active sites in Pt–Ni bimetallic catalysts using multimodal approaches. *ACS Catalysis* **2018,** *8* (5), 4120-4131. https://doi.org/10.1021/acscatal.8b00706
11. Snider, J. L.; Streibel, V.; Hubert, M. A.; Choksi, T. S.; Valle, E.; Upham, D. C.; Schumann, J.; Duyar, M. S.; Gallo, A.; Abild-Pedersen, F.; Jaramillo, T. F., Revealing the synergy between oxide and alloy phases on the performance of bimetallic In–Pd catalysts for CO_2 hydrogenation to methanol. *ACS Catalysis* **2019,** *9* (4), 3399-3412. https://doi.org/10.1021/acscatal.8b04848
12. Naeem, M. A.; Armutlulu, A.; Imtiaz, Q.; Donat, F.; Schaublin, R.; Kierzkowska, A.; Muller, C. R., Optimization of the structural characteristics of CaO and its effective stabilization yield high-capacity CO_2 sorbents. *Nat Commun* **2018,** *9* (1), 2408. https://doi.org/10.1038/s41467-018-04794-5
13. Ravel, B.; Newville, M., ATHENA, ARTEMIS, HEPHAESTUS: data analysis for X-ray absorption spectroscopy using IFEFFIT. *Journal of synchrotron radiation* **2005,** *12* (4), 537-541. https://doi.org/10.1107/S0909049505012719
14. Kieffer, J.; Wright, J., PyFAI: a Python library for high performance azimuthal integration on GPU. *Powder Diffraction* **2013,** *28* (S2), S339-S350. https://doi.org/10.1017/S0885715613000924
15. Abdala, P. M.; Mauroy, H.; Van Beek, W., A large-area CMOS detector for high-energy synchrotron powder diffraction and total scattering experiments. *Journal of Applied Crystallography* **2014,** *47* (1), 449-457. https://doi.org/10.1107/S1600576713034067
16. Bian, Z.; Kawi, S., Preparation, characterization and catalytic application of phyllosilicate: A review. *Catalysis Today* **2020,** *339*, 3-23. https://doi.org/10.1016/j.cattod.2018.12.030
17. Marakatti, V. S.; Peter, S. C., Synthetically tuned electronic and geometrical properties of intermetallic compounds as effective heterogeneous catalysts. *Progress in Solid State Chemistry* **2018,** *52*, 1-30. https://doi.org/10.1016/j.progsolidstchem.2018.09.001

18. Sivaiah, M. V.; Petit, S.; Beaufort, M. F.; Eyidi, D.; Barrault, J.; Batiot-Dupeyrat, C.; Valange, S., Nickel based catalysts derived from hydrothermally synthesized 1:1 and 2:1 phyllosilicates as precursors for carbon dioxide reforming of methane. *Microporous and Mesoporous Materials* **2011,** *140* (1-3), 69-80. https://doi.org/10.1016/j.micromeso.2010.09.015
19. Cherevotan, A.; Raj, J.; Dheer, L.; Roy, S.; Sarkar, S.; Das, R.; Vinod, C. P.; Xu, S.; Wells, P.; Waghmare, U. V.; Peter, S. C., Operando generated ordered heterogeneous catalyst for the selective conversion of CO_2 to methanol. *ACS Energy Letters* **2021,** *6* (2), 509-516. https://doi.org/10.1021/acsenergylett.0c02614
20. Norén, L.; Larsson, A. K.; Withers, R. L.; Rundlöf, H., A neutron and X-ray powder diffraction study of B82 related superstructure phases in the Ni–In system. *Journal of Alloys and Compounds* **2006,** *424* (1-2), 247-254. https://doi.org/10.1016/j.jallcom.2005.10.092
21. Li, C.; Chen, Y.; Zhang, S.; Xu, S.; Zhou, J.; Wang, F.; Wei, M.; Evans, D. G.; Duan, X., Ni–In intermetallic nanocrystals as efficient catalysts toward unsaturated aldehydes hydrogenation. *Chemistry of Materials* **2013,** *25* (19), 3888-3896. https://doi.org/10.1021/cm402183
22. Wang, L.; Niu, X.; Chen, J., SiO_2 supported Ni-In intermetallic compounds: efficient for selective hydrogenation of fatty acid methyl esters to fatty alcohols. *Applied Catalysis B: Environmental* **2020,** *278*. https://doi.org/10.1016/j.apcatb.2020.119293
23. Chen, Y.; Chen, J., Selective hydrogenation of acetylene on SiO_2 supported Ni-In bimetallic catalysts: Promotional effect of In. *Applied Surface Science* **2016,** *387*, 16-27. https://doi.org/10.1016/j.apsusc.2016.06.067
24. Wang, X.; Chen, J., Effects of indium on Ni/SiO_2 catalytic performance in hydrodeoxygenation of anisole as model bio-oil compound: Suppression of benzene ring hydrogenation and C–C bond hydrogenolysis. *Chinese Journal of Catalysis* **2017,** *38* (11), 1818-1830. https://doi.org/10.1016/s1872-2067(17)62910-3
25. Pan, Z.; Wang, R.; Chen, J., Deoxygenation of methyl laurate as a model compound on Ni-Zn alloy and intermetallic compound catalysts: Geometric and electronic effects of oxophilic Zn. *Applied Catalysis B: Environmental* **2018,** *224*, 88-100. https://doi.org/10.1016/j.apcatb.2017.10.040
26. Marakatti, V. S.; Arora, N.; Rai, S.; Sarma, S. C.; Peter, S. C., Understanding the role of atomic ordering in the crystal structures of NixSny toward efficient vapor phase furfural hydrogenation. *ACS Sustainable Chemistry & Engineering* **2018,** *6* (6), 7325-7338. https://doi.org/10.1021/acssuschemeng.7b04586
27. Liu, J.; Lucci, F. R.; Yang, M.; Lee, S.; Marcinkowski, M. D.; Therrien, A. J.; Williams, C. T.; Sykes, E. C.; Flytzani-Stephanopoulos, M., Tackling CO poisoning with single-atom alloy catalysts. *J Am Chem Soc* **2016,** *138* (20), 6396-9. https://doi.org/10.1021/jacs.6b03339
28. Zhou, J.; Yang, Y.; Li, C.; Zhang, S.; Chen, Y.; Shi, S.; Wei, M., Synthesis of Co–Sn intermetallic nanocatalysts toward selective hydrogenation of citral. *Journal of Materials Chemistry A* **2016,** *4* (33), 12825-12832. https://doi.org/10.1039/c6ta04542a
29. Cao, Y.; Sui, Z.; Zhu, Y.; Zhou, X.; Chen, D., Selective hydrogenation of acetylene over $Pd\text{-}In/Al_2O_3$ catalyst: Promotional effect of indium and composition-dependent performance. *ACS Catalysis* **2017,** *7* (11), 7835-7846. https://doi.org/10.1021/acscatal.7b01745
30. Wu, Z.; Wegener, E. C.; Tseng, H.-T.; Gallagher, J. R.; Harris, J. W.; Diaz, R. E.; Ren, Y.; Ribeiro, F. H.; Miller, J. T., Pd–In intermetallic alloy nanoparticles: highly selective ethane dehydrogenation catalysts. *Catalysis Science & Technology* **2016,** *6* (18), 6965-6976. https://doi.org/10.1039/c6cy00491a
31. Armbruster, M.; Schlogl, R.; Grin, Y., Intermetallic compounds in heterogeneous catalysis-a quickly developing field. *Sci Technol Adv Mater* **2014,** *15* (3), 034803. https://doi.org/10.1088/1468-6996/15/3/034803
32. Kovnir, K.; Armbrüster, M.; Teschner, D.; Venkov, T. V.; Jentoft, F. C.; Knop-Gericke, A.; Grin, Y.; Schlögl, R., A new approach to well-defined, stable and site-isolated

catalysts. *Science and Technology of Advanced Materials* **2007,** *8* (5), 420-427. https://doi.org/10.1016/j.stam.2007.05.004

33. Pei, G. X.; Liu, X. Y.; Yang, X.; Zhang, L.; Wang, A.; Li, L.; Wang, H.; Wang, X.; Zhang, T., Performance of Cu-alloyed Pd single-atom catalyst for semihydrogenation of acetylene under simulated front-end conditions. *ACS Catalysis* **2017,** *7* (2), 1491-1500. https://doi.org/10.1021/acscatal.6b03293

34. Hsu, L.-S.; Wang, Y. K.; Tai, Y. L.; Lee, J. F., Photoabsorption study of the electronic structures of Ni_3Al, Ni_3Ga, Ni_3In, and $Ni_{13}In_9$. *Journal of Alloys and Compounds* **2006,** *413* (1-2), 11-16. https://doi.org/10.1016/j.jallcom.2005.06.065

35. Vogt, C.; Monai, M.; Kramer, G. J.; Weckhuysen, B. M., The renaissance of the Sabatier reaction and its applications on Earth and in space. *Nature Catalysis* **2019,** *2* (3), 188-197. https://doi.org/10.1038/s41929-019-0244-4

36. Yan, B.; Zhao, B.; Kattel, S.; Wu, Q.; Yao, S.; Su, D.; Chen, J. G., Tuning CO_2 hydrogenation selectivity via metal-oxide interfacial sites. *Journal of Catalysis* **2019,** *374*, 60-71. https://doi.org/10.1016/j.jcat.2019.04.036

37. Campuzano, J. C.; Greenler, R. G., The adsorption sites of CO on Ni (111) as determined by infrared reflection-absorption spectroscopy. *Surface Science* **1979,** *83* (1), 301-312. https://doi.org/10.1116/1.569974

38. Agnelli, M.; Swaan, H.; Marquez-Alvarez, C.; Martin, G.; Mirodatos, C., CO hydrogenation on a nickel catalyst: II. A mechanistic study by transient kinetics and infrared spectroscopy. *Journal of Catalysis* **1998,** *175* (1), 117-128. https://doi.org/10.1006/jcat.1998.1978

39. Martra, G.; Swaan, H. M.; Mirodatos, C.; Kermarec, M.; Louis, C., Sintering of Ni/SiO_2 catalysts prepared by impregnation and deposition-precipitation during CO hydrogenation. *Catalyst Deactivation, Proceedings of the 7th International Symposium* **1997,** *111*, 617-624. https://doi.org/10.1016/S0167-2991(97)80207-8

40. Gonzalez-Delacruz, V. M.; Pereñiguez, R.; Ternero, F.; Holgado, J. P.; Caballero, A., Modifying the size of nickel metallic particles by H_2/CO treatment in Ni/ZrO_2 methane dry reforming catalysts. *ACS Catalysis* **2011,** *1* (2), 82-88. https://doi.org/10.1021/cs100116m

41. Mihaylov, M.; Hadjiivanov, K.; Knözinger, H., Formation of $Ni(CO)_4$ during the interaction between CO and silica-supported nickel catalyst: an FTIR spectroscopic study. *Catalysis letters* **2001,** *76* (1), 59-63. https://doi.org/10.1023/A:1016786023456

42. Courtois, M.; Teichner, S. J., Infrared studies of CO, O_2, and CO_2 gases and their interaction products, chemically adsorbed on nickel oxide. *Journal of catalysis* **1962,** *1* (2), 121-135. https://doi.org/10.1016/0021-9517(62)90016-7

43. Németh, M.; Somodi, F.; Horváth, A., Interaction between CO and a coke-resistant $NiIn/SiO_2$ methane dry reforming catalyst: a DRIFTS and CO pulse study. *The Journal of Physical Chemistry C* **2019,** *123* (45), 27509-27518. https://doi.org/10.1021/acs.jpcc.9b06839

44. de Ménorval, L.-C.; Chaqroune, A.; Coq, B.; Figueras, F., Characterization of mono- and bi-metallic platinum catalysts using CO FTIR spectroscopy Size effects and topological segregation. *Journal of the Chemical Society, Faraday Transactions* **1997,** *93* (20), 3715-3720. https://doi.org/10.1039/A702174G

45. Furukawa, S.; Endo, M.; Komatsu, T., Bifunctional catalytic system effective for oxidative dehydrogenation of 1-butene and n-butane using Pd-based intermetallic compounds. *ACS Catalysis* **2014,** *4* (10), 3533-3542. https://doi.org/10.1021/cs500920p

46. Millet, M. M.; Algara-Siller, G.; Wrabetz, S.; Mazheika, A.; Girgsdies, F.; Teschner, D.; Seitz, F.; Tarasov, A.; Levchenko, S. V.; Schlogl, R.; Frei, E., Ni single atom catalysts for CO_2 activation. *J Am Chem Soc* **2019,** *141* (6), 2451-2461. https://doi.org/10.1021/jacs.8b11729

Chapter 6 - CONCLUSIONS AND FUTURE WORK

6.1 Conclusions

This thesis focused on strategies to optimize materials to be applied in processes of capture and use of CO_2. The following key conclusions are summarized. Firstly, the addition of sodium in the calcium oxide was evaluated during CO_2 capture in the steam methane reforming. For that, Na_2CO_3-CaO sorbent was synthesized by precipitation method and physically mixed with Ni/Al_2O_3. This material showed 100% of CH_4 conversion and 93.5% of H_2 molar fraction during all 10 cycles performed. However, the sorbent containing sodium presents a shorter pre-breakthrough duration than the pure CaO in the SE-SMR cycles. The characterizations revealed that, despite the increase in the surface area, the addition of sodium increased the particle size of the calcium oxide, leading to poor stability and low CO_2 capture. The sintering phenomenon could be justified by the presence of the promoter and synthesis conditions, such as the precipitation method and calcination temperature.

Secondly, the investigation of the performance of intermetallic compounds as a catalyst to convert CO_2 to CO by the rWGS reaction. Two compositions of Ni:In were synthesized by hydrothermal method and compared with Ni/SiO_2. The method produced nanoparticles with ~5nm of particle size and homogenous dispersion of the metals on the SiO_2 support. Regarding the phases produced by the bimetallic Ni-In catalysts, the *in situ* XRD data revealed that the $Ni_{0.85}In_{0.15}/SiO_2$ has two phases. The first is the alloy phase $Ni_{0.85}In_{0.15}$ and the second is the intermetallic Ni_3In phase which was formed during the cooling to reaction temperature. In addition, the $Ni_{0.50}In_{0.50}/SiO_2$ catalyst exhibited the intermetallic $Ni_{13}In_9$, which has a complex structure, as the major phase. The *in situ* XAS showed that the formation of these different phases caused a shift in the photon energy, which could be associated with the electron enrichment of the Ni atoms caused by the presence of the In atoms. In addition, different coordination environments and chemical bonds were observed in the intermetallic Ni-In/SiO_2 catalysts compared to the Ni/SiO_2.

The catalytic tests showed that the addition of indium promoted the selectivity toward CO in the rWGS reaction. The $Ni_{0.50}In_{0.50}/SiO_2$ catalyst showed 100% CO selectivity even in higher H_2:CO_2 feed compositions. However, the activity decreases

with the increase of the indium content. Therefore, a small addition of indium was enough to keep this high CO selectivity as evidenced by the $Ni_{0.85}In_{0.15}/SiO_2$ catalyst which showed selectivity values above 99%. To explain this high selectivity, CO-DRIFTS revealed that the indium addition provided a weak CO adsorption due to the geometric and electronic effects. The presence of indium atoms isolates the Ni atoms, avoiding the formation of the Ni ensembles which is necessary for a more stable configuration. Thereby, the CO species desorb instead of hydrogenating to form CH_4, leading to a high CO selectivity.

6.2 Recommendations for future work

Chapter 4:

- Synthesizing the CaO sorbent using different techniques such as template-assisted technique which can produce smaller the particle size, optimizing the CO_2 capture capacity and stability over the cyclic process;
- Investigation of the addition of other promoters in various concentrations including Li, K, Rb, Cs identifying its role during the CO_2 capture;
- Optimize the synthesis conditions like calcination temperature and use of different calcium precursors;
- Characterize the sorbents by HR-TEM to understand the CO_2 capture at the atomic level such as the carbonate product layer formation and structural modifications;
- Explore potential sorbents in sorption enhanced steam reforming methanol and ethanol.

Chapter 5:

- Investigate the effect of the binary temperature and duration in the annealing process to synthesize pure phase catalyst.
- Perform the EXAFS fitting to quantify the coordination number and Debye-Waller factor of the intermetallic Ni-In catalysts.
- Understand the surface of the Ni-In catalyst using XPS technique.
- Use DFT and quantum chemical calculations to investigate in deep the electronic effect that appears in the bimetallic catalyst and how it influences the mechanism reaction of the CO_2 conversion.

- Explore other intermetallic Ni-In phases as well as several binary systems such as Ni-Sn and Ni-Ga.